Design, fabrication and evaluation of graphene-gold nanohybrids for sensing, imaging and therapeutic applications

A THESIS PRESENTED BY

JIBIN K

TO

THE SREE CHITRA TIRUNAL INSTITUTE
FOR MEDICAL SCIENCES AND TECHNOLOGY, TRIVANDRUM
THIRUVANANTHAPURAM

IN PARTIAL FULFILMENT OF THE REQUIREMENTS

FOR THE AWARD OF

DOCTOR OF PHILOSOPHY

2020

CERTIFICATE

I, Jibin K, hereby certify that I had personally carried out the work depicted in the thesis entitled, **"Design, fabrication and evaluation of graphene-gold nanohybrids for sensing, imaging and therapeutic applications"**. No part of the thesis has been submitted for the award of any other degree or diploma prior to this date except where due acknowledgment has been made in the text.

Jibin K

Date: 25.11.2020 Reg.No: 2016/PhD/01

Dr. R. S. Jayasree
Division of Biophotonics and Imaging
Department of Biomaterial Sciences and Technology
BMT Wing, SCTIMST

This is to certify that **Mr. Jibin K**, from the Division of Biophotonics and Imaging of this Institute, has fulfilled the requirements prescribed for the Ph.D. degree of the Sree Chitra Tirunal Institute for Medical Sciences and Technology, Trivandrum. The thesis entitled, **"Design, fabrication and evaluation of graphene-gold nanohybrids for sensing, imaging and therapeutic applications"** was carried out under my direct supervision. No part of the thesis was submitted for the award of any degree or diploma prior to this date.

*Clearance was obtained from the Institutional Animal Ethics Committee (IAEC) for carrying out the study. (IAEC approval #SCT/IAEC-229/MARCH/2017/91).

Dr. R.S. Jayasree
Date: 25.11.2020 (Research Supervisor)

The thesis entitled

Design, fabrication and evaluation of graphene-gold nanohybrids for sensing, imaging and therapeutic applications

Submitted by

Jibin K

for the degree of

Doctor of Philosophy

of

SREE CHITRA TIRUNAL INSTITUTE

FOR MEDICAL SCIENCES AND TECHNOLOGY, TRIVANDRUM

THIRUVANANTHAPURAM

Is evaluated and approved by

....

Name of the guide Name of thesis examiner

Dedicated to my mother and my wife...

ACKNOWLEDGMENTS

I would like to express my sincere gratitude to my research guide, Dr. R. S. Jayasree, for her continuous support, valuable suggestions, and patience in mentoring during the entire course of my Ph.D. work. I am thankful to her for all the moral support and help that she has given me throughout my days in the laboratory. I owe my sincere gratitude to The Director, SCTIMST, and Head BMT Wing for providing the institute fellowship and infrastructural facilities. I extend my thanks to Dean, Associate Dean (Ph.D. affairs), Registrar, Deputy Registrar, and all members of the academic division and Director's office for their support and help. I acknowledge the former and present Head of the Division, for their academic support in carrying out my Ph.D. work. I am incredibly thankful to my doctoral advisory committee members, Dr. Roy Joseph, Dr. Manoj Komath, Dr.K.K.Maiti and Dr. Anilkumar.P.R, for their suggestions and critical comments in improving my Ph.D. work.

I acknowledge Dr. Manoj Komath, Mr. Nishad, Ms. Susan Mani of DBST for the TEM and SEM facility. I thank Dr. Roy Joseph and Mr. Willi Paul of DPMD for the Raman analysis. I sincerely thank Dr. M.R. Rekha for the academic support and critical comments that helped me to achieve the objectives of my study. I thank Dr. Maya Nandkumar, Mr. Pradeep, and all staff of DMIT for providing the spectrometer facility for my studies. I sincerely acknowledge Dr. Sachin J Shenoy, Mr. Manoj, and Mr. Sunil and Mrs. Joly of DLAS for helping me in animal experiments. I am thankful to Dr. Anughya Bhatt and all lab members of TRU for helpimg in the blood studies. I sincerely thank Er. Ramesh Babu and his entire team of DPF for the assistance during the fabrication of lab-on-a-filter system.

I cherish every moment that I shared with my former fellows Dr. Arya Saraswathy, Dr. Vineeth, Shamon, Mr. Jayaram, Ms. Dhanya and Ms. Nisha. I also thank all my present lab members Dr. Rekha,Ms.Parvathy, Ms. Resmi V Nair, Ms. Hema, Ms. Marina,Ms. Renuka, Ms. Resmi, and Ms. Rinta, for their support in carrying out my Ph.D. work in the division. I also thank all the staff of BMT Wing, who directly or indirectly helped me in completing my Ph.D. program; thanks to the

division of accounts, stores & purchase, library and the security staff for their kind support

I am indebted to my mother and wife for their prayers, patience, and support, which made my life easy and supported me in the successful completion of my Ph.D. work. Above all, I thank God Almighty for giving me the strength to stand up and walk again during all the difficult times in my life.

Table of Contents

List of Figures

List of tables

List of abbreviations

DNA	Deoxy ribonucleic acid
CTAB	Cetyltrimethylammonium bromide
2D	Two dimensional
GO	Graphene oxide
rGO	Reduced graphene oxide
Pa	Pascal
$AgNO_3$	Silver nitrate
CdSe	Cadmium selenide
Au	Gold
Cu	Copper
Ag	Silver
Rh	Rhodium
Ru	Ruthenium
MnO_2	Manganese oxide
CO_3O_4	Cobalt oxide
BSA	Bovine serum albumin
PEG	Poly ethylene glycol
SERS	Surface enhanced Raman scattering
MRI	Magnetic resonance imaging
S_1^1	Excited state singlet
S_1	Ground state singlet

LSPR	Localized surface plasmon resonance
EF	Enhancement factor
NMR	Nuclear magnetic resonance
EM	Electromagnetic
RF	Radio frequency
NMV	Net magnetization vector
T1	Longitudinal or spin-lattice
T2	Transverse or spin-spin
PDT	Photodynamic therapy
PTT	Photothermal therapy
CDT	Chemodynamic therapy
NIR	Near infra-red
ROS	Reactive oxygen species
PS	Photosensitizer
O_2	Molecular oxygen
HO•	Hydroxyl radical
O_2^{2-}	Peroxide
H_2O_2	Hydrogen peroxide
CT	Computed tomography
CTCs	Circulating tumor cells
FDA	Food and drug administration
Au NRs	Gold nanorods
FET	Field effect transistor
PDDA	Poly (diallyl dimethyl ammonium chloride)

PVP	Poly (vinylpyrrolidone)
CVD	Chemical vapor deposition
DOX	Doxorubicin
PEI	Poly ethyleneimine
$HAuCl_4$	Auric chloride
PpIX	Protoporphyrin IX
CS	Chitosan
TSC	Trisodium citrate
FA	Folic acid
TTNP	Targeted theranostic nanoprobe
EDC	1-Ethyl-3-(3-dimethylaminopropyl) carbodiimide
NHS	N-Hydroxysuccinimide
DPBF	1, 3-diphenylisobenzofuran
SDS	Sodium dodecyl sulfate
DCFDA	2′, 7′-Dichlorofluorescein diacetate
DLA	Dalton lymphoma ascites
PMNP	Plasmonic magnetic nanoprobe
4-ATP	4-amino thiophenol
SPIONS	Super paramagnetic iron oxide nanoparticles
GSH	Glutathione
MB	Methylene blue
$[Ru(dpp)_3]Cl_2$	Ruthenium tris(4,7-diphenyl-1,10-phenanthroline)dichloride

SYNOPSIS

Recent advances in material science and nanotechnology have boosted the emergence of diverse nano-regimes with abundant nanostructures and compositions with distinctive chemical as well as physical properties. In the last few decades, these nanosystems exhibited a tremendous progress in its design and fabrication to gear towards the vital advancement for the assistance of human health through biological and biomedical applications. Recently, two dimensional graphitic materials such as fullerenes, carbon nanotubes, graphene oxide (GO) and reduced graphene oxide (rGO) have attained a great attention and interest in this area. These carbon allotropes have good biocompatibility and are enriched with several functional groups over its two dimensional surface to tweak its exceptional physico-chemical properties as compared to other nanomaterials. Especially, GO and rGO have been comprehensively employed as a nanocargo by utilizing its poly aromatic structure and weak van der Waals interactions for the effective delivery of insoluble anticancer drugs, peptides, genes and nucleic acids into the cellular environment for bioimaging and therapeutic applications.

On par with, gold nanostructures (Au NS) have also gathered great attention owing to its anisotropy, exceptional absorption properties and catalytic abilities. In fact, the discovery of immunogold labeling in 1970's, brings out the idea of using metal nanoparticles as nanobioconjugates for biomedical application. Moreover, the nanoformulations are also playing a crucial role in bringing a significant contribution to the fundamental properties of Au NS such as its plasmon absorption and scattering for photodiagnosis and phototherapies of heterogeneous diseases like cancer. Various anisotropic Au NS also contributes significantly to the drug vectorization, assured to a bright future, to improve biodistribution and therapeutic efficiency, thereby overcoming the issues of stability, solubility and toxic side effects of pharmacokinetic drugs.

The integration of GO or rGO nanosheet with Au NS has developed into a new class of functional metamaterials with improved efficacies and thus offers new prospects in the usage of such nanohybrid architectures for biosensing and

biomedical applications. They can produce a dual-enhanced effect which presents itself as a biodegradable and biocompatible nanoplatform for the release of numerous payloads. Thus, the current research work provides insight into the important features of gold–graphene nanocomposites and also into its various nanoarchitectures for potential applications in biosensing, imaging and therapy.

The thesis has been organized into 5 chapters. Chapter 1 deals with the general introduction about various graphitic materials, graphene-metal nanohybrids, reported synthetic routes for the synthesis of graphene-metal hybrids, importance of graphene-gold nanohybrids, various imaging and therapeutic modalities for cancer, theranostic applications of graphene-gold hybrids and development of clinical screening tool for personalized treatment of cancer.

Chapter 2 summarizes the literature review of biosensing, bioimaging and therapeutic applications of graphene-gold nanohybrids.

Chapter 3 details the materials and methods used for the development of various multifunctional graphene-gold nanohybrids for the diagnostic and therapeutic applications in personalized cancer treatment. All the materials and experimental procedures used for the syntheses and characterization of various nanostructures used in this thesis are enlisted in this section.

Chapters 4 deals with the results and discussion. This chapter is mainly divided into 3 sections.

The first section describes the development of a targeted theranostic nanoprobe (TTNP) which is designed with site specific dual imaging guided triple therapy to form a new paradigm in targeted cancer theranostics. TTNP consists of a plasmonic gold-graphene hybrid (Au-rGO) and a polymeric assembly of chitosan, protoporphyrin IX (PpIX) and folic acid (CS-PpIX-FA) tagged through their electrostatic interaction. Owing to the presence of spiky gold structures present in the graphitic layers, TTNP exhibited high photothermal therapeutic (PTT) efficacies together with good surface enhanced Raman scattering (SERS) properties. Moreover, TTNP was also able to retain the characteristic Soret and Q bands of PpIX, ensuring

the activatable intracellular “off/on” fluorescence imaging assisted photodynamic therapy (PDT). The incorporation of folic acid (FA) facilitated tumor specific accumulation thereby producing maximum therapeutic efficacy with minimal side effects. Thus, TTNP opens the new avenue for the successful visualization of the cellular internalization through dual imaging of SERS and fluorescence without compromising one another. In addition, TTNP also showed high drug loading capacities of anticancer drug doxorubicin (DOX) and exhibited pH and heat stimulated drug release properties. The therapeutic action of TTNP was examined through various apoptotic assays like live dead assay, cytotoxicity assay and flow cytometric assay. The biodistribution profile of TTNP was successfully able to visualize *in vivo* and *ex vivo* through fluorescence imaging and SERS analysis which showed good retention in the tumor area for 24 hours. The tumor reduction experiments carried out with TTNP-DOX after irradiation using both 808 nm and 532 nm lasers induced the maximum tumor reduction among the various sets of experimental counterparts. Thus, TTNP was successfully able to perform the dual imaging (SERS and fluorescence) enabled triple therapy (PTT, PDT, chemo-PTT) in a single nanoplatform.

The second section discusses about the development of a plasmonic magnetic nanoprobe (PMNP) designed to perform dual imaging (SERS/magnetic resonance imaging (MRI)) tailored tumor micro environment (TME) responsive dual therapy (chemodynamic therapy (CDT)/PTT) as a multifunctional theranostic tool for cancer management. The PMNP was formulated by coupling the amine groups of Au-rGO-4-ATP with the carboxylic acid groups of citrate capped super paramagnetic iron oxide nanoparticles (SPIONS) through carbodiimide reaction. The absorption spectrum of PMNP was extended from the near infra-red (NIR) to ultra-violet (UV) region owing to the presence of graphitic layers, plasmonic nanoseeds and SPIONS in the nanoconstruct. The PTT efficacy of PMNP was entirely benefited from its NIR absorption which exhibited a temperature rise up to 43 ^{o}C within 5 minutes of irradiation with 808 nm laser (1.5 W/cm^2). Moreover, the nanosystem produced enhanced Raman signals of D and G bands of graphene as well as the 4-amino thiophenol (4-ATP) unit tagged over the gold nanoseed through both electromagnetic

as well as chemical enhancement mechanism of Au-rGO. PMNP also exhibited super paramagnetic behavior and T_2 MRI contrast similar to bare SPIONS. Furthermore, we have smartly utilized the specific features of TME such as low oxygen concentration, weakly acidic pH environment, high glutathione (GSH) and high hydrogen peroxide (H_2O_2) concentrations for killing the cancer cells with excellent specificity. The CDT efficacy of PMNP investigated under these conditions showed the effective generation of hydroxyl radicals (·OH) which got more pronounced upon induction with photothermal stimulus. Due to the overexpressed levels of GSH and H_2O_2 in cancer cells, which sequentially triggers the redox reactions, PMNP displayed superior cytotoxic effects on cancer cells, while keeping the normal cells unharmed. Furthermore, the probe proved to be an effective therapeutic agent *in vivo* which was revealed from the tumor reduction experiments carried out on tumor bearing mice.

In the third section, we developed a custom-designed portable centrifugal prototype based size selective lab-on-a-filter circulating tumor cell (CTC) detection system for the rapid isolation of CTCs with high purity. The centrifugal prototype comprises of three independent chambers for whole blood sample loading, CTC filtration, and waste residual blood storage. The lab-on-a-filter platform utilizes centrifugal force to rapidly transfer unprocessed whole blood samples from one of the centrifugal prototype chambers to another. To selectively isolate CTCs based on size differences between CTCs and the surrounding hematologic cells, we have integrated an anti-EpCAM antibody coated track-etched polycarbonate membrane filter on our system. In order to further improve the sensitivity of detection, a SERS nanotag built on Au-rGO@antiErbB2 was employed which played a key role in the isolation and quantification of CTCs among the millions and millions of healthy cells in the human blood stream. The time required to separate 5 mL of sample was about 60 s, which is a considerably less time compared to earlier reported procedures. The probe showed excellent sensitivity and selectivity for the specific detection and quantification of CTC from other interfering blood cells. Taken together, the as-proposed lab-on-filter system served as a potential candidate for the accurate

quantification of CTC, which may have huge impact in translational clinical research.

The chapter 5 deals with the summary, conclusions and future perspectives of the present study. The whole thesis is focused on the diverse application of graphene-gold nanohybrids for disease diagnosis, imaging and therapeutic applications. We have brought home the fact that these types of nanohybrids will, in course of time, achieve a breakthrough on the medical front. The *in vivo* studies that we have carried out here are versatile in content and are likely to have a tremendous appeal in the days to come. Future outlook is propelled to assess the suitability of these nanohybrids in clinical translation.

Chapter 1

Introduction

Chapter 1

Introduction

Last few decades have witnessed remarkable progress in the fabrication and utilization of nanomaterials tailored towards the biological and biomedical applications. Among various nanoparticles, gold nanostructures have gathered a special focus owing to its low toxicity, ease in mimicking into various shapes and ease to attach with biologically relevant molecules. Thus, they are regarded as one of the best candidates for various biological applications such as immunoanalysis, biosensing, genomics, detection and therapy of cancer cells, optical bioimaging, and targeted delivery of DNA, drugs, and antigens. In fact, it has been established as a good candidate for almost all critical medical applications ranging from diagnosis to treatment applications (Wilson *et al*., 2008).

In spite of all these exciting properties, gold nanostructures tend to show nonspecific binding and particle instability in biological systems. Especially, the surface capping ligands have a huge role in the particle aggregation. They will either undergo cross-linking or displacement from the particle surface which depends up on the ionic strength of the medium. In addition to that, the biocompatibility of these tagged ligands has also been a major concern over the years. For example, cetyltrimethylammonium bromide (CTAB) has been commonly used as a capping agent for imparting better stability and morphology of gold structures like nanorods. But it causes high cytotoxicity to cells owing to its surfactant nature (Goodman *et al*., 2004). It is very difficult to remove once it gets internalized and even cause disruption of the cell membranes. In addition, CTAB stabilized gold nanorods lack targeting efficacies, which is an essential criterion for treatment of pathogens or cancer cells etc. Thus, development of gold nanostructures with suitable coating and stabilizing agents is critical for moving forward its application, especially in biomedical field.

Among the current efforts to solve this problem, carbon based nanomaterials or carbon shells presented themselves as an attractive alternative for embedding or encapsulating various gold nanostructures owing to its excellent intrinsic properties (Kim *et al*., 2002), (Chopra *et al*., 2009). Moreover, graphene, the recently discovered carbon allotrope and its derivatives are regarded as the best suited templates for the growth and stability of various nanoparticles including gold nanoparticles as compared to other carbon allotropes like carbon nanotubes, fullerenes, carbon dots etc. This thesis deals with the preparation, characterization and design of gold-graphene hybrid systems for various biomedical applications ranging from sensing to therapy. This section discuss about the various graphitic materials, graphene-nanoparticle hybrids, importance of graphene-gold hybrid materials and their applications in biological and biomedical field.

1.1. Graphene

Naturally occurring carbon allotropes are formed by difference in covalent bonding between various carbon atoms. Each one of these allotropes has distinct chemical and physical properties due to characteristic spatial arrangement adopted by its carbon atoms. Among various allotropes, graphene represents an important member which is a two dimensional (2D) material consisting of sp^2 hybridized carbon atoms forming one-atom thick sheets arranged in a perfectly honeycomb structure (Geim *et al*., 2007). Owing to its unique physicochemical and structural characteristics, graphene exhibits various exceptional properties. Its general characteristic properties includes high surface area (2630 m^2 g^{-1}) (Stoller *et al.*, 2008), good mechanical strength (Young's modulus of 1100 GPa) (Lee *et al*., 2008), superior thermal conductivity (5000 $Wm^{-1}K^{-1}$) (Balandin *et al.,* 2008), exceptional optical properties (fluorescence quenching properties and high opacity) (Gomez-Navarro *et al*., 2007) and alluring electronic properties (high carrier capacity and mobility [10, 000 cm^2 V^{-1} s^{-1}] (Bolotin *et al*., 2008). These properties enable graphene and graphene related nanoconstructs to gain worldwide interest, and undoubtedly, hold the most promising potential for implementation in diverse applications.

Graphene is entirely composed of sp^2 hybridized carbon atoms whose electrons are engaged in domains of aromatic conjugation. In graphite, these graphene sheets are being hold tightly by its van der Waals forces. The aromatic domains of various single layered graphene sheets make graphite 'a conducting material' among various natural allotropes of carbon. The existence of single layer of graphene has been theoretically discussed more than fifty years ago. Yet, the probability of single-atom thick, two-dimensional nanocrystal was believed to be impossible. But, in 2004, Geim and Novoselov were successfully able to isolate and characterize single layers of graphene (Novoselov *et al*., 2004). Thereafter, an exponential rise was observed in the research of graphene materials in different scientific fields.

Affirmed of all these properties, the apolar nature of graphene, even in the case of single layer makes its more hydrophobic. In addition to that, its large scale synthesis is being hindered by chemical inertness and difficulty in obtaining it in defect-free state, which is critical for the real life applications.

1.2. Graphene derivatized materials

1.2.1. Graphene oxide

Interest in single layered mono-atomic graphene sheets also draws attention to other graphene derived materials that are now thoroughly investigated in depth under a different light. The most noticeable among them is graphene oxide- which is the derivatized form of graphene sheets with oxygen rich functional groups. By analogy

Figure 1. Synthetic strategy towards the preparation of graphene oxide from graphite. Adopted from (Gupta *et al*., 2017)

to graphene and graphite, graphene oxide is regarded as the 'primitive building block' of single graphite oxide layer. It was first discovered more than one fifty years ago, more particularly through the oxidation of graphite in acidic condition. Nowadays, the most commonly used method for the synthesis of graphene oxide is based on the methodology known as Hummers method (introduced by Offeman and Hummers) (Figure 1). In this method, graphene oxide is synthesized through the oxidation of graphite using potassium permanganate and sulphuric acid (Dreyer *et al*., 2010). During the oxidation of graphite to graphite oxide, the tightly packed graphite layers loosens its integrity due to the introduction of various functional groups like hydroxyl, epoxides and carbonyl groups on the edges and planar surfaces of carbon sheets. The graphene oxide monolayer sheets can be further obtained from graphite oxide through ultra-sonication. Owing to the presence of oxygen-rich functionalities, graphene oxide offers hydrogen bonds with water molecules and exhibits more hydrophilicity (Pan *et al*., 2012). This enables graphene oxide to form stable suspensions in aqueous solutions under various pH conditions. The properties of aqueous dispersibility and stability of single or few layered graphene oxide has great advantage over other carbon based materials and earning a significant role and popularity in scientific fields, especially in biomedical field (Sanchez *et al*., 2012). Further from the hydrophilic property of graphene oxide, its physico-chemical properties can be tuned to different chemically versatile domains and adjusted to a robust candidate for various applications. Unfortunately, graphene oxide is reported to have limited thermal and electrical transport due to its oxygen functionalities over its basal planes, which overlooked its certain applications.

1.2.2. Reduced graphene oxide

Since inexpensive and effective methods looking for accommodating all the properties of graphene are being aggressively sought for, the reduction of graphene oxide(GO) to reduced graphene oxide (rGO) (Figure 2) became more attractive. Actually rGO is a form of graphene which has similar conducting properties to that of graphene and several cost effective and simple methods are available for its synthesis. It contains residual oxygen functionalities and heteroatoms, in addition to distinct defects, unlike in the case of graphene (Varela-Rizo *et al*., 2012). Moreover,

it contains more structural defects and lesser quality of graphene produced from graphite. Reduced graphene oxide forms the natural choice for graphene applications like conductive inks, sensors and composite materials and more, since it can be synthesized in large quantities with low cost.

Once rGO has been synthesized, there are several ways to functionalize and tune it with various materials to form new compounds for specific applications. Chemical treatment or coupling with different two dimensional materials can be employed to enhance the properties of as-developed material to suit its commercial applications.

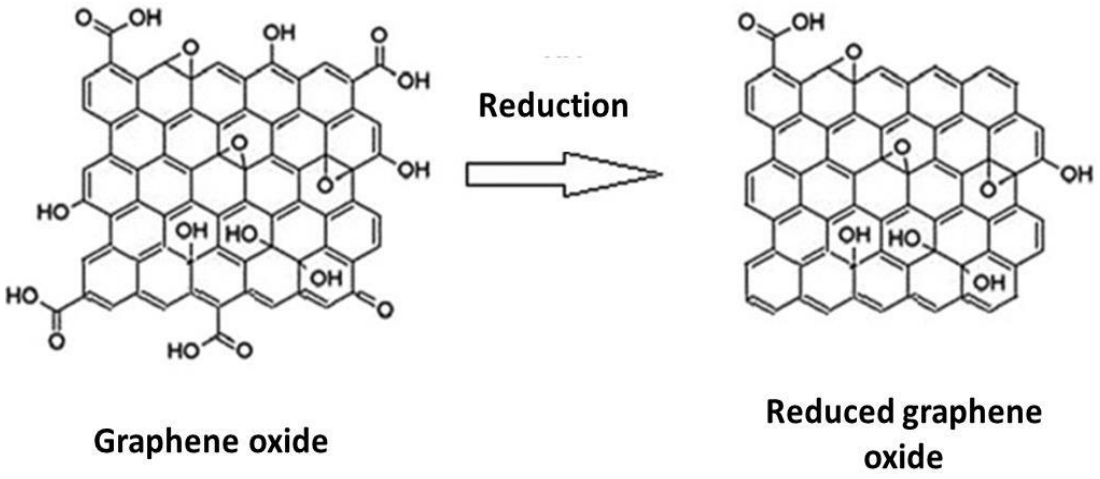

Figure 2. Synthetic strategy of conversion of graphene oxide to reduced graphene oxide. Adopted from (Szunerits *et al*., 2014).

1.3. Graphene-nanoparticle hybrid systems

Among various hybrids and composites of graphene and its derivatives (graphene oxide and reduced graphene oxide), majority of reports are focused on the development of hybrid systems coupling graphitic materials with nanoparticles. The combination of graphitic materials and various nanoparticles to form graphene-nanoparticle hybrid systems provide with a number of unique and specific physico-chemical characteristics and functions which are highly desirable and essential for various applications. These hybrid systems have pronounced performance and synergistic properties than the individual properties of either of the material alone,

which certainly augment their efficiency to outperform all the currently available nanomaterials in different fields. The integration of graphene with different nanosystems like metallic nanoparticles, mesoporous silica nanoparticles and quantum dots opens fascinating opportunities in electronics and nanomedicine. However, the roles of graphene in these two applications are entirely different. For electronic applications, the optical transparency and electronic mobility of graphene are utilized whereas in biomedical applications ranging from drug delivery, bioimaging, biosensing and theranostic applications, the layered wrapping sheets of graphene with high absorption properties, heat generation ability and large surface area were utilized for further functionalization (Nguyen *et al*., 2014).

1.3.1. Synthetic approaches of graphene-nanoparticle hybrids

Graphene-nanoparticle hybrid systems can be prepared by various synthesis approaches. Based on the final structural morphologies of hybrid platform, the synthetic approaches can be divided into two main categories. (a) nanoparticles decorated over graphene or graphene derivatives, and (b) nanoparticles covered or wrapped by graphene or graphene derivatives (Figure 3). The focal difference between these two methods is the relative size ratio between the planar dimensions of graphene and nanoparticles. When the size of the nanoparticles comes under 100 nm, it will be small enough to decorate over the graphene sheets. Whereas, when the nanoparticles have large size as compared to the graphene, its planar sheets can be used for covering nanoparticles, forming the second category of hybrid systems.

1.3.1.1. In situ decoration of nanoparticles on graphitic layers

In situ formation of nanoparticles over the surface of graphene can be accomplished with the help of techniques like sputtering, pulse laser deposition or thermal evaporation (Zhou *et al*., 2010) (Bajpai *et al*., 2011). These techniques are capable of preserving the high electron mobility and defect free nature of graphene during the process. Thus, hybrids made through these techniques exhibit good performance in counter electrodes and nanocapacitors. But, the requirement of high temperature (~1260 ºC) and high pressure (10^{-4} Pa) along with high cost and low efficiency have backfired these techniques when used in large scale synthesis. However, graphene

oxide or reduced graphene oxide, which gets readily dissolved in some solvents, have been utilized for synthesizing several hybrid systems using versatile techniques.

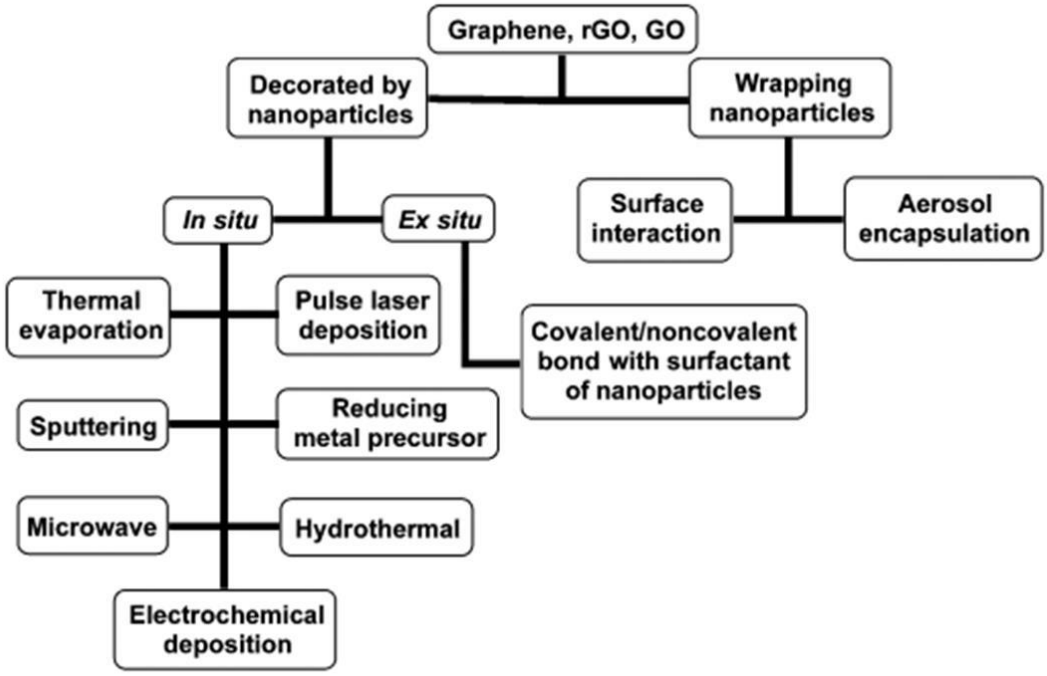

Figure 3. Flow chart representing various synthetic approaches towards the development of graphene-metal nanohybrids. Adopted from (Nguyen *et al*., 2014).

Simultaneous reduction of various metal salts and nucleation over the graphitic planes are widely utilized for the synthesis of GO or rGO-metal nanoparticle hybrids (Goncalves *et al*., 2009). The metal salts like $HAuCl_4$, K_2PtCl_4 and $AgNO_3$ are the commonly used metal precursors and reducing agents like trisodium citrate, ascorbic acid, ethylene glycol and sodium borohydride are utilized for its reduction into various nanoparticles over graphene surface (Liu *et al*., 2012) (Muszynski *et al*., 2008) (Fu *et al*., 2010). The reaction process is similar to the normal nanoparticle synthesis which includes reduction process, nucleation and growth of the particle. The various carbonyl groups on the surface of GO or rGO, such as alcohols (-OH), acids (-COOH) and epoxides (-COC) are responsible for the attachment of metal precursors on the graphitic surface through electrostatic interactions. In addition, the presence of different reducing agents promote the formation of respective nanoparticle over the basal planes of GO and rGO. More

importantly, the particle density over the graphene surface can be perfectly tuned by controlling the density of oxygen containing functional groups. Further, the hybrids of semiconductor nanoparticles like CdSe with GO/rGO can be easily achieved by adding rGO during the synthesis of CdSe nanoparticles. This process will greatly enhance the light induced charge transfer from the semiconductor nanoparticles to rGO owing to the direct anchoring of CdSe nanoparticles over the surface of rGO (Lin *et al*., 2010).

The microwave method can be utilized as an alternative technique as its energy can be used as a source of reduction process. Metals (Au, Cu, Ag, Rh and Ru) as well as metal oxide (MnO_2 and CO_3O_4) nanoparticles can be rapidly developed over graphitic materials through microwave irradiation (Marquardt *et al*., 2011). However, as compared to the conventional methods, microwave technique has limited control over the particle size and distribution over the surface of GO and rGO. For *in situ* decoration, hydrothermal technique is also regarded as a promising approach to prepare nanoparticles with high crystalinity over the single layer of graphene. This technique involves the use of high temperature and pressure, which results in the formation of nanocrystals with the simultaneous reduction of GO to rGO. The reduction of GO through this process is similar to the conventional methods. The I_D/I_G ratio of rGO obtained through hydrothermal methods (2.30:1) is similar to that of pristine graphene (2.45:1), thereby indicating that sp^2 domain in the carbon network of graphene gets recovered during the reduction of process. Further, the direct deposition of nanoparticles over graphene layer can be accomplished through electrochemical deposition method. The advantage of this method is that it doesn't require any kind of post-synthetic preparations like annealing or transferring. Since these hybrids can be easily coated on the electrodes, they are most commonly utilized as biosensors (Artiles *et al*., 2011). Currently, this technique is regarded as a highly versatile approach to alter the working electrodes so that, they can be perfectly tuned to be employed as sensitive, selective, scalable and reproducible biosensors.

1.3.1.2. Ex situ decoration of nanoparticles on graphitic layers

The hybrids formed by the combination of pre-synthesized nanoparticles and graphitic materials provide an alternative method for good control over the particle shape, size and functionality. Various nanoparticles with distinct morphologies like spherical, rod-like, cage shape, nanowire, hollow etc. have been studied in detail in the last decade to get hybrid materials with homogeneous physico-chemical properties (Burda *et al*., 2005). Thus, the *ex situ* synthesis method indeed provides an outstanding platform for the development of nanoparticles over the planes of graphitic layer. The driving forces behind the decoration of nanoparticles over the 2D material is basically due to the non-covalent interactions and π-π stacking between the nanoparticles and graphene layers. These weak forces of attractions were established by adhering the nanoparticles on to the graphene by exchanging or modifying the surfactant present on the surface of nanoparticles. Usually, surfaces of GO and rGO are manipulated with various "linker molecules" like amines, acids and thiols or "adhesive polymers" like bovine serum albumin (BSA) and poly ethylene glycol (PEG), owing to their good biocompatibility and hydrophilic nature.

1.3.1.3. Nanoparticles wrapped by graphitic materials

The approach of *ex situ* immobilization of nanoparticles with graphitic materials has been applied to nanomaterials with large particle size ranging from hundred nanometers to few micrometers, to obtain the graphene-wrapped nanoparticles (Zheng *et al*., 2014). Metals and metal oxides wrapped by GO or rGO were commonly employed as the electrode of lithium ion storages. The use of GO and rGO will provide stability and space for large volume changes during the cycle processes, which assists to master the disadvantages of metal/metal oxide as anode materials. This low cost and facile method will provide the insight pathway for the large scale synthesis of nanoparticles wrapped graphene materials, especially for energy storage applications. Aerosol encapsulation technique is also an alternative approach for the synthesis of wrapping hybrids. This technique relies on the colloidal interaction between the drying microdroplets. But as compared to the other methods, this technique produces particles of smaller size. In contrast to other techniques, this

method allows the encapsulation of particles having similar charge to that of graphitic materials. This technique is very simple and facilitates great advantage over other conventional techniques, especially in biomedical applications.

The interface between biology and nanotechnology is regarded as one of the promising and modish arteries in nanoscience. In the case of graphene-nanoparticle hybrids, the exceptional biocompatibility imparted by graphitic materials present in the hybrids, makes it an ideal candidate for biomedical applications such as tissue engineering, light mediated therapeutics, drug delivery etc. Various nanoparticles including iron oxide, noble metals (Au, Ag, Cu), organic, up-conversion and silica nanoparticles have been utilized for the rational combination with graphitic materials to produce synergistic effects to generate pronounced effects in biological applications (Chen *et al*., 2013).

1.4. Role of graphene-gold hybrids in biomedical applications

The driving force behind the tremendous development of graphene-gold hybrids in biomedicine among various graphene nanomaterials can be attributed to its exceptional stability, versatile physicochemical properties and superior biocompatibility. Coupling of gold nanoparticles with graphitic materials or

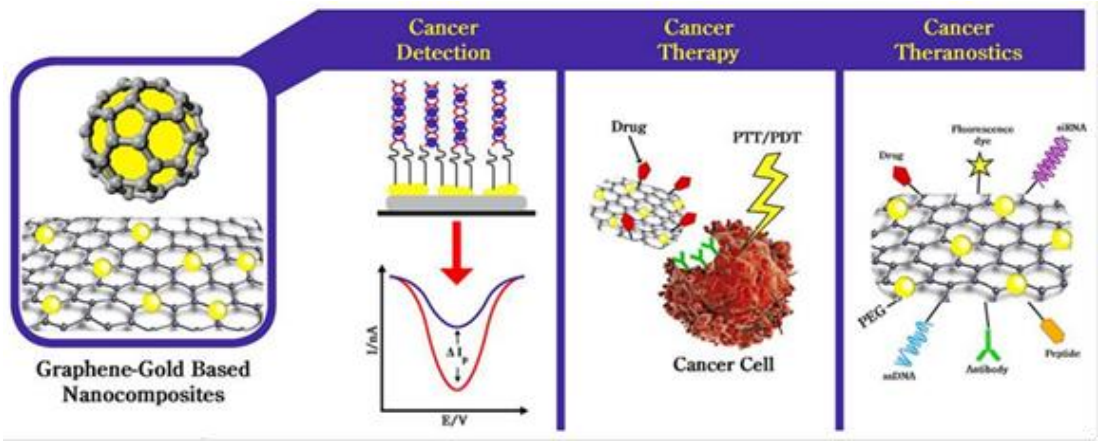

Figure 4. Various biomedical applications of graphene-gold nanohybrids. Adopted from (Al-Ani *et al.*, 2017).

wrapping of gold nanoparticles inside graphitic layers are the two main strategies used for the synthesis of graphene-gold hybrids (detailed description is given in section 1.3). Both GO and rGO can be easily adapted to these two strategies due to its various oxygen rich functionalities through covalent linkages, electrostatic interactions and π-π stacking. Even though, single layered GO can be isolated, owing to the strong van der Waals interactions between the graphene layers, it will always try to aggregate to form graphite structure. But growing of gold structures over the graphene layers will prevent this action and act as a spacer between the graphitic layers, thereby creating both the sides of GO available for further functionalization. This indeed makes the real definition of a two dimensional material having maximum active heads in both the faces of graphene layers. This exceptional property makes graphene-gold nanohybrids the gold standard in various biomedical applications (Figure 4) and in the following sections we will be discussing its applicability in various fields like biosensing, imaging, therapy etc.

1.5. Biosensing and bioimaging

Understanding the molecular connections in living system in their innate habitat is a huge challenge, especially in the area of clinical diagnostics. In the preceding era, the traditional test tube biochemical experiments were employed for the quantitative estimation of molecular processes in cells where the biomolecules are either used in their purified or isolated form. Even though it is highly useful, the cellular environmental conditions are entirely different from the *in vitro* solution phase reactions. Actually, we need to consider and visualize the cell itself as a test tube in order to deeply understand the behavior and chemistry of living cells. This indeed, will provide insight into the diagnosis of various diseases. The main strategy for the successful detection, localization, and monitoring of molecular events in cells, tissues, and living organisms involves the use of various imaging agents along with very sensitive instrumentation.

The imaging agent makes molecular events visible, computable and observable over time, directing to review the molecular irregularities. Recently, nanoparticles have been successfully employed as a template for its inherent non-

invasive and real-time imaging capabilities like fluorescence, surface enhanced Raman scattering (SERS), magnetic resonance imaging (MRI) etc. (Tsien *et al*., 2003). These imaging techniques have pronounced effect for the visualization of biomolecules under courtesy in their innate environments with great spatial and sequential resolution for its imaging and sensing applications.

1.5.1. Fluorescence imaging

Fluorescence is the dissipation of energy in the form of light from electronically excited states generated by the excitation of a molecule or material by providing suitable energy. The fluorescence process is directed by three important events, all of which occur on timescales that are separated by several orders of magnitude (Figure 5a).

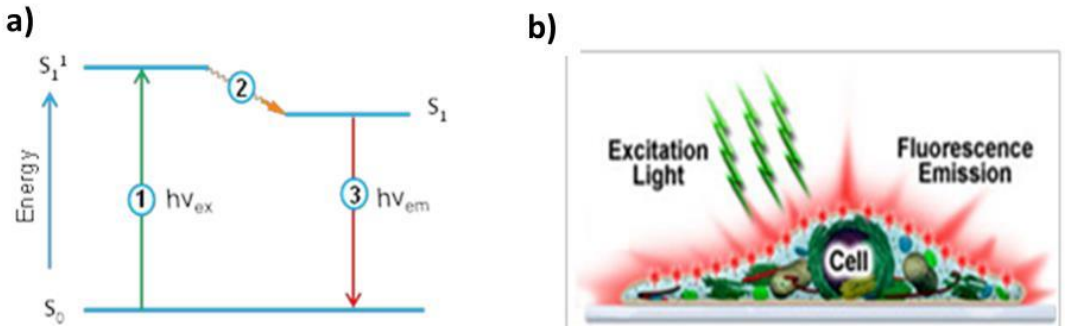

Figure 5. a) Jablonski diagram illustrating the various processes involved in the fluorescence. b) Schematic illustration of fluorescence imaging of a live cell. Adopted from (http://zeiss-campus.magnet.fsu.edu/articles/basics/fluorescence.html).

First, a photon of energy ($h\nu_{ex}$) is supplied to the susceptible molecule, which results in the absorption of light, creating an excited electronic singlet state (S_1^1). This process occurs in femtosecond (10^{-15} seconds), and then the molecule partially dissipates the energy via vibrational relaxation of excited state electrons to the lowest energy level (S_1), which can be measured in picoseconds (10^{-12} seconds). The final process is the emission of a longer wavelength photon ($h\nu_{em}$) and return of the molecule to the ground state, which occurs in the relatively long time period of nanoseconds (10^{-9} seconds). Although the entire molecular fluorescence lifetime, from excitation to emission, is measured only in billionths of a second, the

phenomenon is a remarkable indicator of the interaction between light and matter that forms the basis for the fluorescence microscopy. Because of the extremely sensitive emission profiles, spatial resolution, and high specificity of fluorescence investigations, the technique has become an important tool in cell biology (cartoon in Figure 5b) (Ishikawa-Ankerhold *et al*., 2012).

1.5.2. SERS imaging

Raman spectroscopy provides a "chemical finger print" of the analyte molecules as it count on gain or loss in energy of an inelastically disseminated photon during a molecular vibrational process. Conventional impulsive Raman scattering is inefficient as compared to the intrinsic elastic Rayleigh scattering, as it relies on the Raman cross-section or the polarisbility of the analyte (Aroca *et al*., 2006). Even while investigating aromatic molecules, whose π-bonds can be effortlessly delocalized around the ring, creating diverse vibrational modes, the possibility of a photon to be scattered inelastically is only ~1 in 10^8.

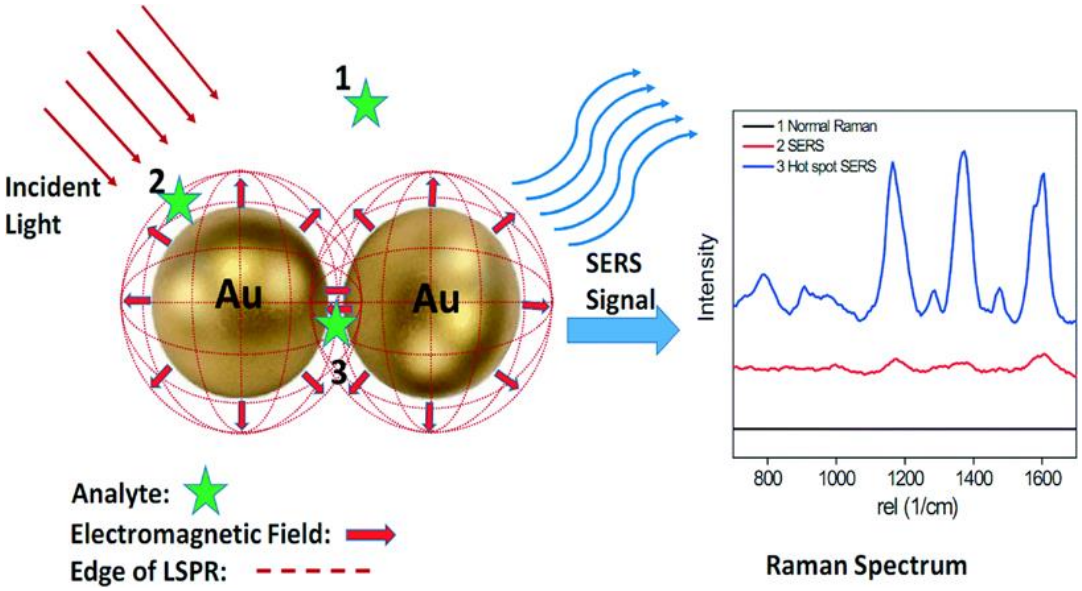

Figure 6. Schematic illustration of SERS hotspot generation of plasmonic nanoparticles in presence of analyte molecules and its corresponding Raman spectra. Adopted from (Haoran *et al*., 2015)

Surface-enhanced Raman spectroscopy (SERS) is a non-invasive analytical technique providing selective, sensitive and non-destructive imprints of bio/chemical

reactions, which is extremely required in numerous fields such as food safety, medical diagnostics, security and environmental protection etc. (Laing *et al*., 2016). SERS actually enrich the Raman signal of analyte molecule by several orders of magnitude by intensifying the electron density around roughened metallic nanostructures (Au, Ag, and Cu). SERS signal enrichment is accomplished through two different mechanisms, mainly electromagnetic enhancement and chemical enhancement (Stiles *et al*., 2008). For the simultaneous occurring of these two mechanisms, an analyte molecule should be adsorbed or be located in very proximity to the dielectric roughened surface (more often metallic structures).

Electromagnetic enhancement exploits the localized surface plasmon resonance (LSPR) of the metallic nanostructures to resonate with the wavelength of Raman excitation lasers. When this occurs, plasmons enhances the local electron cloud density, thus enlightening the probability of inelastic scattering process to occur when the analyte molecule is close to the surface of the particle thereby accounting for the hotspots (Figure 6) (Ding *et al*., 2017). For chemical enhancement to happen, analyte molecules need to be bound straight to the metal surface so that there is a charge-transfer to occur. Classic SERS enhancement factors (EF) are obtained in between 10^6 to 10^8 with some reports as high as 10^{14}, thereby facilitating single molecule detection (Champion *et al*., 1998). This intense SERS enhancement makes it extremely helpful for the detection of analyte having exceptionally low concentrations.

1.5.3. Magnetic resonance imaging

Magnetic resonance imaging is one of the major non-invasive and versatile imaging techniques employed for the investigation of internal physiology and anatomy of living subjects. The basic working principle behind the MRI is nuclear magnetic resonance (NMR), in which atomic nuclei close to strong magnetic field will absorb and emit electromagnetic (EM) waves at a specific resonant frequency, which falls in the region of radio frequency (RF) range. Since there are no adverse effects for radio waves or magnetic field, it can be regarded as one of the safest bioimaging technique (Busquets *et al*., 2015). Usually, magnetic field strength of 1.5-3 T is used for the

conventional imaging, providing wealth of information about the anatomy as well as structural properties of various samples.

Basically, MRI involves the interaction between the atomic nuclei having non-zero magnetic moment and external magnetic field. Since water is abundant in human body, proton nuclei were used for the bioimaging. When the external magnetic field applies, the protons of water, proteins or lipids present in the body will either align with or against the applied field and give a weak net magnetic charge described as net magnetization vector (NMV). When RF pulse is applied, the spin will start to flip between the low and high energy states (Lam *et al*., 2013). When the RF pulse is removed, the spin stops it's flipping and comes back to its normal state and this process is called relaxation. Actually, how quickly relaxation process happens during MRI measurements helps to distinguish between the various tissues in the human body. Generally two types of relaxation processes occur, T1 (longitudinal or spin-lattice) relaxation and T2 (transverse or spin-spin) relaxation.

Longitudinal or T1 relaxation measures how fast the NMV parallel to the applied external magnetic field relax to the normal ground state. It is important to note that, intense MRI signal will be produced by the protons that relax faster to the ground state (short T1) while low signal intensity will be produced by the those which relax slowly to the ground state (long T1). T1 relaxation is also known as spin-lattice relaxation since it involves the energy transfer between the spin states and ground lattice sites of the protons. Transverse or T2 relaxation measures how fast the NMV perpendicular to the applied external magnetic field will relax to the ground state. When the RF pulse is removed, nuclei with different magnetic field will interact and exchange energy between them. Therefore, T2 relaxation is also called spin-spin relaxation (Stephen *et al*., 2011). For MRI bioimaging, T1or T2 contrast images of different tissues can be obtained from the difference in the proton density in the respective tissue regions. This inherent MRI contrast obtained from the body can be further enhanced by using various contrast agents like gadolinium complexes and iron oxide nanoparticles. These contrast agents influence the relaxation processes and provide more contrast to the tissue samples, which is very useful for the proper diagnosis of heterogeneous diseases like cancer.

1.6. Therapeutic approaches in cancer treatment

Cancer constitutes the second leading cause of death in the world and studies suggest that 1 in 6 deaths are due to this deadly disease. Chemotherapy, radiation therapy, photodynamic therapy (PDT), photothermal therapy (PTT) and chemodynamic therapy (CDT) are among the commonly used modalities for treating cancer. The harmful side effects coming from chemotherapy due to the non-specific action of the drug molecules can be minimized by localized photo/chemo therapeutic treatments.

1.6.1. Photothermal therapy

Photothermal therapy serves as an effective strategy for treating solid tumors in a minimally invasive manner. PTT relies on the conversion of absorbed NIR light to localized heat (Figure 7a) (Cheng *et al*., 2012). The commonly employed PTT substrates include anisotropic gold nanostructures, carbon nanotubes etc. (Figure 7b) (Choi *et al.*, 2011). Combination of PDT (See Section 1.6.2) and PTT when administered in a single platform can produce remarkable treatment efficacy. So, it is demanding to develop an effective nanotheranostic agent that could integrate these phototherapeutic modalities for facilitating effective treatment in a non-invasive platform.

1.6.2. Photodynamic therapy

PDT has become one of the frontline options for cancer treatment because of its non-invasive nature, low systemic toxicity and reduced side effects (Dolmans *et al*., 2003). Although the clinical application of PDT has greatly enhanced over the past few years, it has been in practice over 30 years in treating bacterial and fungal infections. The basic principle of PDT relies on the generation of highly cytotoxic reactive oxygen species (ROS) upon excitation of a photosensitizing agent with light of suitable wavelength (Awuah *et al*., 2012). There are four main stages involved in the therapeutic process (Figure 8a). The first stage constitutes the administration of the sensitizer molecule into the body. In the second stage, the photosensitizer (PS) gets accumulated selectively at the target site. The third stage involves irradiation

with light of suitable wavelength in order to produce cytotoxic ROS via the excitation of PS. In the final stage, the as-formed ROS react with various biological

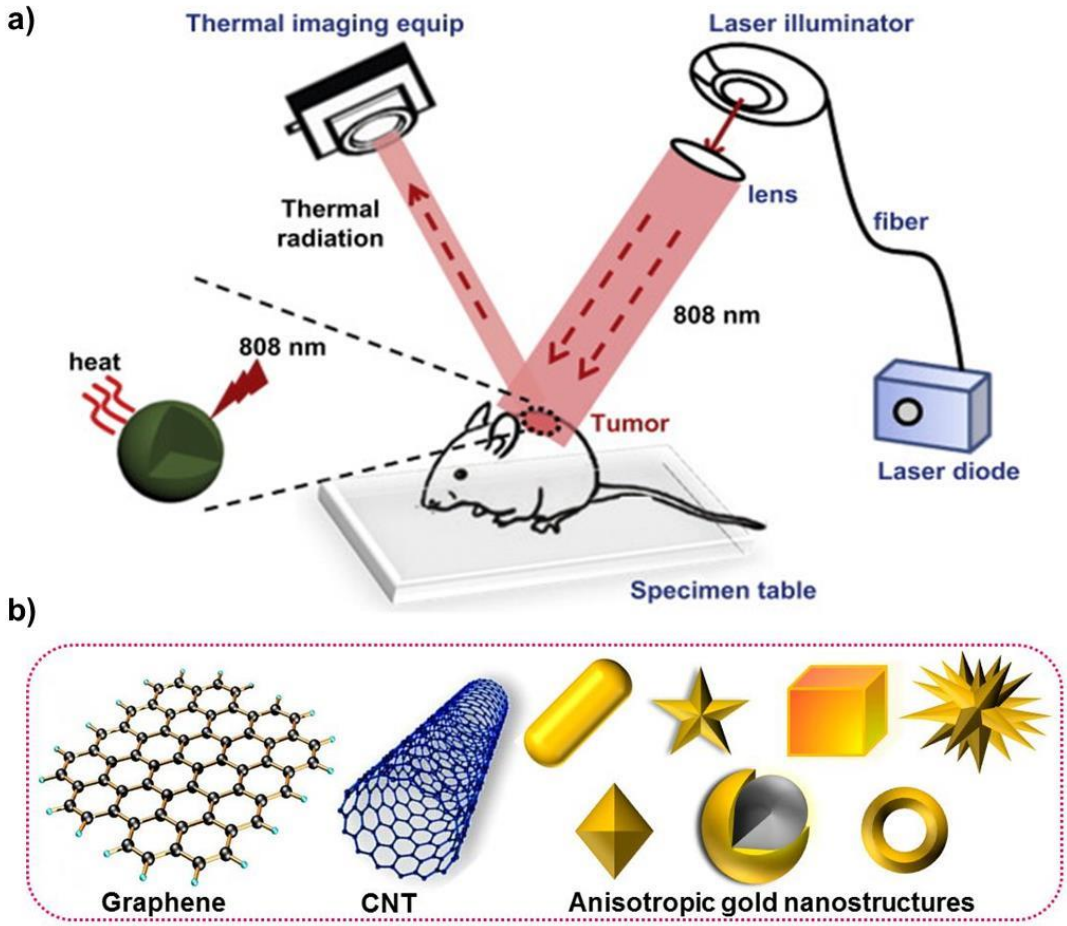

Figure 7. a) Instrumental setup for photothermal therapy and b) commonly used photothermal agents. Adopted from (Cheng *et al*., 2012) and (Choi *et al*., 2011).

targets like amino acids, lipids, proteins, nucleic acids etc thereby inhibiting the normal cell functioning and ultimately leading to cell death. Thus the photodynamic agent serves as a stimulus responsive system which is dormant in the dark condition and gets activated only upon irradiation with light of suitable wavelength. Some of the commonly used photosensitizers for PDT applications are shown in Figure 8b. PDT operates via two mechanisms viz, type I and type II mechanisms. In the type I mechanism, production of reactive species occurs through either hydrogen or electron transfer process between the excited state photosensitizer and the biomolecule. The latter mechanism, on the other hand, works by the conversion of

surrounding molecular oxygen ($^3O_2$) to cytotoxic singlet oxygen via direct energy transfer from the photosensitizer molecule. As a result of the wider operation of the type II PDT process, most of the PDT agents are highly oxygen dependent which involves a significant consumption of molecular oxygen. However, solid tumors are characterized by locations where the supply of O_2 is very low which may be attributed to the insufficient blood supply and massive proliferation of cancer cells

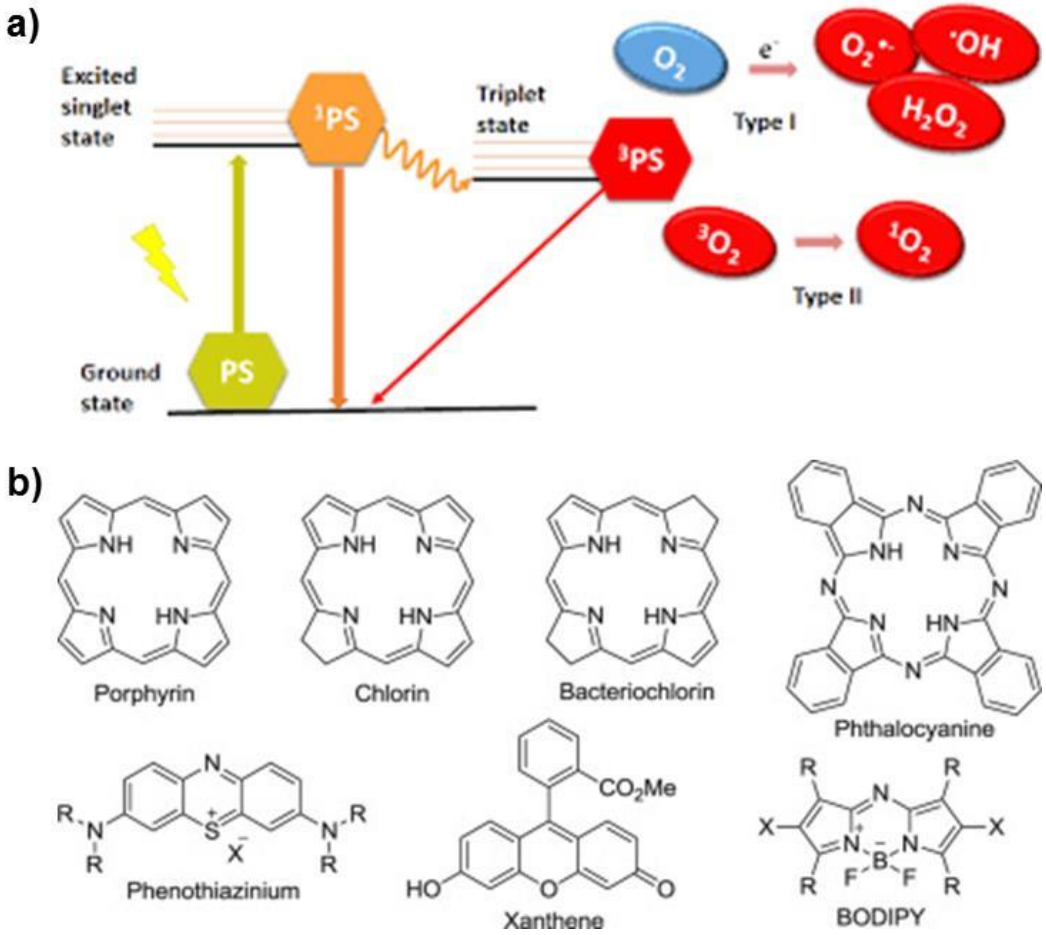

Figure 8. a) Schematic representation of various processes of photodynamic therapy and b) various commonly employed photodynamic agents. Adopted from (Liu *et al.*, 2015 and Zhang *et al*., 2018).

(Moulder *et al*., 1987). This oxygen deficiency in tumors restricts the real therapeutic potential of PDT, especially in cases which demand continuous treatment. In recent years, significant efforts have been put forward in overcoming the limits caused by hypoxia. These strategies have paved way to alleviate hypoxia by either direct

delivery of molecular oxygen or in situ production of oxygen in the tumor microenvironment (Chen *et al*., 2018). Oxygenation at the tumor site greatly increases the local oxygen concentrations in hypoxic areas which can subsequently enhance the efficacy of photodynamic cancer treatment. Although there occurred a series of developments in mitigating hypoxia to improve PDT efficacy, the attainment of a promising candidate has not yet been fulfilled due to the irregularity and lack of microvessels in tumor tissues, thereby leading to uneven distribution of photosensitizer (PS) molecules and non-homogeneous supply of oxygen. Moreover, other serious concerns with these approaches include oxygen leakage during the delivery process, low permeability of nanoparticles, poor biocompatibility and biodegradability of the oxygen carriers, inefficient oxygen production capacity etc. (Li *et al.*, 2016). The oxygen level in the tumor environment is influenced by the balance between oxygen supply and its consumption that both these factors should be carefully looked at while designing probes for treating hypoxic tumors. Thus there is an urgent need to develop simple and smart nanoformulations for relieving tumor hypoxia to realize the full potential of photodynamic therapy.

1.6.3. Chemodynamic therapy

The tumor microenvironment (TME) is regarded as an aggressive and turbulent battlefield of heterogeneous mixture of different molecules, which are always engaged in the decisive interplay with cancer cells to enhance its malignant features (Zhao *et al*., 2012). The changes occurring in tumor microenvironment is always viewed as the implication of tumor progress and metastatic dissemination. Moreover, its emergence has been regarded as the most essential indigenous integral part of tumor malignancy, resulting in the design of various therapeutic platforms targeting the host vesicles of tumors to destroy the cancer cells (Chen *et al.*, 2017). Thus, owing to its general characteristics like hypoxia, acidity and peroxide production, various stimuli responsive strategies like hypoxia targeted therapy, pH responsive starvation therapy, oxidative responsive chemotherapy have gathered more attention in the recent past (Liu *et al*., 2014).

Among various stimuli responsive formulations, exogenous reactive oxygen species (ROS) such as singlet oxygen ($^1O_2$), hydroxyl radical (HO•) and peroxide (O_2^{2-}, $O_2^{\bullet-}$) are considered as potentially effective and precise tools, but widely untested alternative for cancer therapeutics (Ushio-Fukai *et al*., 2008). These ROS species are predominantly generated either from molecular drugs or through PDT and biochemical reactions, where PDT was the major clinically tested ROS mediated strategy, relying mainly on the singlet oxygen production through light activation of photosensitizers. Unfortunately, PDT has shown poor response in clinical scenario, which is mainly due to the low solubility and aggregation of photosensitizers in body

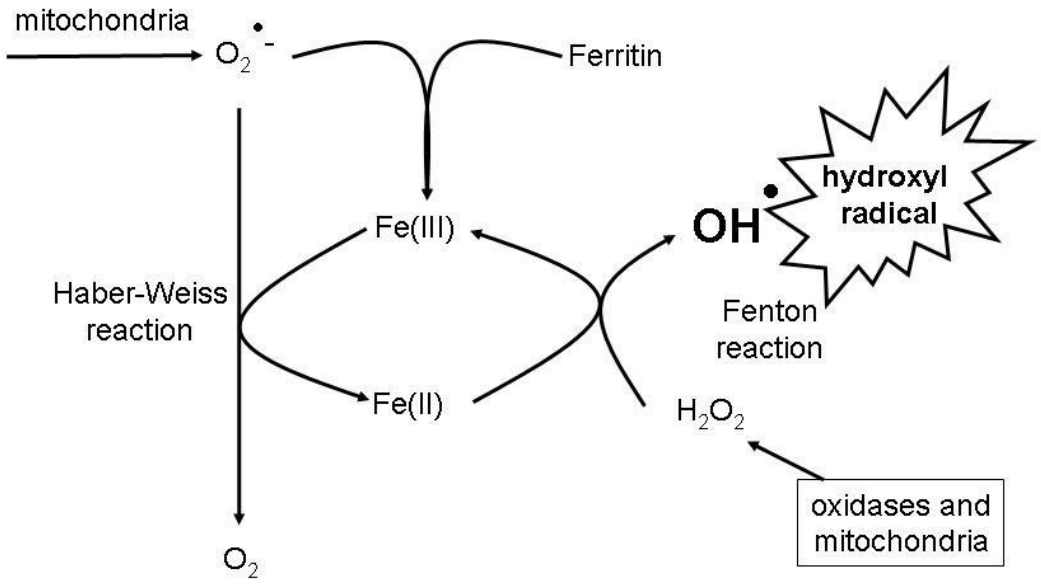

Figure 9. Schematic illustration of the various chemical processes involved in chemodynamic therapy. Adopted from (Kell *et al*., 2010).

fluids, ineffective tissue penetration of light and depending on the passive uptake of photosensitizers by tumor tissues. Moreover, the most intrinsic limitation of PDT is primarily due to the poor therapeutic outcome in oxygen deficient tumor tissues, whereas most of the TME tends to be hypoxic in nature (Fingar *et al.*, 1992).

In virtue of the limitations suffered by PDT, a biochemical reaction triggered by ferrous ion, namely Fenton reaction, which readily consumes hydrogen peroxide (H_2O_2) and produce highly reactive and toxic hydroxyl radical (HO•) has emerged

as a decisive therapeutic tool. Thus, chemodynamic therapy (CDT) surmounts the constraints of non-specificity and penetration issues and induce cell death through the generation of highly reactive HO•, from the endogenous chemical energy of intratumoral Fenton reaction (Figure 9) (Zhang *et al.,* 2016). Moreover, CDT operates completely inoffensive in normal tissues, since it utilize the internal TME conditions for the *in situ* production of free radicals and redox homeostasis that will also help to tackle the oxidative damage from the radical reaction to avoid the death of normal healthy cells.

1.7. Graphene-gold nanohybrids as a theranostic tool

Owing to the potential in real time diagnostic capabilities, theranostics, an integrated form of imaging and therapy, plays a decisive pivotal role in personalized cancer treatment. Fabrication of cost-effective theranostic nanoagents with minimal side effects and precise targeting at therapeutic window with enhanced efficacy can be considered as the thrust area in nanomedicine (Peer *et al*., 2007). But, effective diagnosis guided targeted therapy in a single nanocapsule still remains a dream in the development of potent multifunctional nanoprobes for heterogeneous diseases like cancer. The development of these promising nanoscale engineered theranostic nanoprobes has been hindered by the lack of personalized approach and precise monitoring in clinics. Even though, chemotherapy stands to be a mainstream cancer treatment, drug resistance, low accumulation in the tumor tissues and adverse side effects downside its significance (Greco *et al.,* 2009). To overcome the intrinsic limitations of chemotherapy, it can be integrated with various modalities like photothermal therapy (PTT) and photodynamic therapy (PDT) which can perform accurately at highly complicated therapeutic window, orchestrating enhanced efficacy with minimized off-target side effects (Yu *et al*., 2016) (Ni *et al*., 2014) (Fan *et al*., 2013) (Nair *et al*., 2015). Moreover, it is of prime importance to integrate non-linear optical imaging agents that could effectively couple light harvesting signals with these multimodal therapeutic modalities to better understand disease state with pronounced productivity. Thus, with the emergence of personalized treatment and

enormous demand, it is high time to develop nanoformulations with candid clinically relevant regime to deliver “targeted theranostic” nanoplatforms.

In the last few decades, nanomedicine has achieved an appreciable advancement in registering a hall mark in the medical field and several classes of nanomaterials have been adjusted to the early stages of clinical testing (Rizia *et al*., 2011). For example, biocompatible nanocarriers like dendrimers, liposomes, inorganic nanoparticles and polymeric micelles can offer reduced toxicity and better biodistribution with various imaging tools (e.g., computed tomography (CT) contrast agents, upconversion particles, organic dyes, MRI contrast agents, quantum dots etc.) and with various therapeutic agents (anticancer drugs, proteins, deoxy ribonucleic acid (DNA), siRNA, hyperthermia-inducing agents, photosensitizers etc.) (Li *et al*., 2006). However, most of the theranostic functional nanomaterials developed so far were able to couple only few of these clinical functions and have concerns over complex fabrication, targeted delivery of payloads, auto-fluorescence, depth of tissue penetration and multiplexing, which hindered the further development of “theranostics” in clinical scenario.

Recently, carbon nanomaterials have exhibited a tremendous progress and entered into a phase of maturity in their biomedical development and established itself by explorative usage in various applications from tissue engineering to cancer theranostics (Liu *et al*., 2012). Among them, graphene has sparked undeniable potential for multifunctional applications due to its intrinsic physicochemical and structural properties. By virtue of its large surface area, biocompatibility, strong near infra-red (NIR) absorption and presence of different functional groups and domains, graphene and its derivatives (i.e., graphene oxide and reduced graphene oxide) could provide an ideal support for controlled drug delivery, PTT and act as efficient cargo for various theranostic and targeting payloads (Zhang *et al*., 2010). Moreover, it can also provide a platform for SERS imaging through chemical enhancement, due to its surface plasmon in the terahertz range (Murphy *et al*., 2013). But its photothermal conversion ability and Raman enhancement is below par as compared to that of plasmonic gold nanostructures (Chou *et al*., 2005). These structures facilitate strong

photoabsorption through the excitation of their localized surface plasmon resonance (LSPR), which in turn is responsible for their enhanced SERS and photo thermal effect. Gold nanostructures and exfoliated graphene themselves have been proven to be promising substrates for properties like PTT, drug delivery, SERS etc. (Echtermeyer *et al*., 2008) However, their hybrid plasmonic gold-graphene assemblies are regarded as alluring "hot carriers", where gold nanostructures act as antennas to utilize its surface plasmon resonance and wake up the innate near field coupling between graphene carriers to facilitate new avenues with pronounced effect that may provide synergistic clinical outcome in theranostics (Cai *et al.,* 2015). They can perform a definite dual-enhanced effect which stands as a biodegradable and biocompatible nano-regime for the targeted release of various payloads. So, it is important to design a hybrid nano-regime, intelligent enough to tackle the biological *in vivo* conditions to perform its inherent properties and able to deliver the biomedical payloads to the targeted site with high specificity.

1.8. Development of a clinical screening tool for personalized treatment applications

In view of the crucial role played by tissue biopsy in examining heterogeneous diseases like cancer, biomedical and clinical research community has integrated it with best treatment options for tailoring personalized diagnosis and efficient treatment. But the entire 'picture' of the tumor is often masked by less tumor accessibility due to clinical complication to obtain the tissue at the point of initial diagnosis as well as during the course of treatment (Diaz *et al*., 2014). Moreover, invasive tissue biopsy data obtained from limited amount of collected tissues are often expensive and biased which makes it difficult for conducting repeated diagnosis that can lead to wrong clinical decisions. Even though tumor tissue is regarded as the gold standard source for clinical molecular investigations, in light of its limitations to study the tumor genetics and dynamics, cancer driven materials circulating in the blood plasma has emerged as a potent alternative to overcome some of the above mentioned challenges (Schroeder *et al*., 2012). Thus, "liquid biopsy"

has gained significant attention as promising diagnostic procedure for identification and quantification of cancer driven materials present in the blood stream.

Key targets employed in liquid biopsy include various circulating biomarkers such as circulating tumor cells, circulating vesicles, circulating nucleic acid and circulating proteins. Conventionally these biomarkers are detected either by traditional protein (western blot, radioimmunology, mass spectrometry, flow cytometry, immunofluorescence imaging) or nucleic acid (polymerase chain reaction and reverse transcription polymerase chain reaction) based techniques. But it is technically complicated and lacks specificity, although it provides great advancements in circulating biomarker sensing (Alix-Panabières *et al*., 2013).

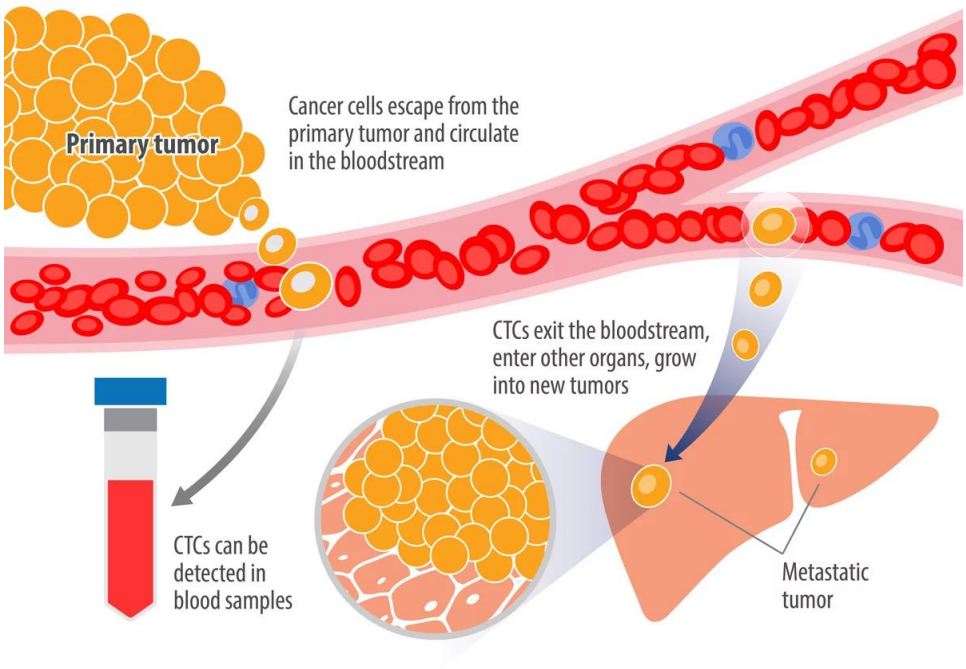

Figure 10. Scheme representing the invasion and migration of circulating tumor cells to metastasis. Adopted from online (https://blog.crownbio.com/ctc-metastasis-mouse-models).

Among various circulating biomarkers, circulating tumor cells (CTCs) show great promise in early detection of cancer, since they are prognostic markers which are present in the blood plasma during the early stages of tumorigenesis (Figure 10) (Zhang *et al*., 2012). During the past two decades, CTC has received tremendous

attention as a hallmark analyte for the non-invasive real time liquid biopsy technique, as a result of which more than 270 clinical trials have already been registered utilizing this biomarker. Furthermore, CTC has been well documented as a prognostic marker for breast cancer and its detection has great insight into the evaluation of metastatic relapse and progression in other tumor entities. Thus far, FDA has approved only one technology, mainly the CellSearch system (Veridex, LLC) for clinical usage. It utilizes ferrofluid nanoparticle attached EpCAM antibody for the magnetic separation of CTC from blood plasma and detect it through immunofluorescence imaging. Although it can be used to detect CTC in patients with breast, prostate and colon cancer, it proves to be successful in identifying only 50% of patients with known metastasis. It still remains extremely challenging to develop a system to count and detect the CTC in cancer patients as it is present as low as 1-10 CTC/mL of blood plasma (Hong *et al*., 2013).

Nanotechnology and nanosensors open up new perspectives for the development of ultra-sensitive and specific biosensors for the detection of CTC by utilizing its exceptional functional attributes and target interactions as compared to the bulk materials. Since, these materials have the ability to accommodate more ligands with higher densities, they can capture CTC through ligand-antigen interaction and thus improve the multivalent effects and lead to enhanced binding affinity. Different types of nanostructured substrates have been reported for CTC enrichment mainly nanoarray, nanosheet, nanofiber and nanoporous substrates etc. Among them, anti-EpCAM tagged magnetic beads are currently used to enrich and isolate CTC population. These magnetic beads can form a bead-cell conjugate which facilitate the isolation of CTC through classical magnetic separation. Although, this method is successful in capturing CTC, it failed to quantify the amount of tumor cells in the blood stream (Wang *et al*., 2011).

1.9. Hypothesis

Recent advancements in nanotechnology and material science have boosted the development of a glut of materials with distinctive physico-chemical features for biomedical applications. Graphitic nanomaterials such as fullerenes, carbon

nanotubes and more recently, graphene and its derivatives like graphene oxide and reduced graphene oxide have established a pronounced interest in this area. Besides the unique physico-chemical properties of these materials, the presence of various functional groups (-COOH, -OH, -O- etc.) on their basal plane and excellent biocompatibility makes them an ideal candidate for biomedical applications. On the other hand, gold nanostructures have also gathered a great attention due to their phenomenal properties and applications in biomedical imaging, catalysis, sensing etc. Thus, loading of graphitic (GO or rGO) nanosheets with gold nanostructures opens a new avenue for the generation of functional metamaterials with enhanced properties in theranostic and diagnostic applications. This thesis is designed based on the above backgrounds with a hypothesis that graphene-gold hybrids will be a suitable candidate that can provide an insight into the development of various multifunctional nanoconstructs for theranostic and diagnostic applications.

1.10. Objectives

The objectives of the current study are

- Development and characterization of various plasmonic graphene-gold nanohybrids.
- Detailed evaluation of tumor imaging and therapeutic efficacies of the as-developed graphene-gold nanohybrids.
- Investigation of imaging efficacies of graphene-gold hybrids through surface enhanced Raman scattering, fluorescence, magnetic resonance imaging etc.
- Evaluation of therapeutic properties of graphene-gold nanohybrids through photothermal therapy, photodynamic therapy, photo-chemo therapy and chemodynamic therapy.
- Evaluation of theranostic capabilities of graphene-gold nanohybrids in *in vitro* and *in vivo* models.
- Development of a diagnostic tool using graphene-gold nanohybrids for the detection of circulating tumor cells from blood as a liquid biopsy kit.

Chapter 2

Review of Literature

Chapter 2

Review of Literature

2.1. Graphene-gold nanohybrids for biosensing and bioimaging

Since the development of gold nanoparticle decorated graphene and its derivatives have been accomplished, they are considered as one of the important futuristic materials for various biomedical applications. The innate properties of these hybrids are tip to replace many of the current materials and techniques which lack the multi-functionalities demanded by heterogeneous diseases like cancer. In the field of cancer diagnostics and therapy, these nanohybrids have shown pronounced effect in bioimaging, electrochemical sensing, photothermal therapy, drug delivery, gene delivery, chemo-photothermal therapy etc. Actually, the surface plasmon resonance property of gold nanostructures and the diverse photo-physical properties of graphitic materials are the spine of their applications. For example, properties like SERS have huge hand in their biosensing and imaging capabilities. In the following section, we will discuss in detail the origin and development of SERS properties of graphene-gold nanohybrids and their immense potential in biomedical applications.

SERS is actually a non-invasive spectroscopic technique which couples the current laser spectroscopic methods with the optical and plasmonic properties of metallic nanoparticles, to assist the most effective means to dramatically increase the Raman signal of reporter molecules tagged on the roughened surface of metal nanostructures (Kneipp *et al*., 1997). Thus, SERS has been extensively utilized in diverse biomedical fields like biosensing and diagnostics. Unlike other spectroscopic techniques, SERS provides high sensitivity and multiplexing capabilities, and thus well employed for the processes that require very minute detailing like identification of proteins, genes, cancer cells, biomolecules, investigation of single molecule interactions (Sun *et al*., 2015) and lot more.

Traditionally, gold and silver nanoparticles are used as the trademark SERS substrates. Anisotropic structures of these metal nanoparticles like nanopopcorns, nanostars and nanorods which exhibit distinct surface plasmon band have proved to be excellent SERS agents (Wang *et al*., 2013). However, recent studies have suggested that graphene and its derivatives can also be used as SERS substrates similar to various plasmonic nanostructures. The SERS property of graphene (G-SERS or GERS) was discovered accidentally by Ling *et al* (Ling *et al*., 2009) during the mechanical exfoliation of graphene in organic solvents. He observed several emerging bands from the graphene during the process. The G-SERS experiments of phthalocyanine showed its enhanced Raman signals due to the presence of graphene. Actually, graphene and its derivatives don't fall into the category of traditional SERS substrate since it doesn't have electromagnetic contribution naturally found in plasmonic nanostructures. Thus, G-SERS of graphene was originated through the chemical enhancement process. Moreover, G-SERS contribution majorly depends on the chemical nature of graphitic materials. For example, GO exhibits more Raman enhancement as compared to the graphene sheets. Therefore, the coupling of graphitic materials with plasmonic nanostructures will provide a dual Raman enhancement due to the combined effects of electromagnetic and chemical enhancements. Hu *et al*. recently compared the intensity of Raman signals of dye molecules like crystal violet onto Au NRs, GO and Au NR–graphene nanohybrids and confirmed the enhancement of G-SERS signal of Au NR–graphene nanohybrids (Hu *et al*., 2013).

2.1.1. Biosensing applications

Graphitic materials have been extensively utilized for the detection of bioanalytes like amino acids, dopamine, and various other biomolecules. These materials basically utilize different properties like plasmonic, electrochemical, field effect transistor (FET) and fluorescence resonance energy transfer to perform its sensing based assays. Electrochemical sensors are exhibiting dominant trends in biomedical applications. The graphene-gold nanohybrids have enormous impact in electrochemical sensing especially using its inherent SERS technique. The coupling of gold nanostructures with graphitic materials will enhance the sensitivity and

detection limit owing to the reaction with specific analyte or improved electron transfer in the system. Currently, glucose sensing platforms are the most common sensors fabricated using graphene-gold nanohybrids. Shan *et al.* utilized glucose oxidase immobilized chitosan-GO-Au composite as an electrode for glucose detection (Shan *et al*., 2010). Their sensor showed glucose detection limit up to 180 µM. In another report, Fang *et al*. utilized cationic poly (diallyl dimethyl ammonium chloride) (PDDA) tagged GO-Au nanocomposite for the detection of hydrogen peroxide (Fang *et al*., 2010). They were able to achieve the detection limit up to 0.44 µM. The superb performance of the sensor was owing to the high loading of the Au

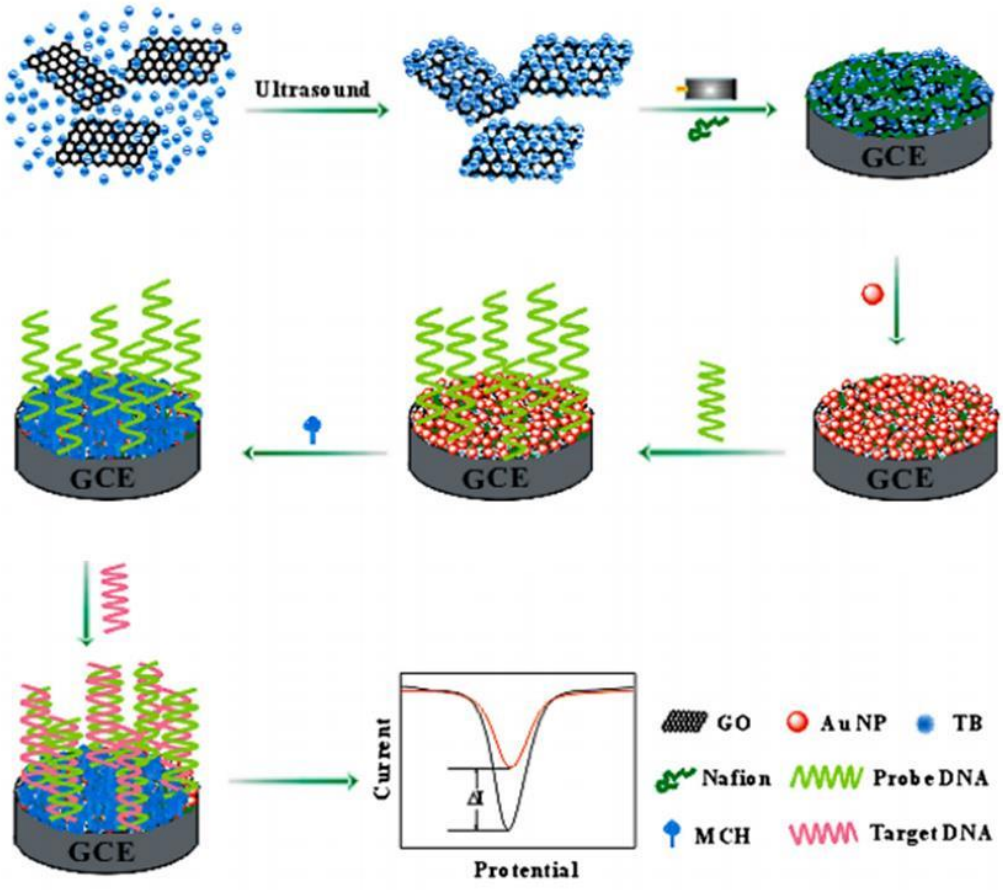

Figure 11. Fabrication and detection process of DNA sensor for rapid detection of multi-drug resistant gene based on Au nanoparticles/toluidine blue–graphene oxide nanocomposites. Adopted from (Peng *et al*., 2015).

nanoparticles over the GO sheets. On the other hand, Jiang *et al.* utilized graphene-Au nanohybrids for the detection of hydrogen peroxide inside living cells. Their

investigation proved that the concentration of hydrogen peroxide in cancer cells is several fold higher than the normal cells (Jiang *et al*., 2014). Another common electrochemical sensing platform performed using graphene-Au nanohybrid was DNA sensing. Mandler *et al.* showed that thiolated DNA can be easily attached on to the surface of graphene-Au nanohybrids. This hybrid can be used as a target point for sensing target DNA (Mandler *et al*., 2012). A DNA sensor of Au nanoparticle/toluidine blue-rGO nanocomposite was fabricated by Peng *et al.* In this study, the hybridization of DNA was measured by monitoring the variation in peak current of toluidine blue (Figure 11) (Peng *et al*., 2015).

Similar to electrochemical sensing, Chen *et al.* utilized FET sensor for the detection of proteins using graphene-gold nanohybrids. Gold nanoparticle decorated reduced graphene oxide was used to tag the anti-immunoglobulin G (IgG) to detect the target proteins. They obtained the detection limit up to 13 pM, which is best among the sensors of various carbon based materials. The sensor also exhibited high selectivity among the mismatched proteins (Chen *et al*., 2011).

2.1.2. Bioimaging applications

Recently, graphene-gold nanohybrids have also shown their prospective in bioimaging. The innate SERS imaging efficacy of these nanohybrids enabled in establishing themselves over the conventional methods of bioimaging owing to their superior attributes like sensitivity, multiplexing properties and stability. For example, Ma *et al.* formulated a coupled nanosystem of GO and gold nanoparticles (AuNPs@nGO), capable of intracellular Raman mapping of HeLa cells. The detailed internalization of AuNPs@nGO was investigated through SERS imaging wherein they found out that the material uptake happened through an energy-dependent process known as endocytosis. The results indicated that AuNPs@nGO was mainly distributed in the cytoplasm which gets internalized into the sub-cellular level of each cell to furnish localized detection and imaging (Ma *et al.*, 2013).

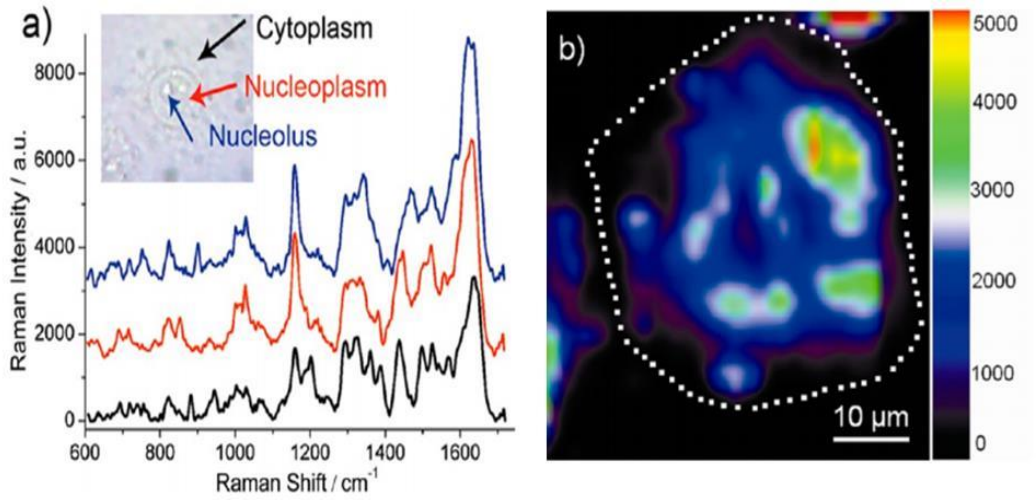

Figure 12. a) SERS spectra and b) SERS image showing the intracellular localization of GO/PVP/IGAuNs in A549 cells Adopted from (Guo *et al*., 2009).

In addition to that, Liu *et al.* found that GO-Au nanohybrids displayed much distinguishable and strong Raman signals in the HeLa cells as compared to the pristine GO (Liu *et al*., 2010). Meanwhile, Guo *et al.* reported the synthesis of one-pot intracellular formation of gold nanoparticles assisted by poly (vinylpyrrolidone) (PVP) tethered GO (GO/PVP/IGAuNs). This indeed allowed the monitoring of sensitive intracellular chemical configurations such as cytoplasm, nucleoplasm and nuclei using SERS imaging (Figure 12) (Guo *et al*., 2009). Zhang *et al*. also employed SERS to understand the mechanism of intracellular uptake of GO@Au nanoparticles. A non-homogeneous distribution of nanoprobe was observed inside the cell via clathrin-mediated endocytosis (Zhang *et al*., 2012). Recently, Kim *et al.* used 3D graphene oxide encapsulated nanoparticles for the detection of neural stem cell differentiation. The Raman peak intensity obtained from the undifferentiated stem cells was 3.5 times higher than the nanoconstruct and it can be easily distinguished from the differentiated stem cells (Kim *et al*., 2013). Bian *et al.* employed chemical vapor deposition (CVD) method for the preparation of SERS substrate by wrapping gold nanostructures inside the layer of graphene named GIAN nanostructures. GIAN was capable of intensifying Raman signals to several orders of magnitude by diminishing the background fluorescence. It was then utilized for the SERS imaging of MCF-7 breast cancer cell lines which showed good distribution

inside the cytoplasm (Figure 13) (Bian *et al*., 2014). Wang *et al*. has utilized rGO-Au nanostar as a potential Raman substrate for the loading and release of anticancer drug, doxorubicin (DOX). The nanoprobe displayed promising potential for monitoring the release of therapeutic drugs during the chemotherapy treatment (Wang *et al*., 2014).

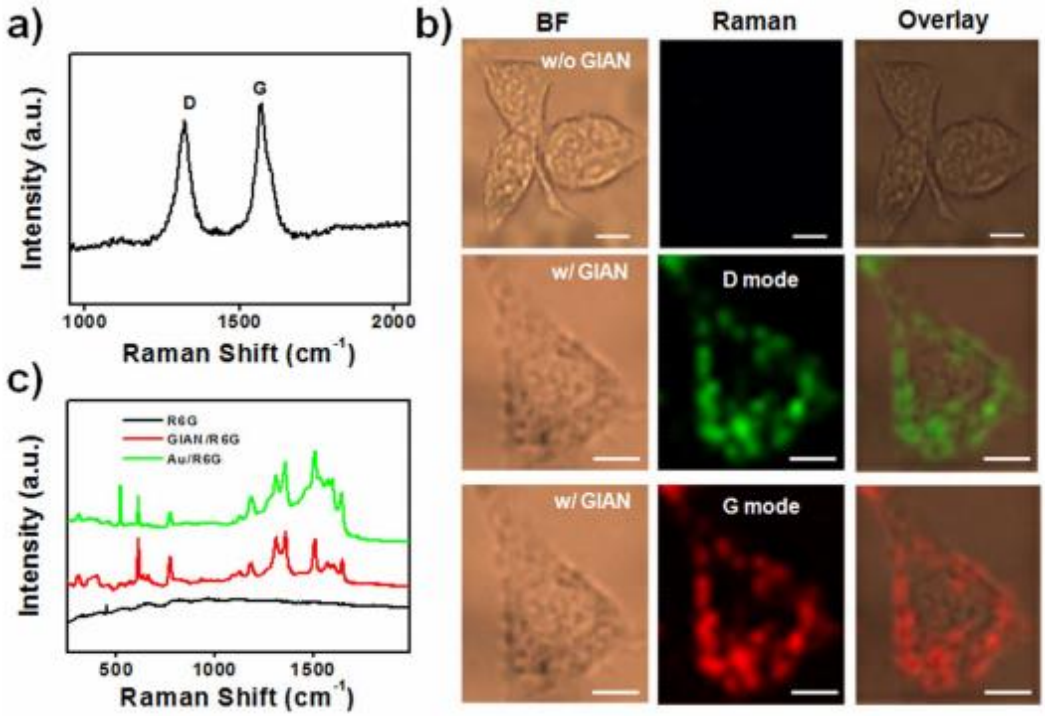

Figure 13. (a) Raman spectrum of D and G bands of graphene. b) Raman imaging of MCF-7 cells with and without GIAN and c) Raman spectra of rhodamine 6G with and without GIAN, and with gold nanoparticles, respectively. Adopted from (Bian *et al*., 2014).

2.2. Therapeutic applications of graphene-gold nanohybrids

Graphitic materials opened up exciting avenues for various therapeutic strategies and platforms in the recent past. They can be utilized as excellent cargoes for different insoluble chemotherapeutic drugs and genes owing to their high surface area (2630 m^2 g^{-1}), 2D planar structure and availability of various types of interactions like covalent or π-π stacking with loading molecules. In addition to that, they have strong absorption in the NIR region which brings out more benefits for biomedical applications.

Among various graphitic materials, graphene-gold nanohybrids exhibit higher photoabsorption in the NIR region. This enhanced effect is due to the coupling effect of gold nanostructures and graphene substrate present in the system. The strong absorption of nanohybrids in the NIR region can be utilized for therapeutic strategies like PTT. PTT relies on the absorption of light energy by the NIR absorbing agents which then converts it into heat energy to cause thermal ablations of pathogens and cancer cells. Even though reduced graphene oxide exhibits six times higher photoabsorption in the NIR region than graphene oxide, its broad absorption and low quantam efficiency denied its widespread applications in specific wavelength. As a result, graphene-gold nanohybrids were introduced as new PTT agents in order to overcome these limitations. These nanohybrids have exceptional photoabsorption in the NIR region due to its surface plasmon resonance properties. Moreover, their plasmonic wavelength can be adjusted through the fabrication of suitable anisotropic gold structures. El-Shall *et al*. fabricated highly water soluble photothermal agent through coupling of gold anisotropic structures with graphene sheets of controlled size (El-Shall *et al.,* 2013). They were the first to observe the enhanced photothermal effect of gold nanostructures coated with graphene oxide in the NIR region. When irradiated with NIR laser, gold anisotropic structures like gold nano-shells and nanorods coated with graphitic materials exhibited strong photothermal effects. *In vitro* application of these nanocomposites was examined using human umbilical vein

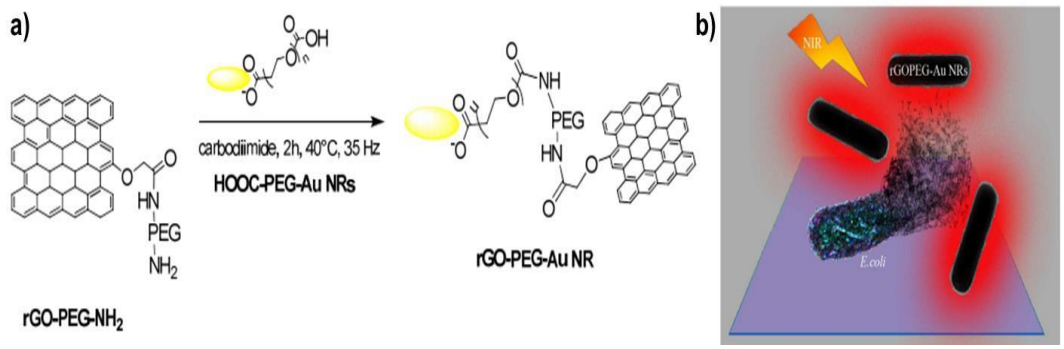

Figure 14. a) Synthetic strategy towards the development of gold nanorods embedded GO. b) Schematic illustration of gold nanorods embedded GO for the detection and selective killing of uropathogenic *E. coli* UTI89. Adopted from (Turcheniuk *et al*., 2015).

endothelial cells. In the absence of laser irradiation, cells showed negligible toxicity but severe toxicity was observed upon the application of laser (808 nm, 3 W/cm^2). Photothermal response towards cancer cells by aptamer conjugated gold nanoparticle embedded graphene oxide was reported recently showing the targeted phototherapeutic response of graphene-gold nanohybrids. More recently, gold nanorods embedded GO were utilized for the detection and selective killing of uropathogenic *E. coli* UTI89 (Turcheniuk *et al*., 2015). The selective killing of the *E. coli* was achieved by tagging multimeric heptyl ὰ-D-mannoside probe with the nanohybrid (Figure 14). This technique offered a highly biocompatible pathogen ablation method for the clinical application of patients with urinary infections.

Figure 15. Schematic representation of the design and development of NGOHA-AuNRs-DOX for combined photothermal chemotherapeutic applications. Adopted from (Xu *et al.*, 2013).

In addition to photothermal therapy, graphene-gold nanohybrids were also utilized for laser induced chemotherapeutic applications. Xu *et al.* designed hyaluronic acid modified gold nanorods-GO system for loading of chemotherapeutic

drug, doxorubicin (NGOHA-AuNRs-DOX) (Figure 15) (Xu *et al*, 2013). The combined photothermal-chemotherapeutic strategy exhibited four fold higher cell death as compared to the individual therapies. Similar to the above work, graphene-Au nanocrystals have been developed for the efficient loading of doxorubicin for chemo-PTT. Chemotherapeutic effect of the nanoconstruct with and without laser displayed huge difference as laser ablation caused higher cell toxicity. Recently, poly ethyleneimine (PEI) coated graphene oxide-gold nanostructures have been used for gene delivery applications. The efficiency of the hybrids was as high as 65%. Interestingly, HeLa cells incubated with the nanohybrid showed 90% cell viability whereas cells incubated with PEI alone showed toxic effects. In another report, Yuan and colleagues explored the anticancer effect of micro-RNA-122 on drug resistant liver cells through integration with GO-Au nanohybrids. More importantly, the integration of monoclonal P-glycoprotein antibodies, microRNA-122, and folic acid with Au@GO nanohybrids were utilized to promote apoptosis in HepG2 cells via a target specific and controlled drug release fashion (Yuan *et al*., 2015).

Chapter 3

Materials and Methods

Chapter 3

Materials and Methods

In order to fulfill the objectives of the current study, we have developed various nanohybrids of graphitic materials with gold nanostructures. These nanohybrids were designed specifically for the site specific imaging tailored therapeutic actions and sensing applications. The detailed description of various synthesis strategies and techniques used for the above work is given in this chapter.

3.1. Synthesis of graphene-gold nanohybrids as targeted theranostic nanoprobe (TTNP) for dual modal imaging guided triple therapy

3.1.1. Materials and reagents

Auric chloride ($HAuCl_4$), graphite flakes, protoporphyrin IX (PpIX), chitosan (CS), doxorubicin hydrochloride (DOX) and trisodium citrate (TSC) were purchased from Sigma Aldrich. Sodium borohydride ($NaBH_4$), phosphoric acid (H_3PO_4), dimethyl sulphoxide (DMSO), sulphuric acid (H_2SO_4), folic acid (FA) and sodium hydroxide (NaOH) were purchased from MERCK. All the chemicals were used as such without any further purification. Absorption and IR spectral measurements were carried out on a Shimadzu (UV-1800) UV-Vis spectrometer and FTIR Carry 600 (Agilent Technologies) respectively. Emission spectra were recorded on a FP-8200 Jasco spectrofluorometer and zeta potential measurements were obtained from nano ZS (Malvern, UK). We utilized an inverted fluorescence microscope (IX83; Olympus Corp., Tokyo, Japan) with a cooled CCD camera (XM10, monochrome, Olympus) for the *in vitro* fluorescence experiments and SERS experiments were performed on a WITec confocal Raman microscope with an integration time of 1s and 10 accumulations. *In vivo* and the *ex vivo* animal imaging was carried out with a live animal optical imaging system (Xenogen, IVIS Spectrum).

3.1.2. Preparation of spherical gold nanoseed loaded rGO (Au-rGO)

Graphene oxide was synthesized through modified Hummers method. Synthesis of Au-rGO was carried out using a reported procedure with suitable modification. Initially, 1 mL of GO solution (4 mg/mL) was dissolved in water (50 mL) and mixed with 100 µL of $HAuCl_4$ (0.1 M) and stirred for 1 hour. The solution was then heated at ~80 ^oC followed by drop by drop addition of 500 µL of sodium citrate (0.1 M). The final mixture was then kept undisturbed for 1 hour to attain uniform decoration of gold nanoseed over the surface of graphene.

3.1.3. Preparation of spiky gold nanostar loaded rGO (Au-rGO NS)

100 µL of the above prepared citrate stabilized Au-rGO seed solution was added to a 10 mL growth solution containg $HAuCl_4$ (0.25 mM) and 10 µL of HCl (0.1 M) under moderate stirring at room temperature. Then, 64 µL of silver nitrate (0.01 M) and 67 µL of ascorbic acid (0.1 M) were added rapidly to the above solution. Immediately after the addition of latter, colour of the solution changed from red to blue indicating the formation of spiky gold nanostar on the surface of reduced graphene oxide with strong NIR absorption. The obtained solution was finally centrifuged at 5000 rpm for 10 minutes, washed several times and kept at 4 ^oC until use.

3.1.4. Synthesis of chitosan-protoporphyrin IX conjugates (CS-PpIX)

Protoporphyrin IX conjugated chitosan was synthesized through EDC/NHS coupling. Briefly, PpIX (10 mM) and EDC (30 mM) were dissolved in 2 mL DMSO and stirred for 2 hours. Then, 30 mM of NHS was added slowly in to the above solution, followed by the addition of 8 µM chitosan dissolved in 10 mL of sodium acetate/acetic acid buffer (pH= 5.2). After stirring for 24 hours, the above solution was subjected to dialysis for 3 days against 1:3 v/v of methanol/water system (molecular cut off = 12-14 kDa) to remove unbound photosensitizer from the chitosan solution and lyophilized to get it as a fine powder.

3.1.5. Folic acid coupling of chitosan-PpIX conjugates (CS-PpIX-FA)

About 8.75 mg of FA and 3.12 mg of EDC were dissolved in 2.5 mL of anhydrous DMSO for 2 hours with gentle stirring. 0.5% of CS-PpIX was then added to the

above solution and stirred overnight under 3^{o}C. The final solution was brought to pH ~9 and subjected to dialysis and subsequently followed by centrifugation at 5000 rpm for 15 minutes which was finally lyophilized to get it in powder form.

3.1.6. Synthesis of TTNP (Au-rGO@CS-PpIX-FA)

100 µL of CS-PpIX-FA (1 mg/mL) nanoparticle was allowed to mix with Au-rGO NS (0.1 mg/mL) through bath sonication for 1 hour. The resulting solution was incubated for 30 minutes to ensure the effective loading of CS-PpIX-FA on the surface of reduced graphene oxide, electrostatically. Final mixture was then centrifuged at 9000 rpm for 30 minutes to remove the excess chitosan conjugate and the residue was washed with double distilled water for several times.

3.1.7. Preparation of DOX loaded TTNP (TTNP-DOX)

For drug loading, different ratios of **TTNP** (0.1 mg/mL) to DOX (1:25, 1:1, 1:0.50, 1:0.25) were mixed together and subsequently sonicated for 30 minutes and kept for overnight stirring. Non-entrapped drug in the supernatant was then separated through centrifugation at 25000 rpm for 30 minutes. Loading content and encapsulation efficiency was examined by piloting the characteristic photoluminescence of DOX centered at 590 nm which were calculated as follows:

$$\textbf{Drug loading content (\%)} = \frac{\textbf{Wt.of drug in TTNP} * \textbf{100}}{\textbf{Wt.of TTNP}}$$

$$\textbf{Encapsulation efficiency (\%)} = \frac{\textbf{Wt.of drug in TTNP}}{\textbf{Wt.of total drug}} \textbf{*100}$$

3.1.8. Dual responsive drug release from TTNP-DOX

Photothermally induced and pH responsive drug release experiments were accomplished by dispersing **TTNP-DOX** in PBS (pH = 5, 7.4) with and without laser irradiation (1 W/cm^2, 808 nm). The mixture was then incubated in a water bath at 37 ^{o}C with continuous shaking from which 1 mL of supernatant was collected at definite time intervals and replaced with the same volume of fresh media. Drug released from the nanocarrier was quantified by recording the emission spectra of dialysate at 590 nm.

3.1.9. NIR laser-triggered photothermal efficacy of TTNP

The photothermal efficacy of **TTNP** was evaluated by taking various concentrations of **TTNP** (6.25, 12.5, 25, 50, 100 µg/mL) and irradiated with an 808 nm laser at different power densities (0.5, 0.75 and 1 W/cm^2 respectively) for 10 minutes.

3.1.10. Determination of singlet oxygen efficiency of TTNP

Singlet oxygen generated from the **TTNP** was detected via the quenching of absorption of 1, 3-diphenylisobenzofuran (DPBF), which is widely used as the trapping agent. In our work, a solution of **TTNP** and PpIX were dissolved in methanol and mixed with 10 µL DPBF and subjected to laser irradiation (532 nm, 0.1 W/cm^2). Decrease in absorption of DPBF at 410 nm was monitored at predetermined time intervals. Singlet oxygen efficiency was calculated from a plot of ΔA versus irradiation time.

3.1.11. Fluorescence quenching and recovery effect of TTNP

Fluorescence quenching and recovery status of **TTNP** in intracellular conditions were mimicked using 5% sodium dodecyl sulfate (SDS). Fluorescence intensity of various concentrations of PpIX, **TTNP** and **TTNP**+5% SDS (6.25, 12.5,25,50,100 µg/mL, respectively) were quantified.

3.1.12. Cellular experiments

The triple negative breast cancer MDA-MB231 cell lines were thawed from cryo-preservation and were added to 5X volume of DMEM to neutralize the cryo-preservation medium. This was centrifuged at 3000 rpm for about 3 minutes and the pellet thus obtained was resuspended in 1 mL of complete DMEM, seeded into T25 flasks and incubated at 37 ºC and 5% CO_2 until 90% confluency. A series of cryo-preserved cells in liquid nitrogen was made from the first passage and was used for all further experiments. DMEM basal medium along with 5% serum and supplemented with 1% of penicillin-streptomycin solution was used in the culturing procedure. For all the following experiments, the cryo vials were thawed and seeded into T25 flasks and allowed to grow. After reaching 90% confluency, the cells were trypsinized and plated on to the required type of culture well plates.

3.1.13. Cell viability studies

The cells after two passages were seeded on to a 96 well plate and incubated at 37 ºC for 24 hrs. The cells after incubation were treated for 24 hrs with different concentrations of **TTNP**, ranging from 6.25-200 µg/mL in serum free media. After the treatment period, the material solution was replaced with 90 µL of fresh medium along with 10 µL of MTT reagent (5 mg/mL) for 4 hrs. Again after this period of MTT treatment, the cells were treated with 100 µL of DMSO and allowed to sit for 30 minutes. The absorbance was measured at 570 nm using a micro plate reader.

In order to evaluate the cell viability under laser treatments, individual (808 nm or 532 nm) and combined laser powers (808 nm + 532 nm) were irradiated on the cells treated with the constructs and then incubated for 30 minutes to induce the therapeutic effect. After the treatment period the same procedure was adopted for finding out the cell viability as explained above.

3.1.14. Cellular uptake studies

The cells collected after two passages were seeded on to a four well dish and allowed to proliferate. After proliferation, the cells were treated with the standardized concentration of **TTNP** and incubated for different time intervals ranging from 30 to 120 minutes. After the incubation, the fluorescence of the material was checked using an epi-fluorescence microscope (DAPI, HcRED). Similarly, intracellular release of DOX with respect to different time intervals of incubation was also evaluated. The cells were seeded into 4 well dishes and grown to maximum confluency. Later, to the cells, DOX was added and incubated for a range of different time intervals starting from 2 hours to 6 hours. Images were taken to highlight the fluorescence shift from cytosolic region to nuclear region (DAPI, HcRED).

3.1.15. Intracellular ROS generation using DCFDA assay

The two times passaged cells were cultured in a 12 well dish for 24 hrs at 37 ºC. After proper growth, the cells were subjected to different treatments of **TTNP** and CS-PpIX with and without laser irradiation. After the material treatment for 4 hrs and 30 minutes post laser irradiation, the cells were treated with 25 µL of DCFDA reagent and incubated for 40 minutes. The cells were then washed and added with

color less media and images were taken using an epi-fluorescence microscope (DAPI, FITC).

3.1.16. Live-dead assay

The cells passaged for two times were seeded on to 12 well dishes and incubated for 24 hrs. The cells after reaching 90% confluency were treated with **TTNP** and **TTNP-DOX** with and without laser irradiation. The cells were then treated with both fresh serum free media along with acridine orange-propidium iodide mixture (1:1 in 1X PBS) and incubated for 30 minutes. After the incubation, the cells were washed and imaged under fluorescence microscope. (FITC, HcRED).

3.1.17. FACS analysis

The cells were seeded in to 6 well plates and was allowed to reach maximum confluency and then subjected to different treatments with DOX, **TTNP** and **TTNP-DOX** with and without laser irradiation. Alexa Fluor® 488 Annexin V/Dead Cell Apoptosis Kit was used to carry out this analysis and the protocol was followed as prescribed by the manufacturer. After the material incubation, the cells were washed with PBS and irradiated with lasers. The cells were then washed with PBS. After centrifugation, cells were syringe filtered on to FACS tubes and suspended in 100 µL of 1X binding buffer. The suspension of cells was then added with 5 µL of annexin V conjugate and 2 µL of PI (100 µg/mL) 15 minutes prior to analysis. After the incubation, the cells were washed with 1X binding buffer and again suspended in 500 µL of 1X binding buffer. The cells were then analyzed for fluorescence using BD Aria FACS.

3.1.18. *In vivo* experiments

All animal experiments were performed in compliance with the guidelines set forth by the Committee for the Purpose of Control And Supervision of Experiments on Animals (CPCSEA) and were approved (SCT/IAEC-229/MARCH/2017/91) by the institutional animal ethics committee (IAEC) of Sree Chitra Tirunal Institute for Medical Sciences and Technology (SCTIMST). 5–6 weeks old Swiss albino mice with an average body weight of ~ 33 g were rendered from Division of Laboratory Animal House (DLAS), SCTIMST. DLA tumor-bearing mice models were

established by injecting a suspension of DLA cells (1×10^6 cells/100 µL PBS) intramuscularly into right leg of the mice. The theranostic properties of **TTNP** were executed about two weeks later when the tumor volume reached ~ 0.1-0.3 cm^3 in diameter.

For *in vivo* fluorescence imaging, DLA tumor bearing mice were divided into two groups, PBS and **TTNP** (PpIX: 3 mg/kg; Au-rGO NS: 6 mg/kg) and were injected (100 µL) through tail vein. Then, fluorescence live imaging was carried out for different time intervals (0, 6, 12, 24 h) using Xenogen IVIS Spectrum optical imaging system. After imaging, all the animals were euthanized, and tumor tissue and major organs such as brain, heart, liver, spleen and kidney were collected for understanding the biodistribution through SERS spectral intensity analysis.

When the tumor volume reached about ~ 0.1-0.3 cm^3, mice were divided into seven groups for different therapeutic strategies. Group 1 was injected with PBS (control) whereas groups 2, 3 and 4 were injected with **TTNP** and groups 5, 6 and 7 with **TTNP-DOX**. After 24 h post injection, groups 1, 3, 6 and 7 were irradiated with 808 nm laser (1 W/cm^2, 5 minutes) and groups 1, 4 with 532 nm laser (1 W/cm^2, 5 minutes) respectively. The materials (PBS, **TTNP**, and **TTNP-DOX**) were then injected intravenously on the second, fourth and sixth day following the first injection. Similarly, laser ablations (808 nm and 532 nm laser) were executed after 24 h of each injection. The tumor volume measurement was then carried out for a course of 20 days to evaluate the therapeutic outcome of our nanoprobe. The tumor volume (V) measurement was calculated as length×$width^2$×0.5, where length and width corresponds to the tumor diameters in the longest and widest point, respectively. Moreover, the body weights of mice were also monitored through the study. After the evaluation of whole therapeutic effects, all the animals were euthanized and tumors as well as major organs (brain, heart, kidney, liver, and spleen) were fixed with 4% formaldehyde to carry out H&E staining to analyze the potential toxicity of our nanosystem.

3.2. Synthesis of graphene-gold nanohybrids as plasmonic magnetic nanoprobe (PMNP) for dual modal imaging assisted CDT/PTT

3.2.1. Materials and reagents

Graphite flakes, $HAuCl_4$, TSC, 4-amino thiophenol (4-ATP), $FeCl_3$ anhydrous and $FeCl_2.4H_2O$ were purchased from Sigma Aldrich. H_3PO_4, H_2SO_4 and sodium hydroxide were purchased from MERCK. All the chemicals were used as such without any further purification. Absorption and IR spectral measurements were carried out on a Shimadzu (UV-1800) UV-Vis spectrometer and FTIR Carry 600 (Agilent Technologies) respectively. We utilized an inverted fluorescence microscope (IX83; Olympus Corp., Tokyo, Japan) with a cooled CCD camera (XM10, monochrome, Olympus). We used 1.5 T whole body MR scanner (MAGNETOM Avento Tim System1.5 T, Siemens, Munich, Germany) using a 12 channel head coil for the MRI experiments and SERS experiments were performed on a WITec confocal Raman microscope with an integration time of 1s and 10 accumulations.

3.2.2. Synthesis of amine functionalized Au-rGO (Au-rGO-NH_2)

The preparation of gold nanospheres loaded rGO (Au-rGO**)** is detailed in section 3.1.2. To a freshly prepared solution of Au-rGO, 100 µL of 4-ATP (6 mM) was added and vortexed for 30 seconds. The mixed solution was kept for 1 hour for the maximum conjugation of thiol molecules over the surface of plasmonic structures. The final product was separated through repeated centrifugation at 8000 rpm.

3.2.3. Synthesis of super paramagnetic iron oxide nanoparticles (SPIONS)

Synthesis of SPIONS was carried out using co-precipitation of ferrous salts in alkaline condition. Briefly, $FeCl_3$ and $FeCl_2.4H_2O$ were taken in 2:1 ratio in aqueous solution and heated to 80 ^oC. After the complete mixing of both the salts, 1M NaOH was added slowly to the above solution. When the solution turned into black precipitate, 0.1M TSC was added to the solution as the capping agent. The entire

reaction was carried out for 2 hours. After the reaction, the SPIONS were magnetically separated and washed several times with HCl and double distilled water.

3.2.4. Fabrication of plasmonic magnetic nanoprobe (PMNP)

Au-rGO-NH_2 was conjugated with SPIONs through EDC/NHS coupling. Briefly, 2 mL of SPIONS (1 mg/mL) and 30 mM of EDC were dissolved in 3 mL aqueous solution and stirred for 2 hours. Then, 30 mM of NHS was added to the solution and followed by the subsequent addition of 10 mL of Au-rGO-NH_2 for the amide functionalization. The reaction was carried out for 24 hours and purified through magnetic separation and centrifugation.

3.2.5. Detection of extracellular Fe^{2+} ions

Initially, 1 mg of **PMNP** was dissolved in various concentration of GSH solution (0-2 mM, 1 mL). Then, the solution was kept at room temperature for 30 minutes which was followed by centrifugation to remove the **PMNP** from the solution. Further, 100 µL of phenanthroline (100 mM) solution was added to the supernatant and sustained for 15 minutes. After that, the absorbance of the supernatant was monitored through UV-visible spectrometer.

3.2.6. Extracellular oxygen generation from PMNP

H_2O_2 (30 µL, 1M) was added to 15 mL of **PMNP** (50 µg/mL) under vigorous stirring condition. The dissolved oxygen content from the solution was evaluated using a portable dissolved oxygen meter.

3.2.7. Extracellular detection of ·OH

Solutions of methylene blue (MB; 8 µg/mL), H_2O_2 (10 mM) and **PMNP**-GSH (0.5 mg/mL) were prepared at different pH. The formation of ·OH was estimated by checking the degradation of MB through monitoring its absorbance at 660 nm using a UV-visible spectrometer.

3.2.8. Photothermal properties of PMNP

Various concentrations of **PMNP** (0-200 µg/mL) solution was irradiated with 808 nm laser (1-2 W/cm^2) for 5 minutes and temperature difference was monitored every 30 seconds using a thermocouple probe.

3.2.9. Cytotoxic evaluation of PMNP

The HeLa cells were seeded on to a 96 well plate and were nursed at 37 ºC for 24 hours. The cells were then treated with various concentrations of **PMNP** (0-200 µg/mL) for 12 and 24 hours. After that, **PMNP** solution was replaced with 90 µL of medium along with 10 µL of MTT reagent (5 mg/mL) for 4 hours and the assay was performed as described in section 3.1.13.

3.2.10. Evaluation of intracellular O_2 generation of PMNP

The intracellular oxygen production of our probe was evaluated through phosphorescence imaging using a luminescent oxygen probe, $[Ru(dpp)_3]Cl_2$. After culturing HeLa cells in a 96 well plate, it was incubated with **PMNP** (50 µg /mL) for 24 h. Then it was stained with RDPP and washed with PBS. Finally the variation in red luminescence observed from the **PMNP** treated cells as compared to the control cells were taken as the quantitative as well as the qualitative measure of oxygen generated from the material.

3.2.11. Intracellular ROS detection using DCFDA assay

After culturing HeLa cells for 24 hours, **PMNP** (50 µg/mL) was incubated at different time periods (0-4 hours). Then DCFDH-DA assay was performed as described in section 3.1.15.

3.2.12. *In vitro* photothermal enhanced CDT

The HeLa cells were seeded on to 12 well plates and incubated for 24 hrs. After reaching ~90% confluency, cells were treated with **PMNP** (50 µg/mL) with and without laser irradiation. The cells were then treated with acridine orange-propidium iodide mixture (1:1) and nurtured for 30 minutes. After the incubation, the cells were imaged under fluorescence microscope.

3.2.13. FACS analysis

The cells were seeded in to 4 well plates and then subjected to **PMNP** administration with and without laser irradiation. Then FACS analysis was carried out as explained in section 3.1.17.

3.2.14. *In vivo* experiments

All animal experiments were performed in compliance with the guidelines set forth by CPCSEA and were approved (SCT/IAEC-229/MARCH/2017/91) by IAEC of SCTIMST. 5–6 weeks old Swiss albino mice with an average body weight of ~ 33 g were rendered from DLAS, SCTIMST. DLA tumor-bearing mice models were established by injecting a suspension of DLA cells (1×10^6 cells/100 µL PBS) intramuscularly into right leg of the mice. The theranostic properties of **PMNP** were executed about two weeks later when the tumor volume reached ~ 0.1-0.3 cm^3 in diameter.

For *in vivo* MRI imaging, DLA tumor bearing mice were divided into two groups, PBS and **PMNP** (10 mg/kg) and were injected (200 µL) through tail vein. Animal MRI studies were performed on a 7 T clinical magnet running a multisection T2-weighted turbo spin echo sequence (TR 5780 ms; TE 125 ms; FOV 98 mm × 140 mm; slice thickness 3 mm; flip angle 90). Signal intensity corresponding to pre- and post-contrast images was extracted and the percentage signal intensity change was calculated. Then, animals were euthanized, and tumor tissue and major organs such as brain, heart, liver, spleen and kidney were collected for understanding the biodistribution through SERS spectral intensity analysis.

When the tumor volume reached about ~ 0.1-0.3 cm^3, mice were divided into three groups for different therapeutic strategies. Group 1 was injected with PBS (control) whereas groups 2 and 3 were injected with **PMNP.** After 24 h post injection, groups 3 were irradiated with 808 nm laser (2 W/cm^2, 5 minutes). The materials (PBS, **PMNP**) were then injected intravenously on the second, fourth and sixth day following the first injection. Similarly, 808 nm laser ablation was executed after 24 h of each injection. The tumor volume measurement was then carried out for a course of 20 days to evaluate the therapeutic outcome of our nanoprobe. The

tumor volume (*V*) measurement was calculated as length×width^2×0.5, where length and width corresponds to the tumor diameters in the longest and widest point, respectively. Moreover, the body weights of mice were also monitored through the study. After the evaluation of whole therapeutic effects, all the animals were euthanized and tumors as well as major organs (brain, heart, kidney, liver, and spleen) were fixed with 4% formaldehyde to carry out H&E staining to analyze the potential toxicity of **PMNP**.

3.3. Design and fabrication of an ultrasensitive centrifugal force based lab-on-a-filter system for the size selective detection of circulating tumor cells

3.3.1. Materials and reagents

Graphite flakes, auric chloride ($HAuCl_4$), and trisodium citrate (TSC) were purchased from Sigma Aldrich. Anti-EpCAM and Anti-ErB2 antibodies were purchased from abcam. Track etched polycarbonate membranes were purchased from MERCK Millipore. All the chemicals were used as such without any further purification. We utilized an inverted fluorescence microscope (IX83; Olympus Corp., Tokyo, Japan) with a cooled CCD camera (XM10, monochrome, Olympus) for the *in vitro* fluorescence experiments and SERS experiments were performed on a WITec confocal Raman microscope with an integration time of 1s and 10 accumulations.

3.3.2. Preparation of Au-rGO@anti-ErbB2 SERS nanotag

The synthesis of the probe was initiated with the synthesis of Au-rGO which is described in section 3.1.2. The as-prepared Au-rGO was incubated with PEG-SH to provide high surface coverage and stability to the nanohybrid. After 3 h, free PEG molecules were removed by continuous rounds of washing and centrifugation (8000 rpm, 20 min) and the pellet was dispersed in PBS for antibody conjugation. The carboxyl groups of the PEGylated Au-rGO nanohybrids were activated by the addition of EDC (25 mM) and NHS (25 mM). After 30 min, excess reagents were removed by centrifugation (8000 rpm, 20 min) and the nanotags were resuspended in

PBS which was subsequently reacted with anti-ErbB2 antibodies for 2 h. After keeping the tags overnight at 4 ºC, the unbound antibodies were removed by 4 rounds of centrifugation (10,000 rpm, 5 min) to afford Au-rGO@anti-ErbB2 SERS nanotag.

3.3.3. Antibody immobilization over track etched polycarbonate membranes

Track etched polycarbonate membranes were incubated overnight at room temperature in a solution of anti-EpCAM antibody. To determine the effect of residual PBS salts, untreated polycarbonate membranes were also stored under the same condition in PBS. After incubation in the antibody or in PBS, all the polycarbonate samples were rinsed with fresh mQ-water and kept at 37 ºC for one week. This process allows us to store the membrane in room temperature for longer duration.

3.3.4. Cell spiking experiments

For conducting cell spiking experiments in PBS solution and blood samples, the cell suspension (1 mL, ~1 to 1000 cells/mL) was initially injected into the upper loading chamber of the centrifugal prototype. Then, the prototype was placed in a rotor and spun at a speed of 2400 rpm. During this process, cells were transferred to the filter membrane placed in the middle chamber and allowed the residual liquid to flow to the third and final collection chamber. After the filtration, two steps of PBS wash were carried out at a speed of 1200 rpm to remove the residual liquid, if any present in the filter membrane. The time required to separate 5 mL of sample was only 60 s, which is a considerably less time compared to earlier reported procedures.

3.3.5. CTC detection by SERS spectral analysis

After the filtration process, the lab-on-a-filter system was subjected to two steps of washing using PBS. During this step, the unbound nanotag and other blood components will be removed from the filter system. The filter was then removed from the filter chamber which was dissolved using chloroform and pelletized with the captured CTC. The pellet obtained from the filter was then illuminated by 633 nm laser and a SERS spectrum was recorded to evaluate the amount of Au-

rGO@anti-ErbB2 SERS nanotag. The SERS signal intensity corresponds to the number of CTCs present in the whole blood along with the WBCs.

3.3.6. CTC analysis by fluorescence microscopy

Fluorescence immunostaining technique was used for the analysis of captured cells. For the identification of captured cancer cell lines and CTCs, DAPI (100 ng/mL) positive, cytokeratin positive (240 ng/mL), and CD45 negative (4 μg/mL) were used. Prior to the staining process, cells were first blocked with 0.5 % BSA for 15 min at room temperature, followed by a washing step with PBS. The cells were then fixed with 4% paraformaldehyde for 15 min followed by a permeabilization step with 0.1% Triton X-100 for 5 minutes. The fixed cells were then washed with PBS. After the immunostaining process, the whole device was mounted on an inverted fluorescence microscope and images were recorded.

Chapter 4

Results and Discussion

Chapter 4

Results and Discussion

The development of multifunctional molecular diagnostic platforms for concordant visualization and treatment of diseases with high sensitivity and resolution has recently become a crucial strategy in cancer management. Thus, engineering functional metamaterials with high therapeutic and imaging capabilities to elucidate diseases from morphological behaviors to physiological mechanisms is an unmet need in the current scenario. In view of this, we have designed various plasmonic nanohybrids of graphene-gold composites for theranostic and biosensing applications. This chapter discusses the major results involved in the synthesis and detailed characterization of the three nanoprobes, their photo-physical studies, cell imaging capabilities and therapeutic abilities of the as-synthesized probes. The first section describes the key results associated with the studies on the development of a multifunctional theranostic probe built on graphene gold nanohybrid for bimodal imaging guided triple therapy. In the second section, the major findings generated from the fabrication of a plasmonic magnetic nanoprobe based on graphene, gold and SPIONS are discussed. The third section presents the major results from the development of a graphene gold hybrid platform for detection of circulating tumor cells.

4.1. Studies on development of multifunctional spiky gold nanostar decorated graphene nanohybrid as a targeted theranostic nanoprobe (TTNP) for bimodal imaging guided triple therapy

4.1.1. Synthesis of spiky gold nanostar decorated graphene nanohybrid (TTNP)

The preparation of the optical metamaterial, **TTNP** was initiated through the synthesis of graphene oxide by modified Hummers method. The UV visible spectra

showed a valley like absorption profile with a maxima around 260 nm (Figure 16a). The TEM and SEM images displayed the well-defined layered structure of GO as clear from figure 16b and 16c respectively. Then, in order to inherit the plasmonic properties, spiky gold nanostars were decorated over few layers of partially

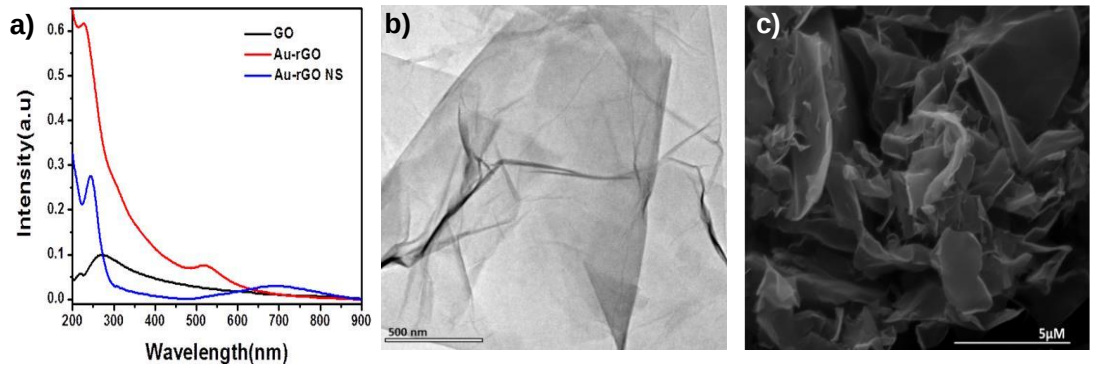

Figure 16. a) UV-Vis absorption spectra of GO, Au-rGO and Au-rGO NS, b) TEM and c) SEM images of GO.

reduced graphene oxide (Au-rGO NS) through the growth of spherical gold nanoseed developed over the rGO surface. The formation of seed as well as spiky star shaped gold nanoparticles over the graphene oxide was observed through morphological analysis (Figure 17). The as-formed plasmonic hybrid was then attached to a polymeric assembly (CS-PpIX-FA), which was built on chitosan (CS) tagged NIR emitting photosensitizer, protoporphyrin IX (PpIX), to activate intracellular "off/on" fluorescence imaging assisted photodynamic therapy (PDT).

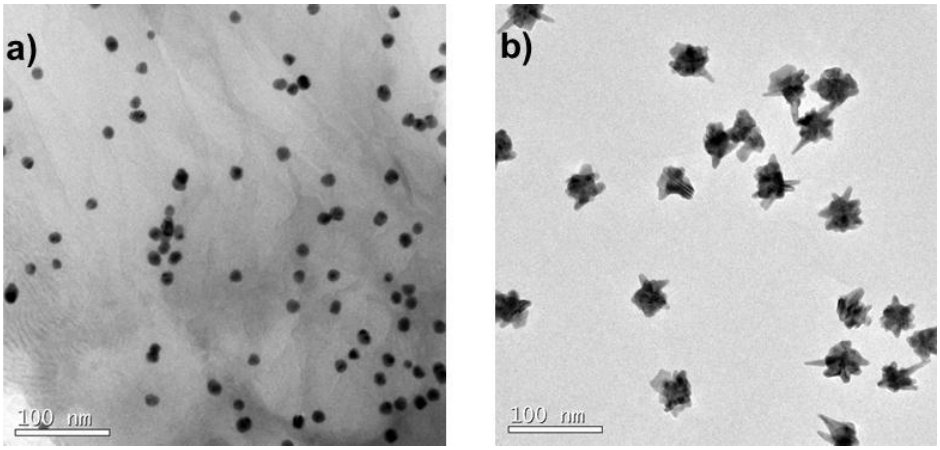

Figure 17. TEM images of a) Au-rGO and b) Au-rGO NS

On an average, 51 molecules of PpIX were attached to the CS chain through amide linkages. Then, folic acid was covalently conjugated with CS-PpIX. FTIR

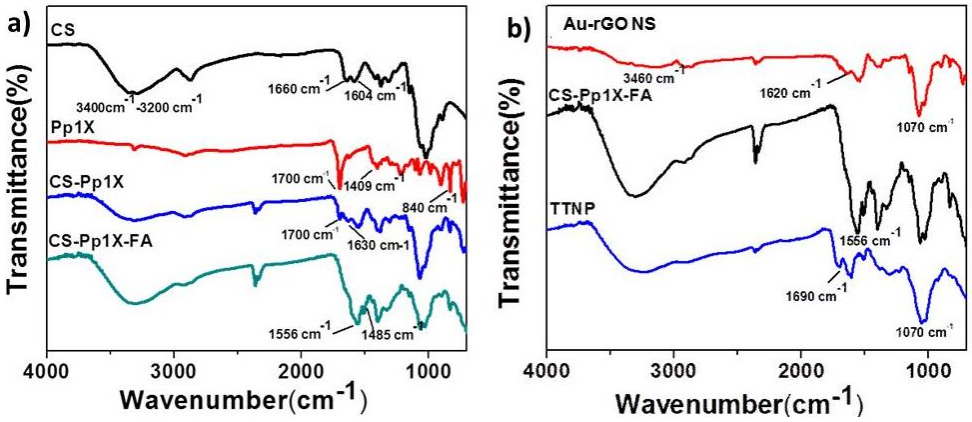

Figure 18. FTIR spectrum of a) CS, PpIX, CS-PpIX and CS-PpIX-FA b)Au-rGO NS, CS-PpIX-FA and **TTNP**.

analysis of CS-PpIX and CS-PpIX-FA displayed all the characteristic peaks of both CS and PpIX and showed a sharp decrease in the intensity of peak at 1700 cm^{-1}

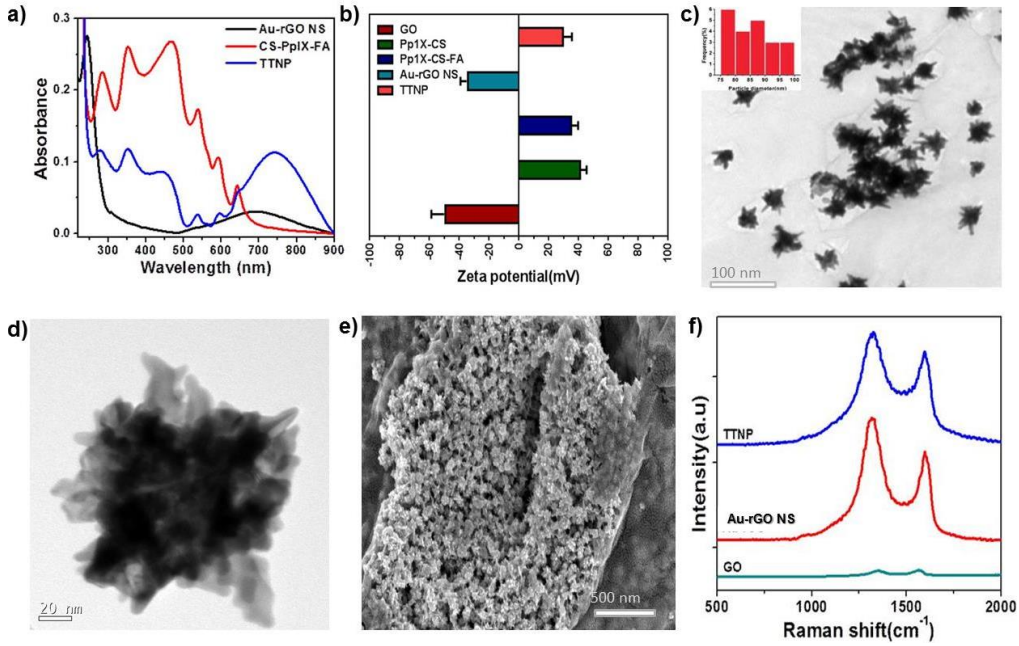

Figure 19. a) UV-Visible absorption spectra and b) zeta potential of various constructs, c) and d) represent the TEM image (inset showing the size distribution) and HR-TEM image of **TTNP** respectively. e) FE-SEM image of **TTNP** and f) SERS spectral data of GO, Au-rGO NS and **TTNP**.

which corresponds to the –COOH group of PpIX. In addition, it was also exhibiting a peak at 1630 cm^{-1} which corresponds to the amide bond formation between CS and PpIX. In CS-PpIX-FA, the peak which corresponds to the amide bond at 1630 cm^{-1} shifted to 1556 cm^{-1} due to the overlapping of various peaks of CS and PpIX present in the system (Figure 18a). CS-PpIX-FA was further appended with Au-rGO NS to fabricate our targeted theranostic nanoprobe, **TTNP**. UV-Vis absorption spectra of **TTNP** exhibited a strong plasmonic absorption in the NIR region, while retaining the characteristic Soret and Q bands of PpIX in CS-PpIX-FA (Figure 19a). Zeta potential measurements revealed a positive zeta potential with a magnitude of 29.5 mV (Figure 19b). The plasmonic nanoarchitectures present in **TTNP** (average size ~80 nm) were markedly visible from the TEM image and exhibited a spiky morphology with well-defined protrusions from its edges (Figure 19c and 19d). Moreover, these structures were found to be distributed uniformly over the few layers of graphitic surface (Figure 19e and 20). FTIR spectra of **TTNP** exhibited all the characteristic peaks of Au-rGO NS and CS-PpIX-FA. Especially, it showed characteristic C–O alkoxy stretching, C=C stretching, -OH stretching vibration of graphitic plane and –NH stretching bands of CS (Figure 18b). Furthermore, an increase in the height profiles up to 5 nm and an enhancement in the surface roughness of Au-rGO NS

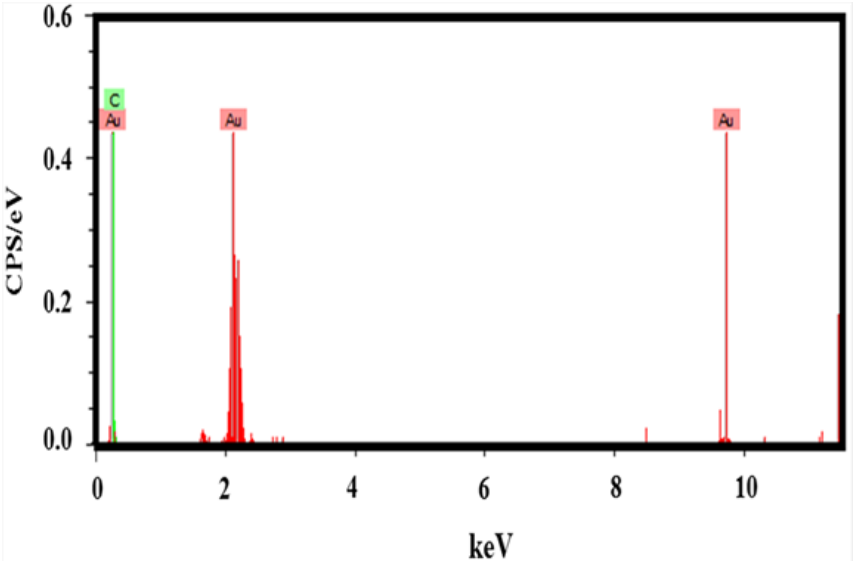

Figure 20. FE-SEM-EDX analysis of **TTNP**.

against GO confirms the adsorption of these nanostructures on the graphitic planes (Figure 21). This preferential adsorption of gold nanostructures at rGO vacancies led

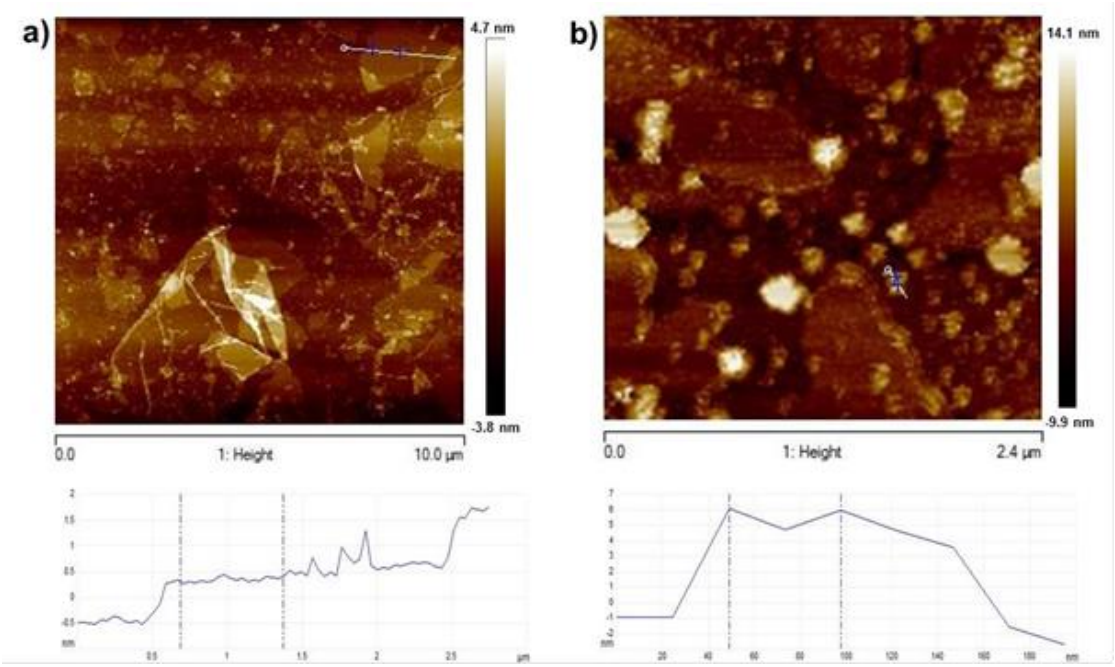

Figure 21. AFM analysis of a) GO and b) Au-rGO NS.

4.1.2. Evaluation of fluorescence activation and photosensitizing activity of TTNP

We studied the fluorescence properties of **TTNP** in the intracellular mimicking conditions. Initially, **TTNP** showed negligible emission at 630 nm (λ_{ex}= 405 nm) in

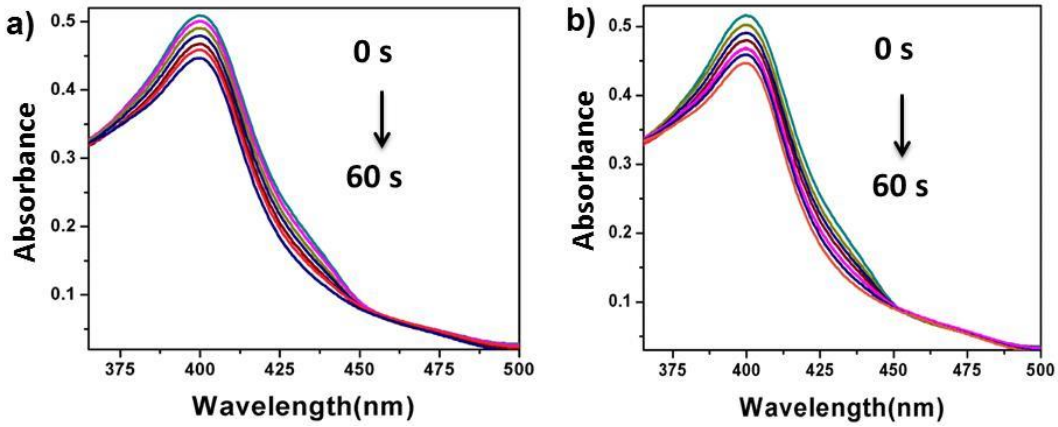

Figure 22. Decrease in absorption of DPBF in a) PpIX and b) **TTNP** under 532 nm laser irradiation (1 W/cm^2) for 60 seconds with 5 second intervals.

PBS. However, up on addition of sodium dodecyl sulphate (SDS, 5%) to the above solution, **TTNP** produced strong red emission at 630 nm (Figure 23a and 23b). In addition to the fluorescence activation, **TTNP** also showed 'off-on' photodynamic activity in the intracellular mimicking conditions. It was observed that generation of

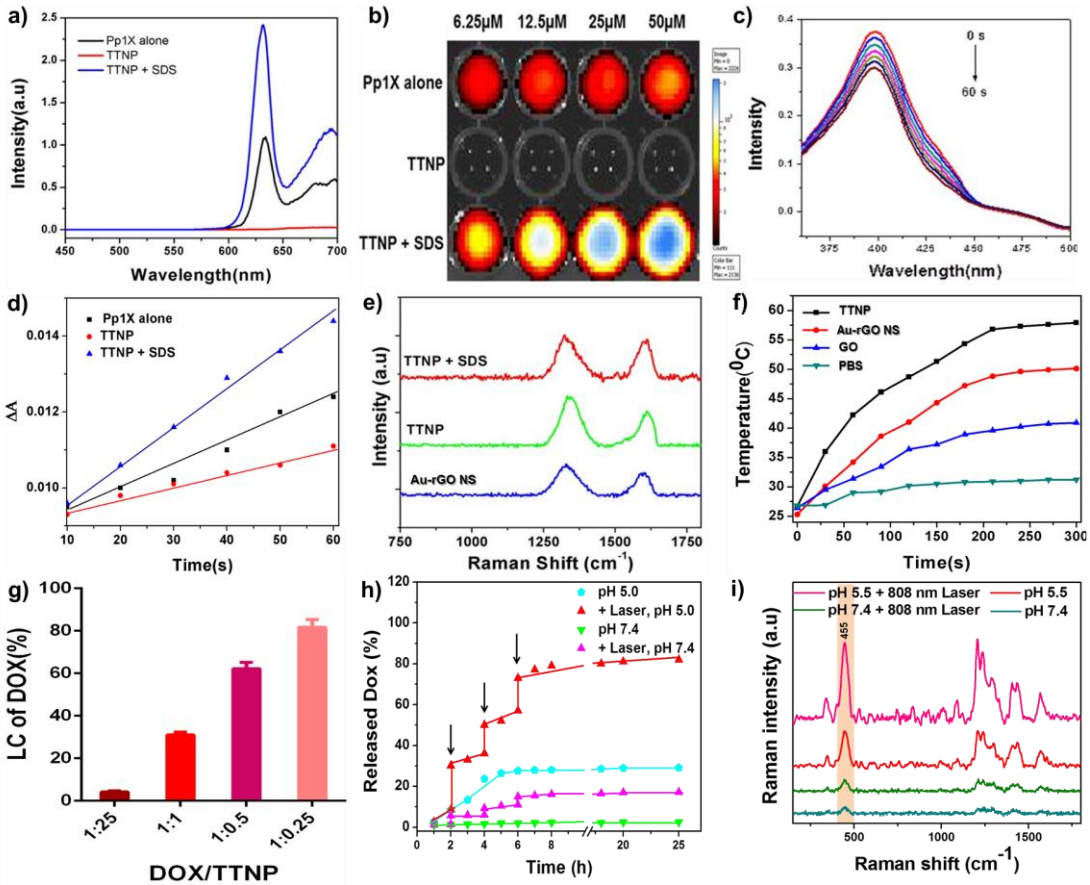

Figure 23. a) and b) shows the fluorescence enhancement of **TTNP** in the absence and presence of SDS. c) Time dependent decrease in DPBF absorption in methanolic solution of **TTNP** + SDS with 532 nm laser irradiation (1W/cm^2), d) Linear plot showing the variation of absorbance of different constructs with time, e) SERS spectral analysis of Au-rGO NS, **TTNP** and **TTNP**+SDS, f) Photothermal efficiency of various constructs under 808 nm laser with power density of 1 W/cm^2. g) Drug loading of DOX with **TTNP** in different ratios. Drug release of DOX from **TTNP** under different pH and 808 nm laser irradiation (1 W/cm^2, 60 s) through UV-Vis absorption (h) and SERS spectral analysis (i). Black arrow indicates the point of laser irradiation.

ROS by **TTNP** after laser irradiation was low with a singlet oxygen quantum yield of 0.52 (Figure 22b and 23d) but upon the addition of SDS, the singlet oxygen quantum yield of **TTNP** steeply raised to 0.68 (Figure 23c and 23d) higher than that of PpIX alone having a quantum yield efficiency of 0.63 (Figure 22a and 23d).

4.1.3. SERS imaging capabilities and photothermal properties of TTNP

We then investigated the SERS properties of **TTNP** by the addition of SDS which showed the retention of its characteristic D and G bands as shown in figure 23e. So, **TTNP** can furnish both fluorescence and SERS, which is much difficult to achieve simultaneously without interference from each other. Thus, we could successfully visualize real-time rapid internalization of **TTNP** through dual imaging channels without compromising one another. Along with that, we utilized the strong plasmon induced photoabsorption of **TTNP** in the NIR region to trigger its innate PTT efficacy.

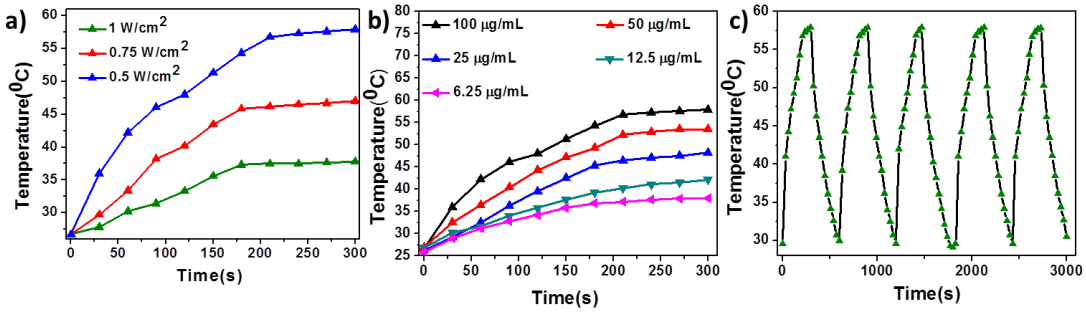

Figure 24. Photothermal properties of **TTNP** under a) various power densities and b) various concentrations. c) represents the photothermal stability evaluation of **TTNP** over a period of five cycles.

To demonstrate the photothermal ablation, we irradiated various constructs (**TTNP**, Au-rGO NS, GO, PBS) with 808 nm laser for 5 minutes wherein **TTNP** showed rapid rise of temperature (57.2 ºC) against GO (40.2 ºC) and Au-rGO NS (49.7 ºC) (Figure 23f). We also evaluated the PTT ability of the construct with different concentrations (6.25 µg/mL to 100 µg/mL) of **TTNP** and with varying laser power densities (0.5 W/cm^2 to 1 W/cm^2) as displayed in Figure 24a and 24b respectively. Moreover, the photothermal ability of **TTNP** was found to be consistent

over 5 cycles without any noticeable loss in the heating potential as evident from figure 24c.

4.1.4. Investigation of drug loading potential and stimuli responsive drug release

Owing to the presence of high polyaromatic surface area, graphene planes in **TTNP** was utilized as a cargo for carrying DOX through weak π-π and hydrophobic interactions. The successful loading of various concentrations of DOX in the **TTNP** (**TTNP-DOX**) surface was evaluated by monitoring the quenching of its characteristic emission peak located at 590 nm (Figure 25).

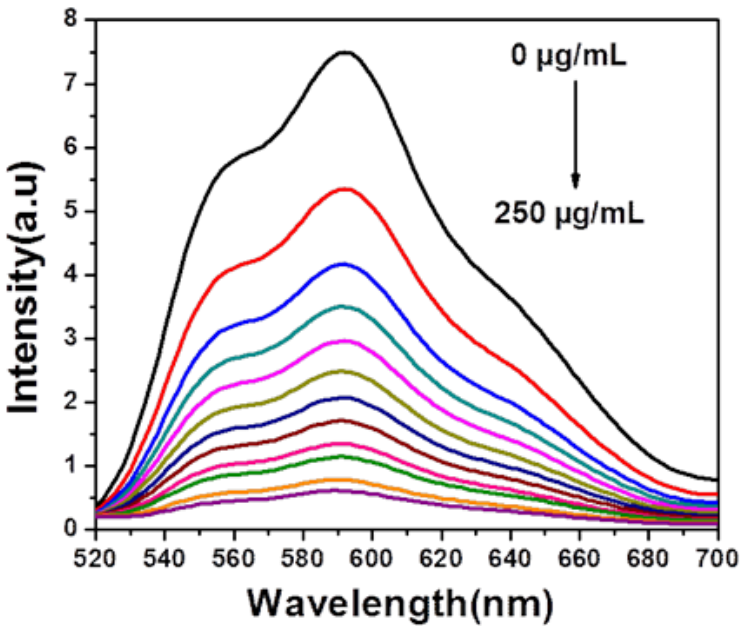

Figure 25. Fluorescence quenching of DOX on additon of various concentration of **TTNP**.

Along with high drug loading efficiency of **TTNP** (Figure 23g and 26), for an effective chemotherapy, it is always clinically advisable to have a temporal and sustained drug release prompted by multiple external stimuli like pH, heat, redox potential etc. So, we utilized the photothermal efficacy of **TTNP** to trigger the drug release of DOX at 37 ºC from the **TTNP-DOX** with laser irradiation (2 min, 0.75 W/cm^2). The results indicated that **TTNP** exhibited enhanced laser induced drug release which got boosted in 2 hours from 10% to 30% following 2 min laser irradiation. Similarly, enhanced drug release was also observed when laser was

triggered at 4 hours and 6 hours, when the release got increased from 37% to 45% and from 55% to 73%, respectively (Figure 23h). Finally, 80% DOX was released after 24 hours, which was about 4 times higher than **TTNP** without laser irradiation. During each stage of dual stimuli (pH and light) release process, the fluorescence intensity of DOX went on increasing with a corresponding decrease in the SERS signal of DOX centered at 455cm^{-1} (Figure 23i).

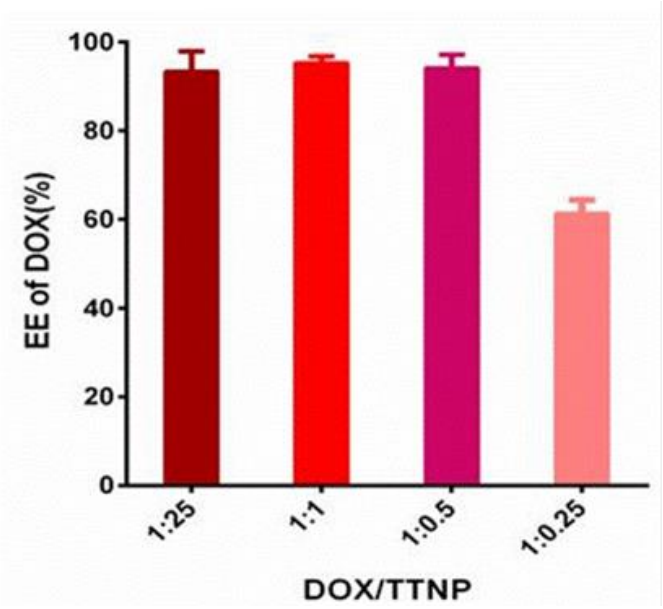

Figure 26. Encapsulation efficiency of DOX in various ratios with **TTNP**.

4.1.5. *In vitro* cellular uptake and fluorescence activation in MDAMB-231 cells

Before performing detailed cell studies, we investigated the intrinsic cytotoxicity of **TTNP** in MDAMB-231 breast cancer cell lines, as its biological application stands on its commendable cellular viability. In this context, various concentrations of **TTNP** (6.25-200 µg/mL) were exposed to MDAMB-231 cell lines for 24 hours and its cytotoxic effects were determined using MTT assay (Figure 27). After that, we monitored the characteristic cellular uptake of **TTNP** (5µg/mL of free PpIX) from 0 to 120 minutes.

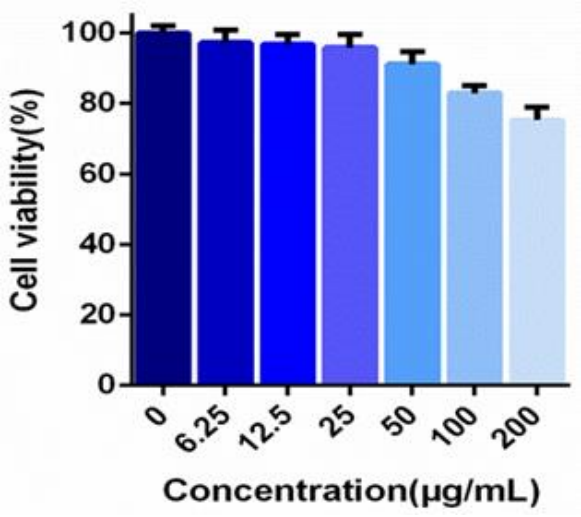

Figure 27. Cytotoxicity evaluation of various concentration of **TTNP** through MTT asssay.

Initially, it produced very weak fluorescence intensity as evident from figure 28a. But, as the incubation time goes on, fluorescence intensity of **TTNP** enhanced tremendously, indicating the restoration of the fluorescence "on" state of porphyrin moiety, similar to the fluorescence recovery observed in the presence of SDS. This

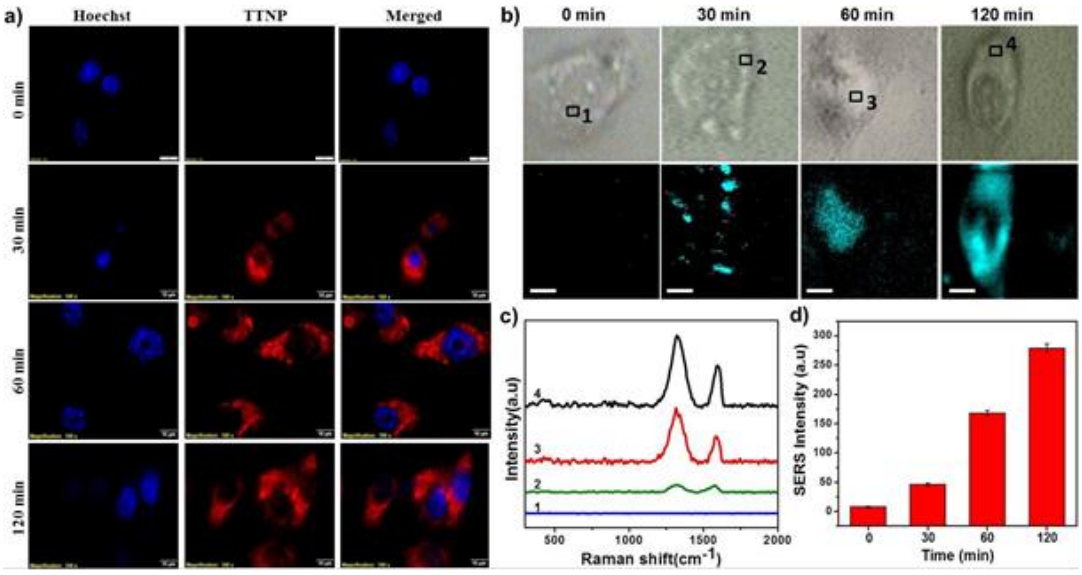

Figure 28. *In vitro* cellular uptake of **TTNP**. Time dependent a) fluorescence and b) SERS imaging of **TTNP** in MDAMB-231 cells. c) SERS spectra acquired from the specified points shown in b). d) Bar diagram showing the variation of SERS spectral intensity with time.

indeed, prompted us to evaluate the label-free cellular internalization of **TTNP** through SERS signals of Au-rGO NS. Both D and G band of Au-rGO NS were utilized for monitoring the time dependent cellular internalization which showed rapid internalization within 30 minutes (Figure 28b-d). Moreover, the coherence between both fluorescence and SERS data gives a strong indication that porphyrin moiety remains (CS-PpIX-FA) in contact with graphene surface even after the polymer disassembly. This in turn, provide room for accommodating the PDT efficacy of CS-PpIX-FA with the inherent photothermal ablation and photo induced chemotherapy of Au-rGO NS to perform triple modal therapeutic strategy for ensuring complete cell death.

4.1.6. Evaluation of therapeutic outcome of DOX loaded TTNP *in vitro*

The singlet oxygen generation efficiency of **TTNP** was evaluated in MDAMB-231 cells using a non-fluorescent dye, 2′, 7′-dichlorofluorescein diacetate (DCFH-DA), which will turn into green fluorescent DCF upon reaction with ROS. Cells incubated with various constructs were subjected to laser irradiation (1W/cm^2, 532 nm) for 60 seconds in order to trigger the production of singlet oxygen. The results showed that **TTNP** produced remarkably higher level of singlet oxygen, about two fold higher than that produced by free PpIX (Figure 29a and 29b). On the contrary, **TTNP** showed negligible fluorescence in the absence of laser as compared to PpIX alone, indicating its ability to produce laser specific toxicity to the cancer cells. Subsequently, we also evaluated the photothermal properties of **TTNP,** through live/dead assay after exposure to 808 nm laser (1W/ cm^2) for 60 seconds. As compared to the control group, **TTNP** caused severe cell death along with laser irradiation (Figure 29c (i-iv)). On the other hand, **TTNP** without irradiation caused negligible toxicity to the cells. In addition to that, after the successful internalization of **TTNP-DOX** through receptor mediated endocytosis, the dual stimuli intracellular response and therapeutic action of doxorubicin loaded in the nanoconstruct was also monitored. Initially, DOX gets detached from **TTNP-DOX** and releases in to the cytoplasmic compartments of cancer cells due to the acidic pH prevailing therein and later moves to the nucleus to induce apoptosis (Figure 30).

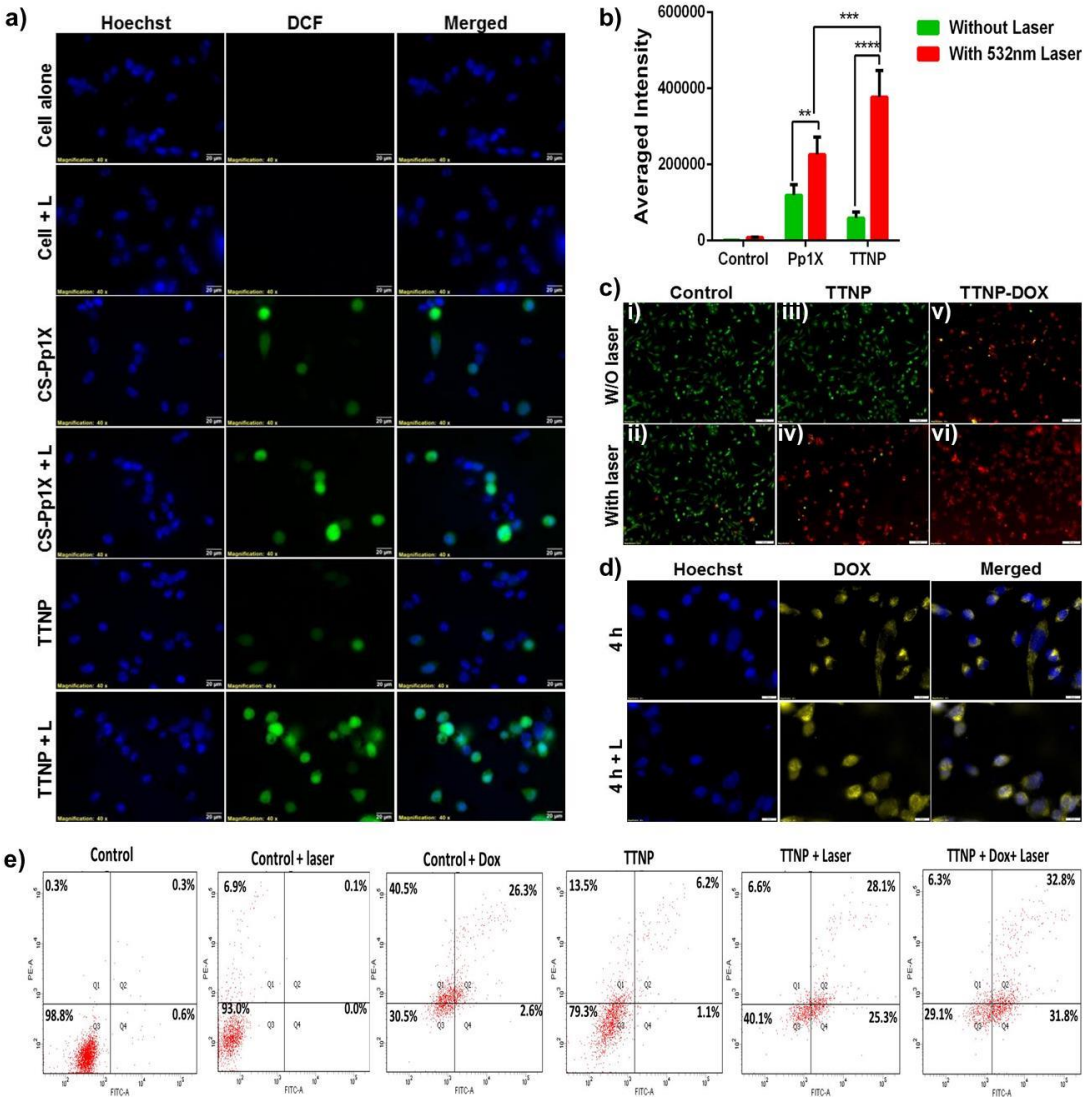

Figure 29. *In vitro* therapeutic evaluation of **TTNP** in MDAMB-231 cells. a) Fluorescence microscopic images and b) fluorescence intensity profiling of various constructs in the absence and presence of laser (532 nm) through DCFDA analysis. c) Live-dead assay of **TTNP** and **TTNP-DOX** in the absence and presence of laser (808 nm). d) Fluorescence microscopic images of DOX release from the construct in the absence and presence of laser (808 nm). e) Evaluation of therapeutic efficacy of **TTNP** and DOX with or without laser irradiation through flow cytometry assay.

In sequence, light responsive DOX release from the probe was also examined after four hours of incubation in MDAMB-231 cells (Figure 29d). After photothermal ablation (1W/cm^2, 60 seconds), the major Raman fingerprinting peaks

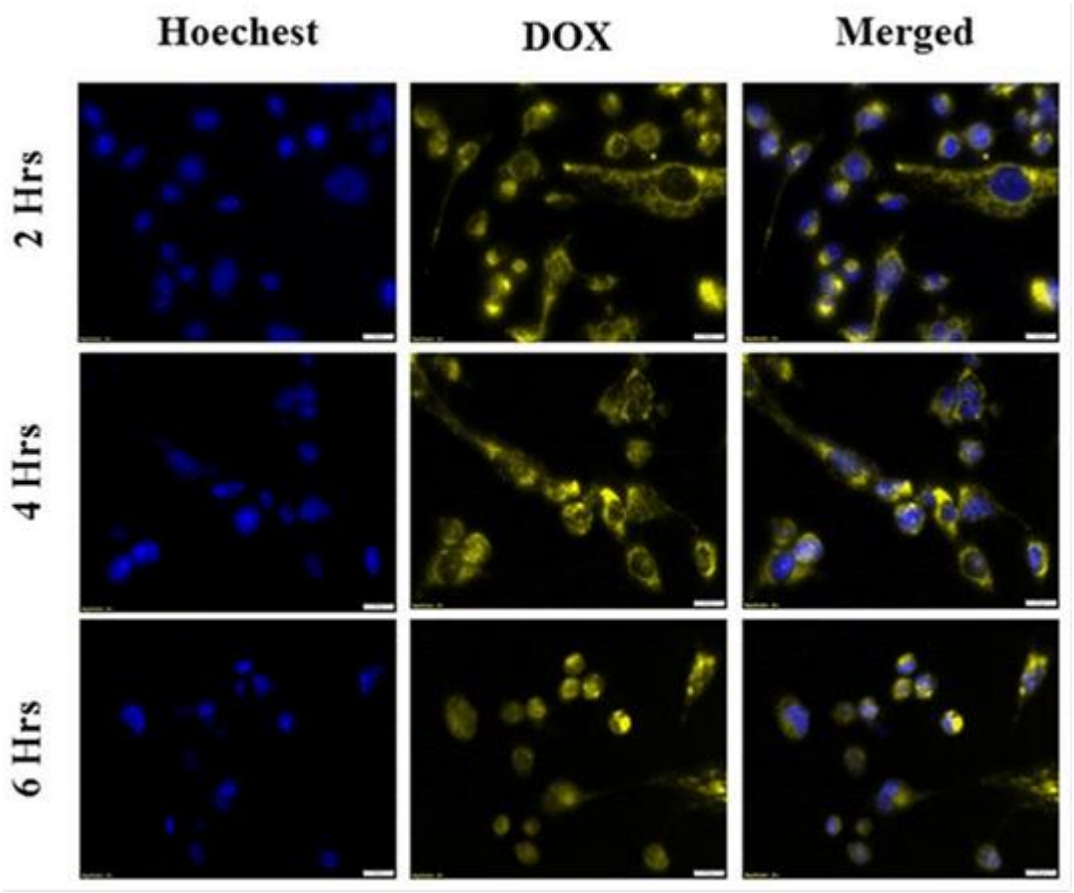

Figure 30. Time dependent pH responsive cellular release of DOX.

of DOX got diminished in the cytoplasmic areas due to the detachment of more DOX molecules from the graphitic planes (Figure 31). On the other hand, the fluorescence signal intensity of DOX present in the lysosome was rapidly shifted to nucleus and induced more cytotoxic effects in addition to the pH triggered chemotherapy (Figure

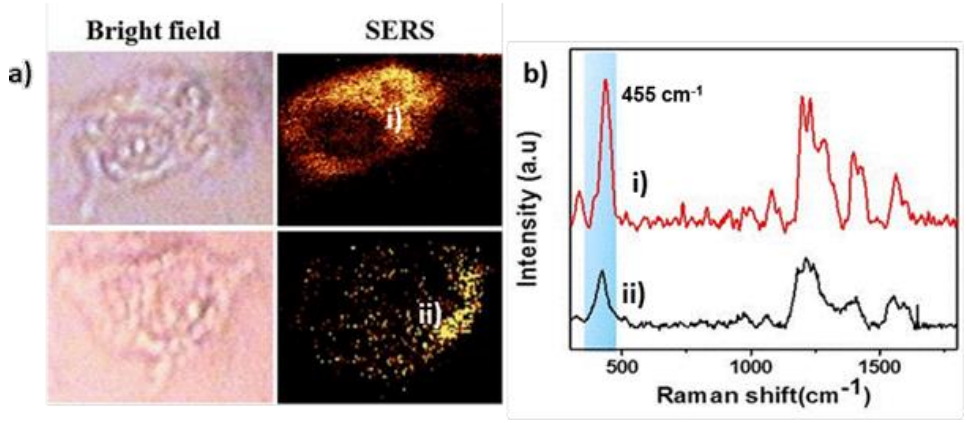

Figure 31. a) SERS mapping and b) corresponding spectra showing the DOX release from **TTNP** i) without and ii) with 808 nm laser (1W/cm^2, 60 s).

29d), which was examined through live/dead assay (Figure 29c (v and vi). The synergistic effect and total outcome of the combined therapeutic strategy (PDT, PTT and PTT induced chemotherapy) was estimated initially through MTT assay (Figure 32). The cell viability after the combined action was dramatically dropped to ~15%, which is significantly higher than the effects induced by the individual therapeutic modalities. Then, the cell death execution of various light sensitized therapeutic properties of our probe with lasers (808 nm + 532 nm) was investigated in detail through flow cytometry (Figure 29e). It is noteworthy that, laser triggered therapeutic efficacies of **TTNP** (64.6%) was three times higher than the conventional DOX (28.9%) induced apoptosis under *in vitro* conditions.

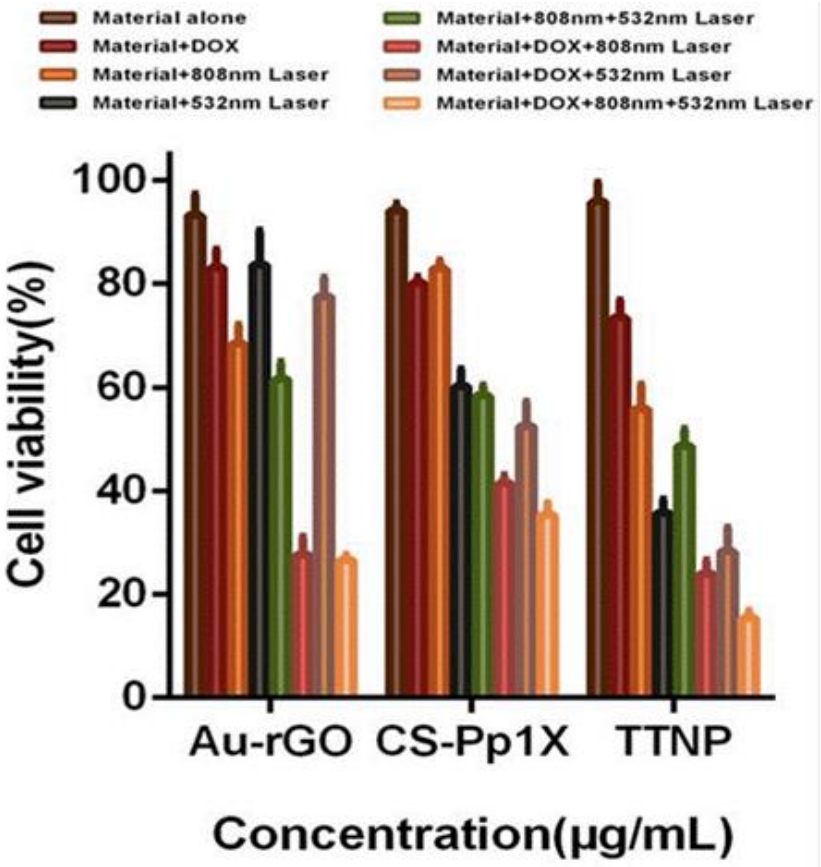

Figure 32. Therapeutic evaluation through MTT assay of MDA MB 231 cells after various treatments.

4.1.7. *In vivo* imaging and biodistribution of TTNP

Inspired by the promising attributes of **TTNP** in the *in vitro* conditions, we moved on to evaluate its *in vivo* targeted theranostic ability by intravenous injection into DLA

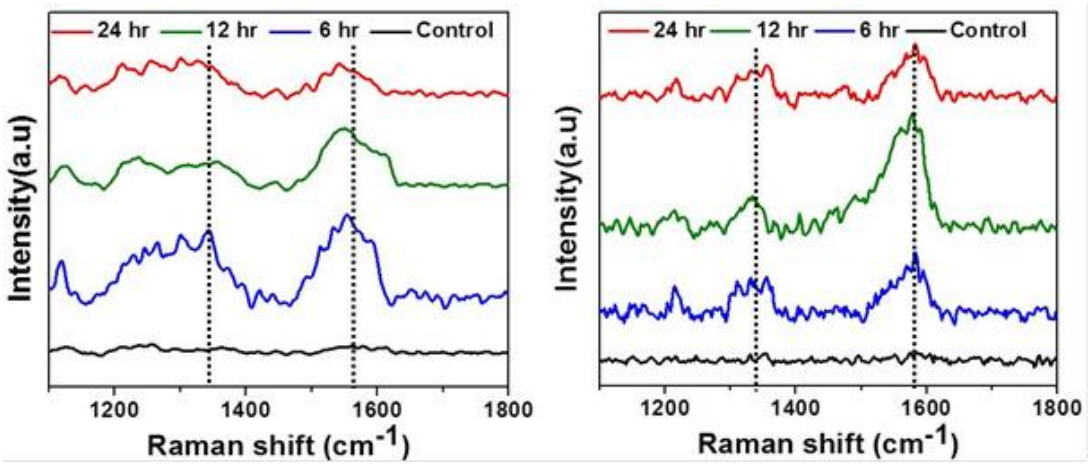

Figure 33. SERS analysis of blood (left) and urine (right) samples collected at different time periods after intravenous injection of **TTNP-DOX**.

tumor bearing mouse models. In order to utilize the potential of **TTNP** as a nanoplatform for *in vivo* imaging, it is extremely important to initiate the investigation through its pharmacokinetics and biodistribution. The circulation of **TTNP** in the blood stream was evaluated through SERS spectral analysis of blood samples which showed a time dependent decline in the spectral intensity of Raman signals at 1580 cm^{-1} and 1340 cm^{-1} from 6 h to 24 h (Figure 33). At the same time, spectral analysis of urine samples exhibited time dependent increase of the same indicating the preferential excretion of the material from the body (Figure 33).

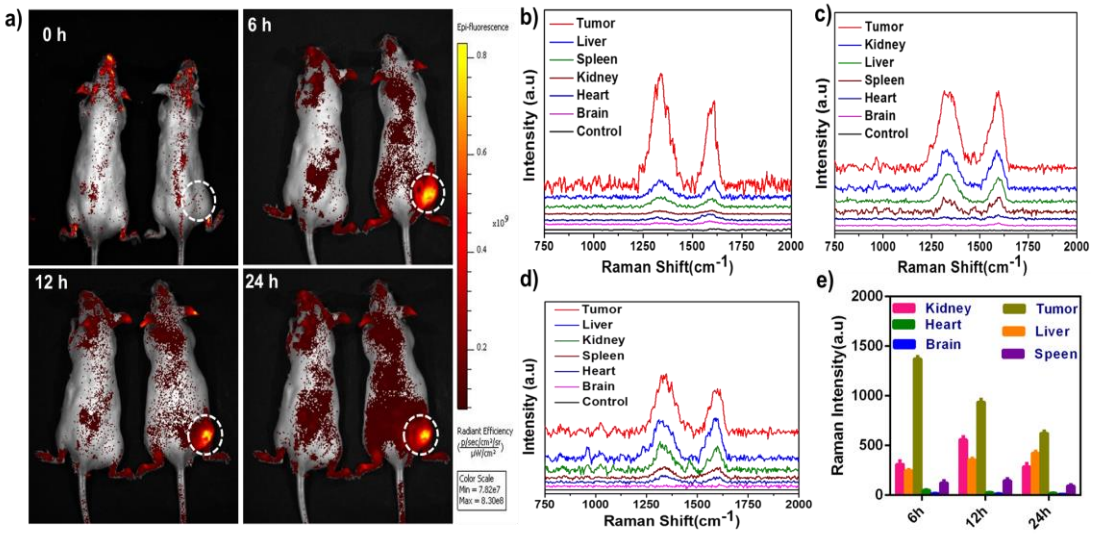

Figure 34. a) *In vivo* fluorescence images of DLA tumor bearing mice at different time points. Inset circles represent the tumor site. *Ex vivo* SERS spectral analysis of

various organs treated with **TTNP** at 6 h (b), 12 h (c) and 24 h (d). e) Bar diagram showing the SERS spectral intensity of the organs at the specified time points.

The intrinsic architecture-dependent fluorescence and SERS property has allowed **TTNP** to be used as a turn-on optical nanoprobe to enhance the sensitivity of NIR imaging for efficient cancer diagnosis through signal amplification and preferential accumulation at the tumour site. From Figure 34a , it is clear that **TTNP** displayed significantly higher tumor accumulation at 6 h post injection and found to retain its fluorescence even after 24 h, due to its improved stability in the circulation

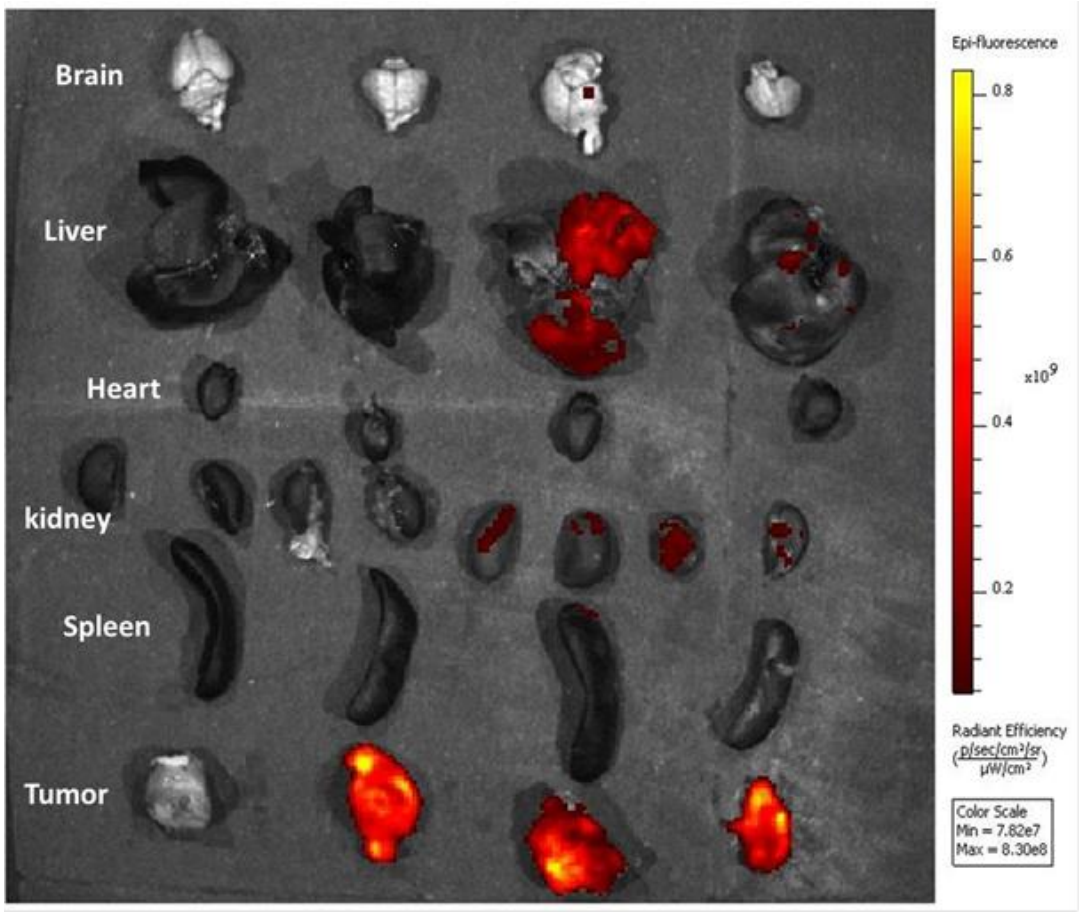

Figure 35. *Ex vivo* fluorescence imaging of various organs (brain, liver, heart,kidney, spleen and tumor) at 0, 6,12 and 24 hours (from left to right).

system and higher uptake into the indigenous tumor sites. Moreover, favorable biodistribution pattern was observed in tumor, which showcased superior fluorescence intensity in *ex vivo* imaging (Figure 35) and characteristic Raman signature peaks (at 1580 cm^{-1} and 1340 cm^{-1}) of **TTNP** at 6 h while retaining

sufficient intensity at 24 h (Figure 34b-e). In addition, various organs like brain, heart, liver, kidney and spleen were subjected to *ex vivo* fluorescence and SERS analysis to determine the distribution of material at various time points (Figure 35 and Figure 34b-e). It is important to note that, heart and brain showed minimal accumulation while other organs displayed a time dependent reduction in their accumulation profiles.

4.1.8. *In vivo* evaluation of synergistic therapeutic efficacy of TTNP

In order to investigate the synergistic therapeutic efficacy of **TTNP** enabled simultaneous PTT, PDT and chemo-PTT effects *in vivo*, DLA tumor-bearing mice were randomly divided into 7 groups (n=3) *viz.* saline as control, **TTNP** alone, **TTNP** with 808 nm laser, **TTNP** with 532 nm laser, **TTNP-DOX** alone, **TTNP-DOX** with 808 nm laser and **TTNP-DOX** with combined 808 and 532 nm laser. Owing to the selective accumulation of **TTNP** in tumor sites after 6 h, 532 nm and 808 nm laser irradiation was carried out successively at tumor sites (1 W/cm^2) for 60 seconds. At the same time, tumor volume and body weight of various groups were

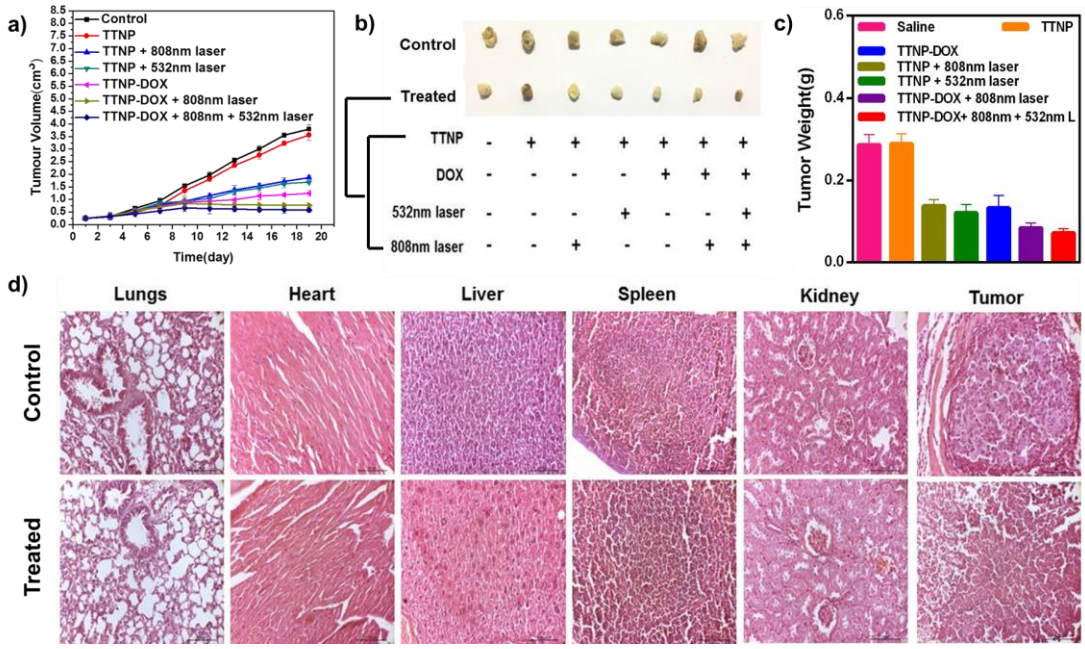

Figure 36. *In vivo* analysis of therapeutic potential of **TTNP**. a) Tumor volume reduction analysis after various therapeutic strategies. b) Photographs showing the reduction in tumor size after various therapeutic actions. c) Tumor weight evaluation

of excised tumors after various treatments. d) H&E examination of various organs before and after treatment with **TTNP-DOX**.

monitored daily and plotted as a function of time to assess the individual as well as the coupled therapeutic effects over a period of 3 weeks. After various therapeutic strategies, tumor volumes calculated from single laser (808 nm) as well as coupled laser (808 nm+532 nm) irradiated **TTNP-DOX** injected mice were found to show a remarkable reduction after 8 days as compared to the group injected with saline and **TTNP-DOX** alone (Figure 36a). On the other hand, tumor volume of mice groups injected with **TTNP** alone and **TTNP** with either 808 or 532 nm laser increased exponentially over the course of time. Furthermore, no significant body weight reduction was observed in various groups indicating the low toxicity effects during the *in vivo* experiments (Figure 37).

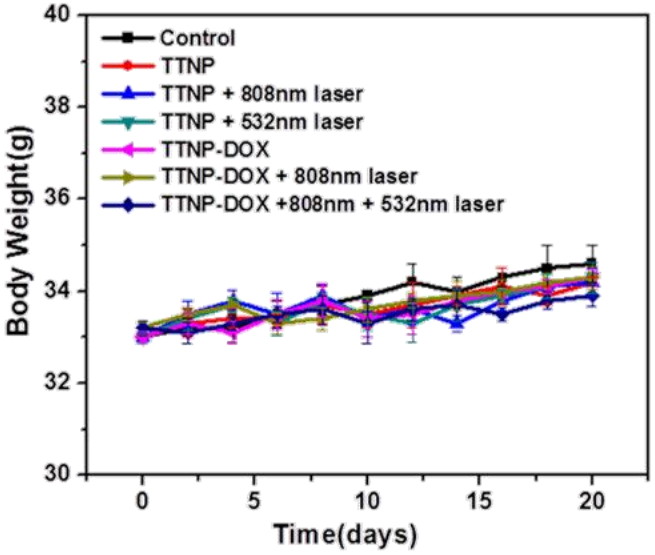

Figure 37. Body weight analysis of mice after various therapeutic actions.

After 20 days, all the mice were euthanized and the tumor tissue were snipped out and weighed. The effective therapeutic outcome of the entire experiment was evident through the observed reduction in the tumor size (Figure 36b) and the corresponding mean tumor weights (Figure 36c). It is noteworthy that, H&E (hematoxylin and eosin) evaluation of tumor tissues of laser treated **TTNP-DOX** injected mice showed severe cancer necrosis (~70%) (Figure 38) when compared against the control groups. Moreover, no significant damage to other major organs

was observed, indicating the safety of **TTNP-DOX** as a theranostic carrier under *in vivo* conditions (Figure 36d).

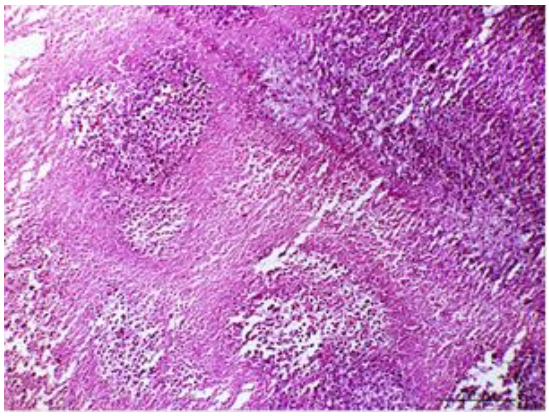

Figure 38. H&E analysis of tumor after various therapeutic actions.

4.2. Synthesis of graphene-gold nanohybrids as plasmonic magnetic nanoprobe (PMNP) for dual modal imaging assisted CDT/PTT

4.2.1. Synthesis and characterization of PMNP

In order to prompt the clinical application of CDT/PTT in cancer therapeutics, our efforts to the construction of plasmonic magnetic nanoprobe (**PMNP**) comprises of the development of multifunctional gold-graphene plasmonic architecture (Au-rGO) conjugated super paramagnetic iron oxide nanoparticles (SPIONS). The fabrication of magnetically intercalated optical metamaterial, **PMNP** was initiated through the synthesis of graphene oxide by modified Hummers method. Then, spherical gold nanoseeds having diameter ~ 15 nm were decorated over few layers of graphene oxide (Au-rGO) to inherent the optical and plasmonic properties of the nanohybrid. The surface of as-formed plasmonic hybrid was modified with 4-aminothiophenol

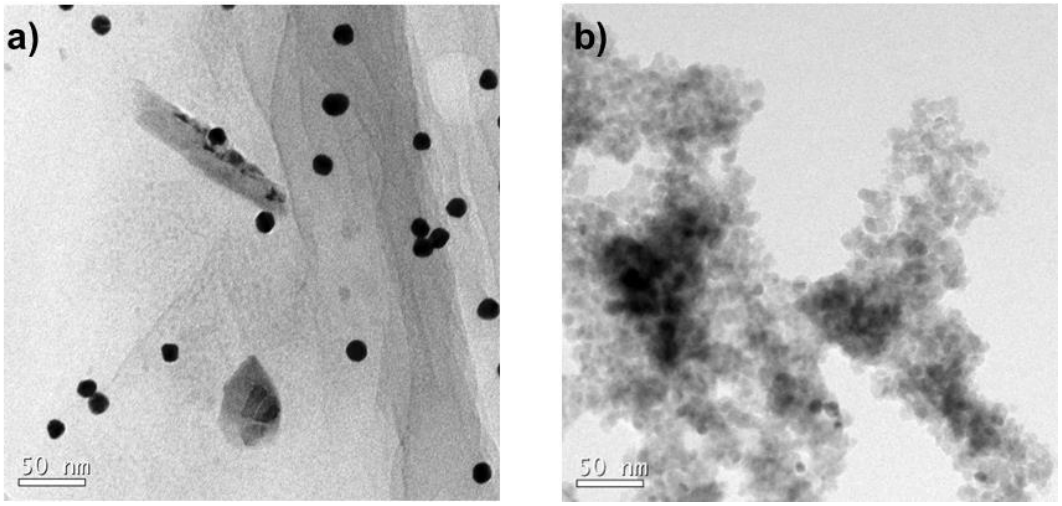

Figure 39. TEM images of a) Au-rGO and b) SPIONS.

(4-ATP), a prominent SERS reporter and then amine terminated plasmonic hybrid (Au-rGO-ATP) was conjugated to the citrate stabilized SPIONS through EDC/NHS coupling, to complete the fabrication of our probe **PMNP**, to afford its dual imaging assisted dual therapy. The TEM images of Au-rGO and SPIONS are given in Figure 39a and 39b respectively. The particle size and morphology of plasmonic gold nanoseed and SPIONS present in **PMNP** were distinctly visible from its TEM

images and EDS elemental mapping exhibiting the homogeneous dissemination of Au, Fe and O over the graphitic layers (Figure 40) further conforming its chemical composition. During the adsorption of ATP over Au-rGO, FTIR spectra showed all

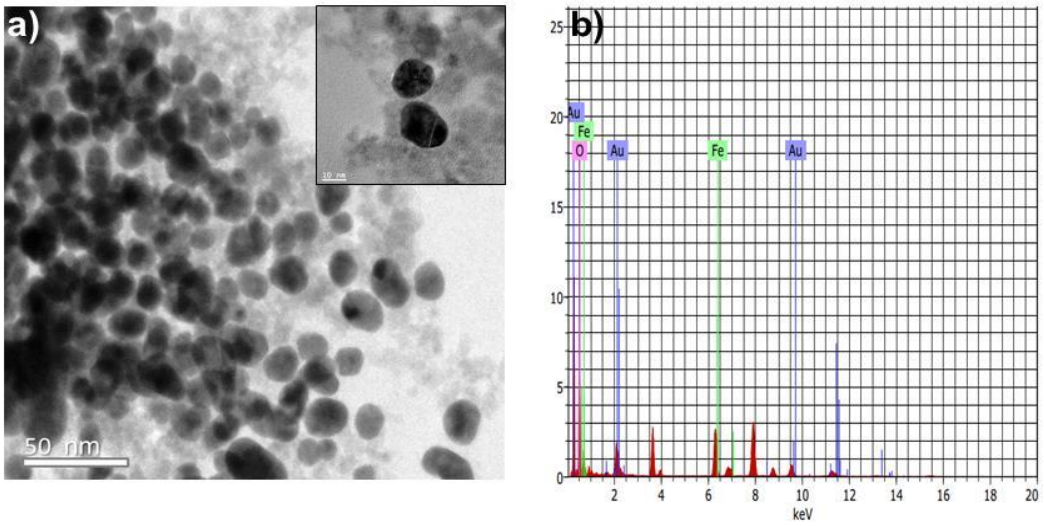

Figure 40. a) TEM image (Inset represents HR-TEM image of **PMNP**) and b) EDX elemental mapping of **PMNP**.

the characteristic peaks of Au-rGO and ATP (1080 cm^{-1},1620 cm^{-1}, 3228 cm^{-1}, 3358 cm^{-1}) except the one that corresponds to the thiol group present in ATP (2549 cm^{-1}) which further conforms the formation of Au-S bond in Au-rGO-ATP (Figure 41a).

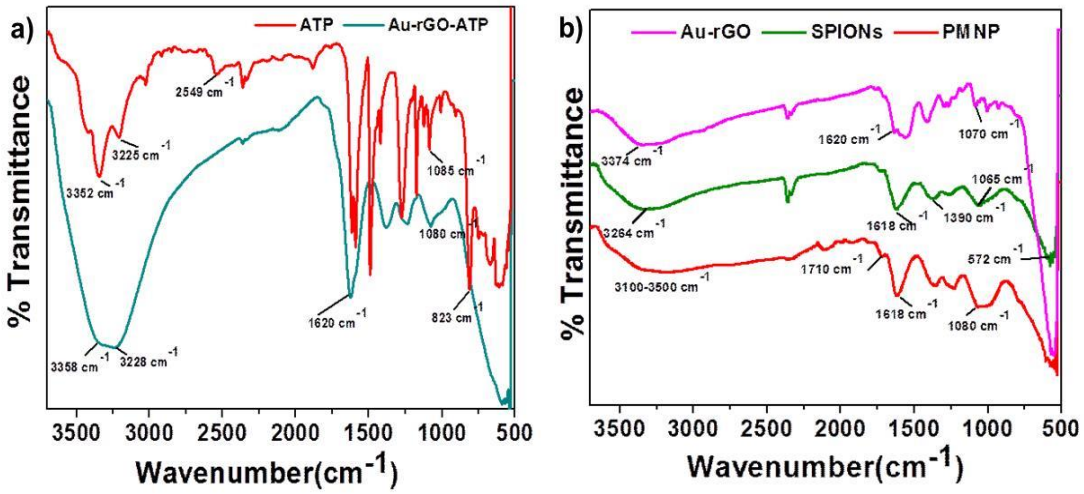

Figure 41. FTIR spectra of a) ATP, Au-rGO-ATP and b) Au-rGO, SPIONS, **PMNP**.

Further, amide bond coupling between SPIONS and Au-rGO-ATP to form **PMNP** was indicated by the peaks at 1710 cm^{-1} and those between 3500-3200 cm^{-1} which corresponds to the -CO and -NH stretching respectively (Figure 41b). Moreover,

PMNP exhibits all the sharp and pronounced characteristic Raman signals of Au-rGO and ATP at 1330, 1590, 1177, 1090, and 473 cm^{-1} owing to its synchronized SERS effect (Figure 42a). The absorption spectra of **PMNP** exhibited the near-infrared (NIR) and plasmonic absorption of Au-rGO, while retaining the characteristic absorption of SPIONS ranging from 250 to 350 nm (Figure 42b). The absorption valley of **PMNP** spans the NIR region, which propel them to be receptive to light in the biological window. Therefore, 808 nm laser can be employed to understand the photoenhanced CDT/PTT performances of **PMNP**.

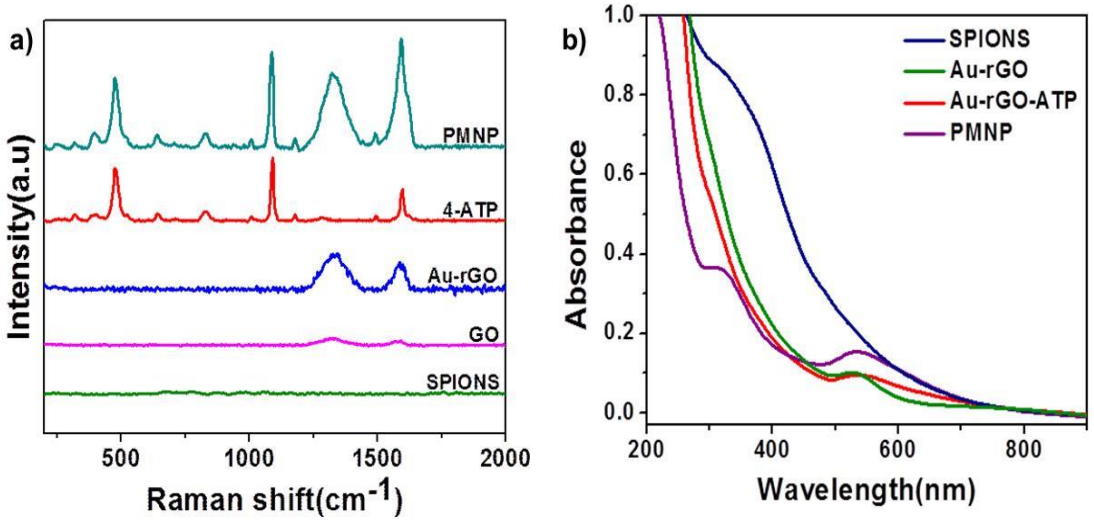

Figure 42. a) SERS and b) UV-Visible absorption spectral analysis of various constructs used in the construction of **PMNP**.

4.2.2. Investigation of magnetic properties of PMNP

The magnetic efficacies of **PMNP** were evaluated by the field-dependent magnetization measurement at room temperature (Figure 43a), which was also verified through magnetic separation (Figure 43b). **PMNP** exhibited a hysteresis in the S-shape curve similar to the SPIONS, indicating its super paramagnetic nature. But owing to the inductive effect offered by Au and C present in the **PMNP**, it has less saturated magnetization as compared to SPIONS. Further, the MR imaging properties of **PMNP** was explored by monitoring its transverse relaxation time (T2) and compared it with SPIONS using an applied magnetic field of 1.5 T (Figure 44). As the Fe concentration increases, both the materials were capable of causing a decrease in the signal intensity in their T2 MR images (Figure 44a). The transverse

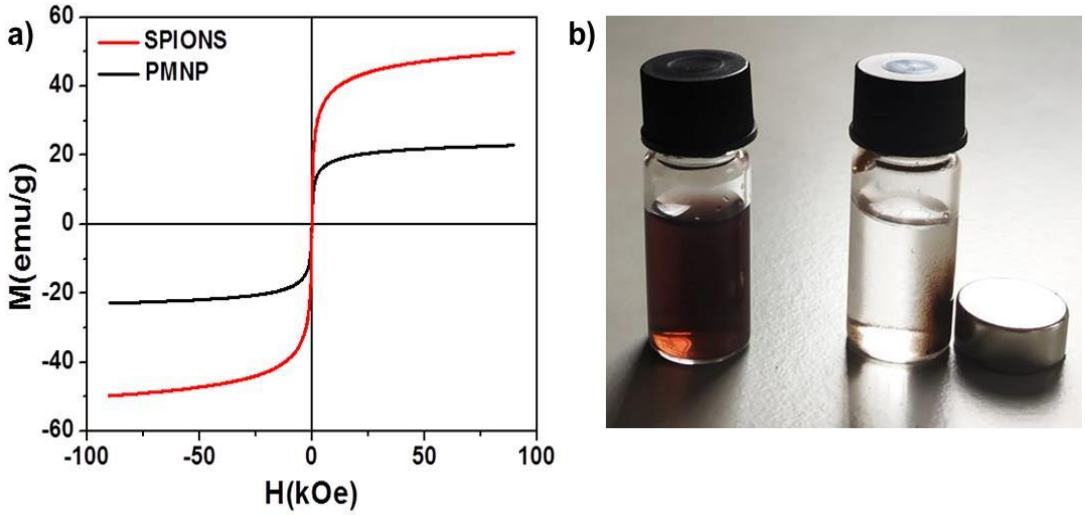

Figure 43. a) VSM measurement comparison between SPIONS and **PMNP**. b) Photograph showing the magnetization property of **PMNP** in presence of an external magnet.

r_2 relaxivity values of SPIONS and **PMNP** were calculated to be 139.45 and 150.07 $mM^{-1}s^{-1}$, respectively (Figure 44b). The lower r_2 value of **PMNP** as compared to SPIONS may be due to the inductive effect of C and Au over Fe present in **PMNP**. But the fact is that **PMNP** has similar or better r_2 relaxivity values than most of the Fe based clinically proved MRI contrast agents (ferumoxsil (72 $mM^{-1}s^{-1}$, ferumoxide (98.3 mM^{-1} S^{-1}) . Thus, **PMNP** provides an avenue for better T_2 MR imaging applications.

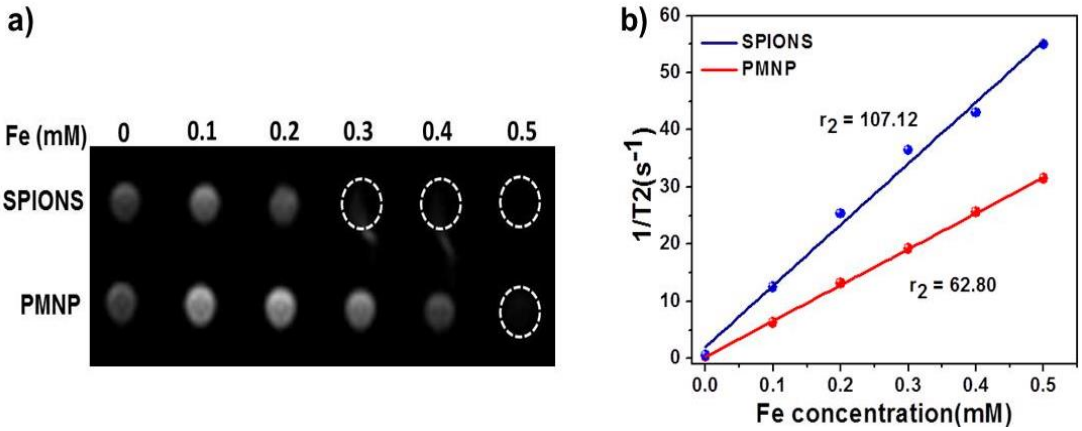

Figure 44. a) MR imaging capabilities and b) magnetic relaxivity calculation of SPIONS and **PMNP**.

4.2.3. Evaluation of chemodynamic therapeutic potential of PMNP

Nanomaterials that can respond to the specific features of TME such as low oxygen concentration, weakly acidic pH environment and high glutathione (GSH) concentrations, hold promising potential for killing cancer cells with high specificity and minimal side effects. In this study, we attempted to demonstrate the potential of **PMNP** for *in situ* glutathione-activated and H_2O_2-reinforced chemodynamic therapy for cervical cancer. In order to assess the TME-fine tuning ability of **PMNP** in solution state, we first estimated the effect of GSH on **PMNP**. During the introduction of GSH to **PMNP**, a sharp enhancement in the concentration of Fe^{2+} ions was observed which went on increasing with increase in the GSH (0-2 mM) concentration, validating the

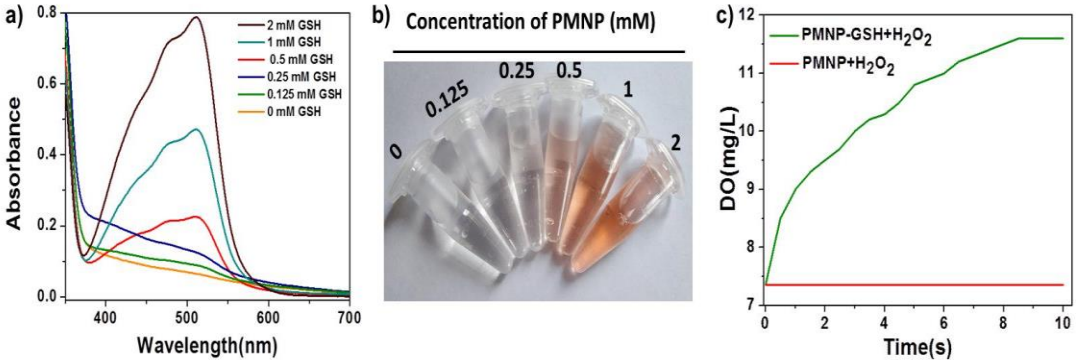

Figure 45. a) UV-Visible absorption spectra and b) photograph showing the reduction of Fe^{3+} ions present in **PMNP** as estimated by 1, 10 phenanthroline assay. c) Quantitative estimation of oxygen generated from the **PMNP** after Fenton reaction.

reduction of Fe^{+3} ions present in the nanoprobe (Figure 45a and 45b). In the meantime, O_2 was also liberated from **PMNP-GSH**, when treated with H_2O_2 *via* Fenton reaction (Figure 45c), which will be advantageous towards diminishing the hypoxic condition in TME. The efficacy of Fe (II) in **PMNP-GSH** to produce ·OH was explored through the degradation of methylene blue (MB) assay. In this study, MB did not exhibit any change while there was only H_2O_2 or **PMNP-GSH** present, whereas it underwent a slight dip when H_2O_2 was added to **PMNP-GSH** owing to the generation of ·OH by Fenton reaction. The degradation of MB caused by the

reaction of **PMNP** with H_2O_2 was very low as compared with **PMNP-GSH** indicating the significant role of GSH for the ·OH radical formation. Moreover, the experiment was carried out in pH 5.4 (lysosomal/endosomal conditions) and pH 7.4 (physiological conditions) to validate the TME- responsive nature of the probe. The absorption of MB at 660 nm got decreased by 4.6% at pH 7.4 and by 8.7% at pH 5.4, indicating the pH-dependent formation of ·OH radicals (Figure 46). The role of PTT for the accelerated production of ·OH by **PMNP-GSH** was then examined at 318 K. As anticipated, MB showed maximum degradation, because temperature rise simultaneously stimulates ionization and increases the ·OH production.

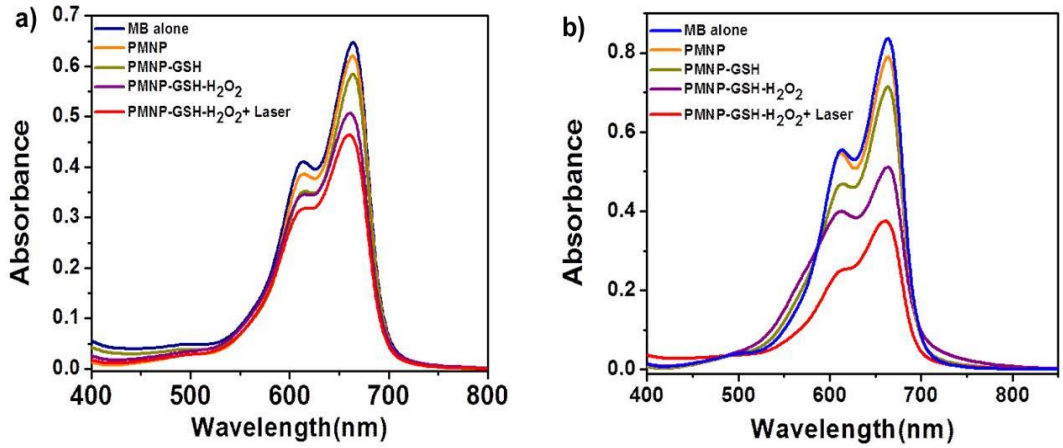

Figure 46. a) Estimation of ·OH generation through methylene blue assay at a) pH 7.4 and b) pH 5.4.

4.2.4. Evaluation of photothermal properties of PMNP

In addition to the chemodynamic therapeutic potential, **PMNP** displayed excellent photothermal efficacies owing to its absorption in the NIR region (Figure 47a). The photothermal ability of **PMNP** depends on its concentration, laser irradiation time, power density etc. When **PMNP** (50 μg/mL) was exposed to 808 nm laser (2 W/cm^2), the temperature was increased from 27.6 °C to 43 °C within five minutes and also exhibited good photostability over five cycles (Figure 47b and 47c). Taken together, these results confirm that **PMNP** has a promising potential as a multifunctional theranostic agent for photoenhanced CDT/PTT.

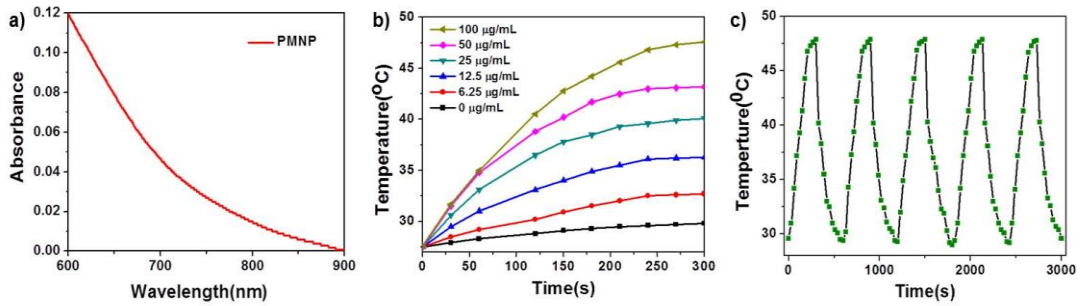

Figure 47. a) represents NIR absorption of **PMNP**. b) Photothermal efficacy of **PMNP** carried out with various concentrations and c) its photothermal stability over five cycles of laser irradiation (2W/cm^2, 5 minutes).

4.2.5. *In vitro* evaluation of CDT/PTT efficacy of PMNP

Inspired by the above results, we further evaluated the TME mediated *in vitro* anticancer efficacy of **PMNP**. As the initial step, the time dependent and TME specific cytotoxic effects of **PMNP** in normal and cancer cells were investigated using MTT assay. As expected, **PMNP** possessed higher toxic effects towards the

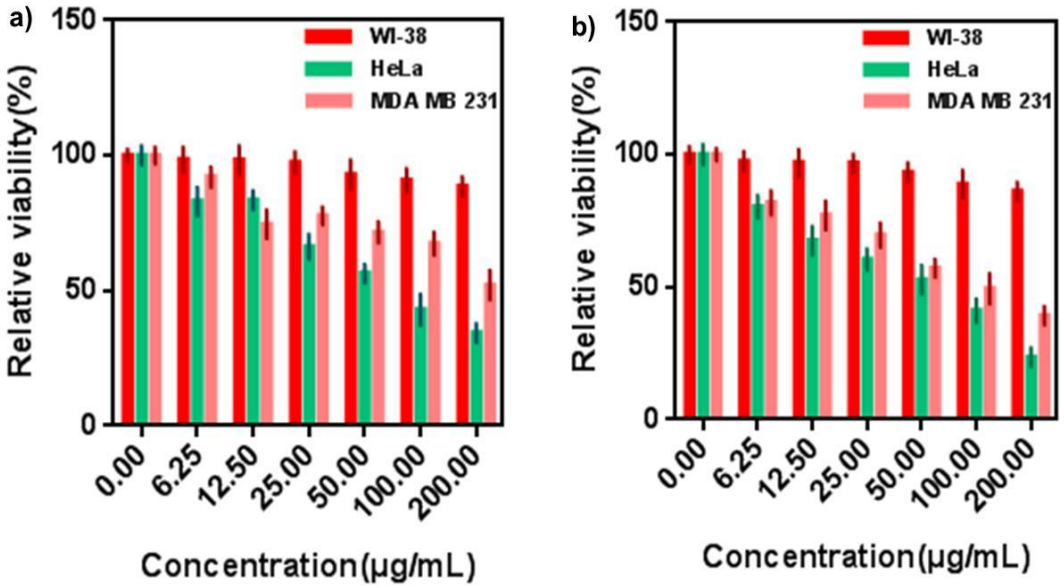

Figure 48. Cytotoxic evaluation of **PMNP** in various cell lines at a) 12 and b) 24 h.

cancer cells as compared to the normal cells (Figure 48). Specifically, when **PMNP** (200 μg mL^{-1}) was treated for 24 h, the cell viability of HeLa cells and MDA MB 231 drastically reduced to 23.5% and 39.3%, respectively. In contrast, **PMNP** produced less cytotoxic effects towards the normal cell line, WI-38 (86.1%). We then

visualized the cellular internalization of **PMNP** through SERS imaging. It is clear from the SERS images that **PMNP** undergoes a rapid cellular internalization which increased with time showing a distribution in the cytosolic regions (Figure 49). After ensuring the localization of **PMNP** in the tumor micro environment, our next intention was to understand the ·OH radical generation of our probe. Since the induction of Fenton's reaction results in the generation of molecular oxygen, we attempted to evaluate the intracellular O_2 generation capability of **PMNP** using a

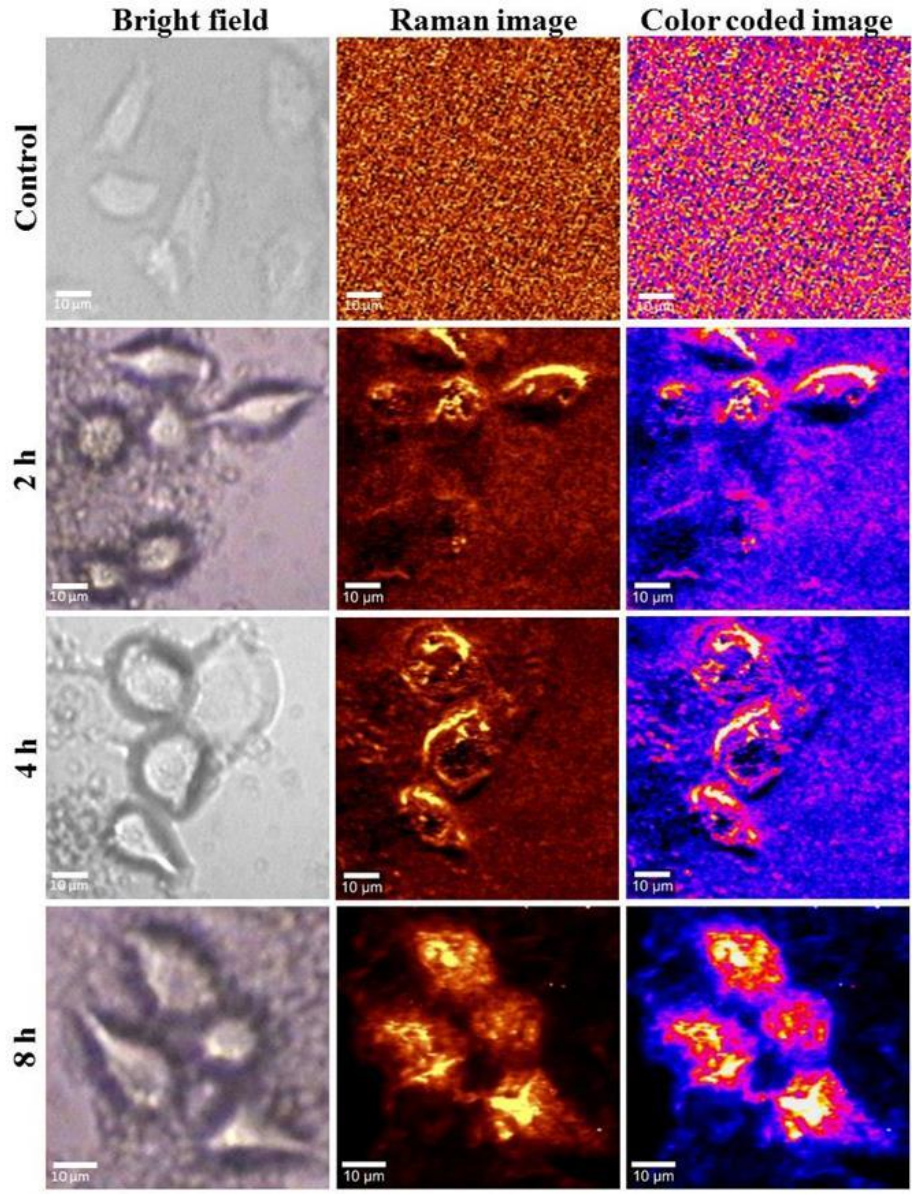

Figure 49. Cellular internalization of **PMNP** on HeLa cells using SERS imaging.

luminescent O_2 probe, $[Ru(dpp)_3]Cl_2$ (RDPP) which serves as a turn-off luminescent probe that undergoes quenching of its emission signal in presence of increasing concentrations of O_2. Towards conducting this study, we have prepared a hypoxic variant of HeLa cells *via* a chemical treatment by administration with cobalt chloride (100 μM, 24 h). In this experiment, the red emission of RDPP was completely quenched by **PMNP** indicating its O_2 generating properties which was more pronounced in the case of cells maintained under hypoxia (Figure 50). This in turn demonstrates that addition of **PMNP** (100 μg mL^{-1}) for 24 h can precisely control the TME conditions very effectively.

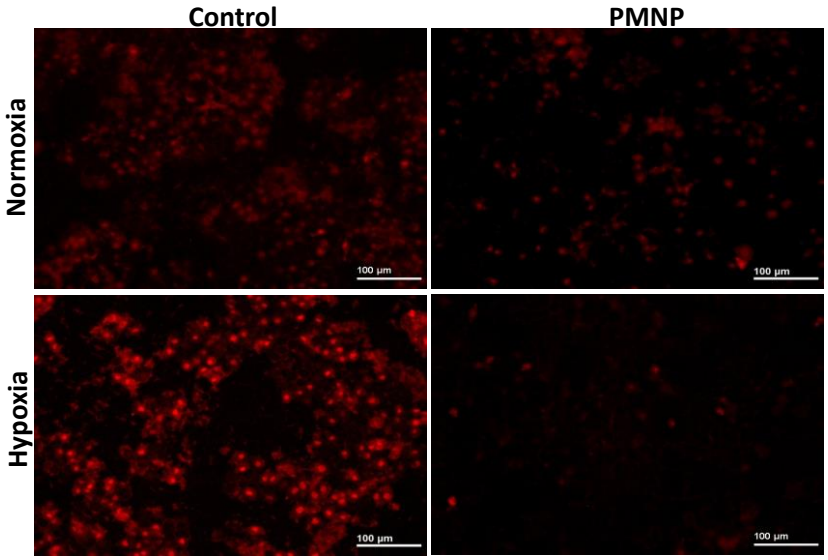

Figure 50. Fluorescence microscopic images of HeLa cells administered with **PMNP** under normoxic and hypoxic conditions and co-stained with luminescence oxygen probe $[Ru(dpp)_3]Cl_2$.

The ROS production efficacy of **PMNP** in the *in vitro* cellular environment (HeLa cells) was examined using 2, 7- dichlorofluorescin diacetate (DCFH-DA) which can be readily oxidized by ROS to give a green emission (Figure 51). Surprisingly, even from the initial time points (0.5 and 1 h), very weak green signals were obtained from the cells incubated with **PMNP** attributed to the production of small amount of ·OH radicals from the probe. This was mainly due to the reaction between the Fe^{2+} ions generated from the reaction between intracellular GSH and **PMNP** with overexpressed H_2O_2 in the intracellular condition. Further we evaluated the photothermal chemodynamic potential of **PMNP** on HeLa cells using live-dead

assay (Figure 52a). The results indicated that, upon the administration of **PMNP** followed by 808 nm laser irradiation, a large population of the cancer cells were killed due to it's the synergistic effect, demonstrating the probability of our probe to kill cancer cells through photoenhanced Fenton reaction properties of **PMNP**. After getting a clear picture of the individual therapeutic capabilities of the nanoprobe, our next intention was to assess the effect of combined therapy on HeLa cells which was accomplished through Annexin V-propidium iodide flow cytometry assay.

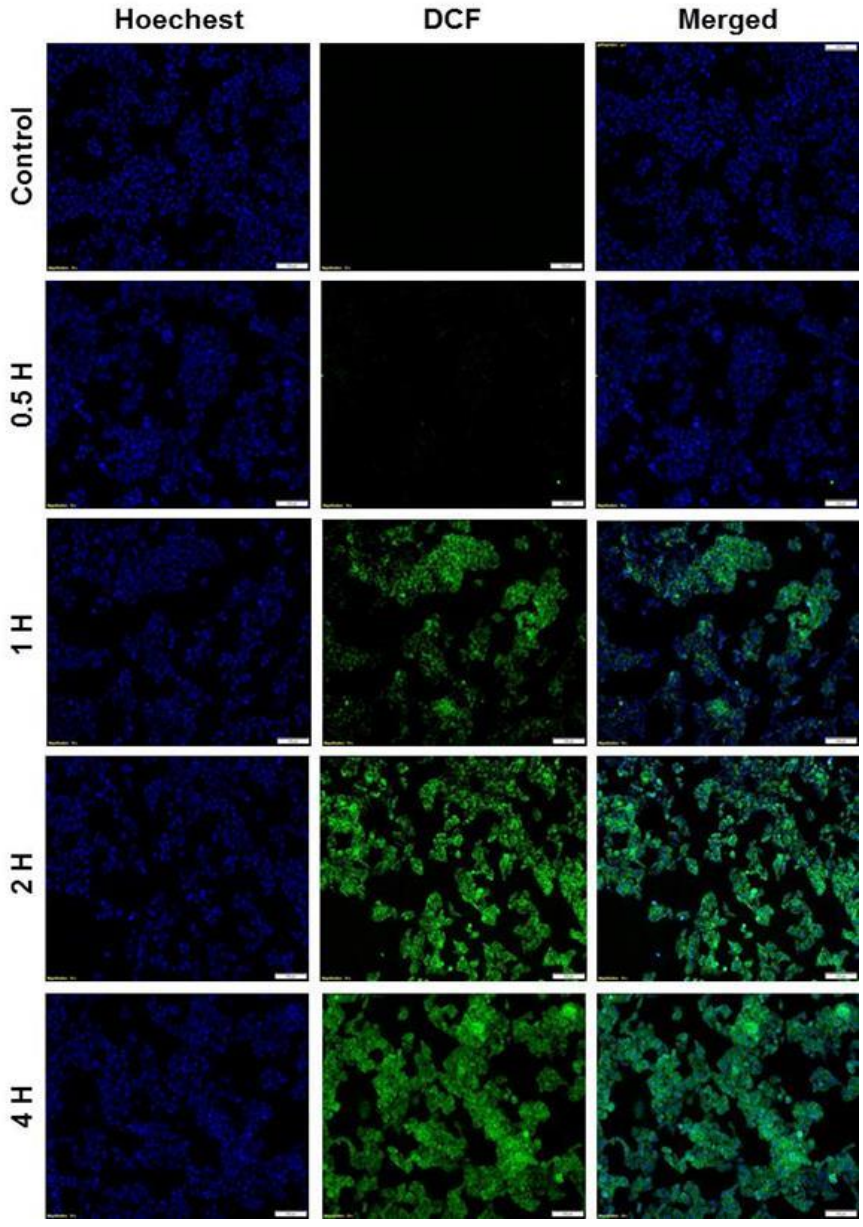

Figure 51. Investigation of ROS generation efficacy of **PMNP** on HeLa cells using DCFDA assay.

The synergistic effect of the combined therapeutic strategy (CDT/PTT) was apparent through flow cytometry as displayed in Figure 52b. As compared to the control, **PMNP** (39.5%) as well as **PMNP** + 808 nm laser (44.2%) treatments induced superior apoptosis under *in vitro* conditions.

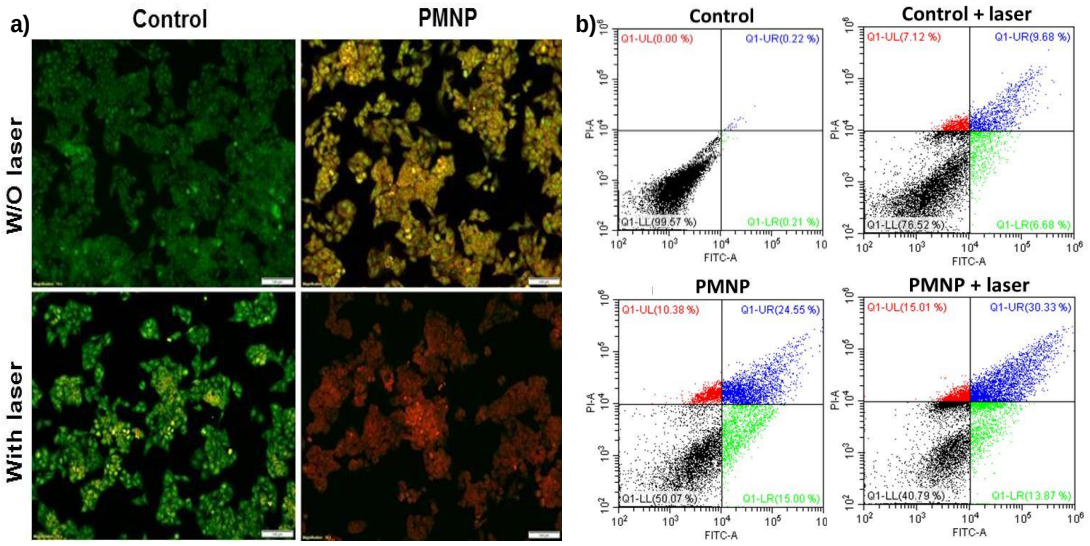

Figure 52. Evaluation of coupled therapeutic effects of **PMNP** and **PMNP** + 808 nm laser using a) live-dead assay and b) flow cytometry assay.

4.2.6. *In vivo* biodistribution of PMNP

Encouraged by the promising results of **PMNP** in the *in vitro* conditions, we further proceeded to investigate its *in vivo* TME mediated theranostic potential by

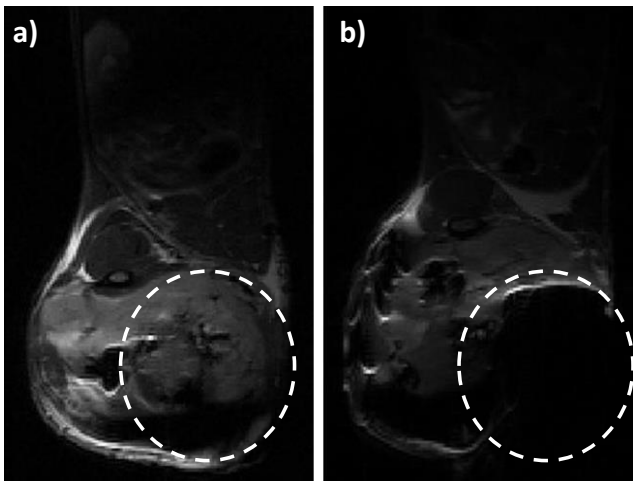

Figure 53. a) Pre and b) post contrast images of **PMNP** injected DLA tumor bearing mice.

intravenous injection into DLA tumor bearing Swiss albino mouse models. Prior to the investigation of therapeutic efficacy of the material, we started with the biodistribution experiments wherein SERS analysis was employed for tracking the localization and distribution of **PMNP** in various organs. Further, we have studied the target specific accumulation of our material through MR imaging analysis, which revealed an enhancement in the image contrast at the tumor site via the shortening of T2 relaxation times. As a result, MR signals underwent a drop in the pixel intensity at the tumor sites owing to the TME responsive tumor homing nature of our probe (Figure 53). Similarly, SERS spectral analysis also indicated that **PMNP** exhibited TME guided targetability at the tumor site as clear from the intense signals obtained from the tumor area 12 h post injection while retaining sufficient intensity even at 48 h, which can be attributed to its remarkable stability in the circulation stream and selective uptake by the tumor cells (Figure 54). Moreover, we have also evaluated the distribution of **PMNP** in various organs like brain, heart, liver, kidney and spleen using spectral intensities of 1330 and 1090 cm^{-1} peaks wherein we could observe a time dependent elimination of the material from liver, kidney and spleen while heart, lungs and brain showed minimal accumulation indicating the safety of the material for *in vivo* therapeutic applications (Figure 54).

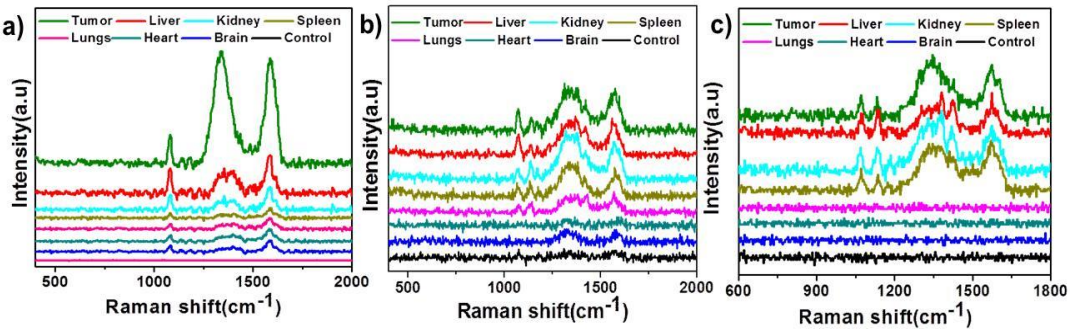

Figure 54. Biodistribution studies of **PMNP** in various organs of mice at a) 12 h, b) 24 h and c) 48 h investigated by SERS analysis.

4.2.7. *In vivo* evaluation of synergistic therapeutic efficacy of PMNP

In order to investigate the TME responsive CDT/PDT therapeutic ability of **PMNP** *in vivo*, DLA tumor-bearing Swiss albino mice were randomnly divided into 3 groups (n=3) *viz.* saline as control, **PMNP** alone and **PMNP** with 808 nm laser. Due

to the specific accumulation of **PMNP** in tumor sites after 12 h, 808 nm laser was irradiated successively at tumor sites (2 W/cm^2) for 5 minutes and the process was repeated at days 3, 5 and 8. Concurrently, body weight and tumor volume of different

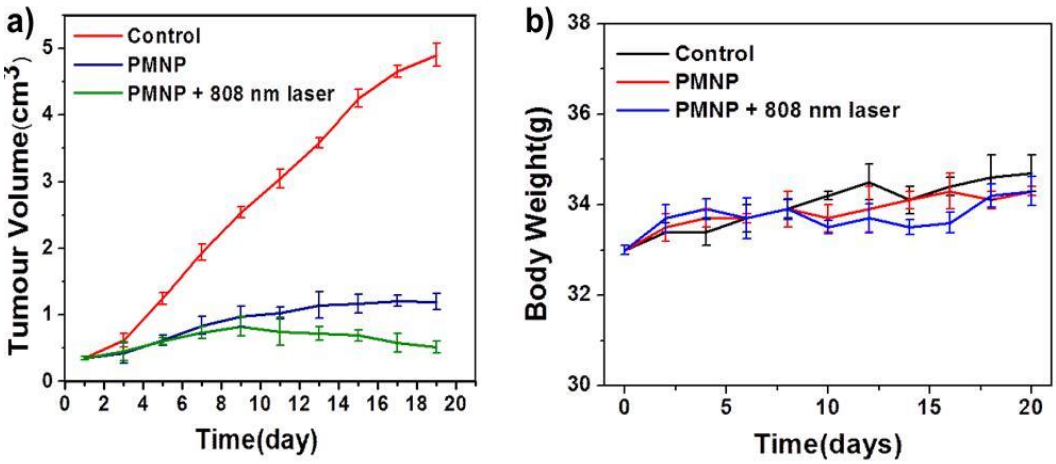

Figure 55. a) Tumor volume reduction studies and b) body weight analyisis of DLA tumor bearing mice after various therapeutic strategies.

groups were monitored daily and the results were plotted against time in order to evaluate the therapeutic effects exerted by individual as well as coupled therapeutic strategies for a period of 20 days. It is interesting to note that, the tumor volumes calculated from mice groups injected with **PMNP** alone and **PMNP** with 808 nm laser showed a significant reduction after 9 days when compared against the control animals (Figure 55a). Furthermore, we diddn‘t observe any significant reduction in

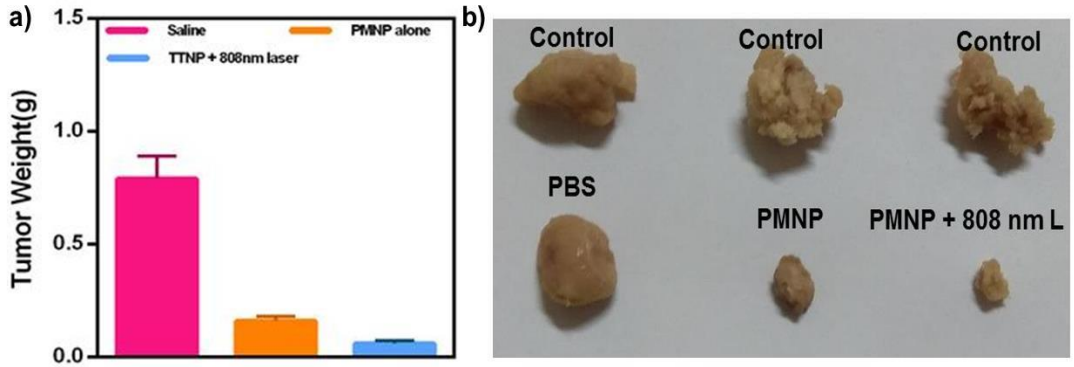

Figure 56. a) Tumor weight analysis and b) photographs showing the reduction in tumor size after various therapeutic actions with **PMNP**.

the body weight of animals under various groups which suggests the biocompatibilty and suitability of **PMNP** for *in vivo* applications (Figure 55b).

After 20 days, all the animals from diffrent groups were sacrificed and the tumor tissues were taken out and weighed. The superior therapeutic effect of the material was apparent from the remarkable decrease in the tumor size (Figure 56b) which was equally reflected in the corresponding mean tumor weights as well (Figure 56a). These results were observed to be in line with the tumor volume experiments i.e, tumor weights of **PMNP** alone as well as those with **PMNP** irradited with 808 nm laser were found to be the lightest as compared to the control group, indicating the TME responsive targeted chemodynamic/photothermal therapeutic efficacy of **PMNP**. Furthermore, the histochemical analysis of various organs were performed using H&E (hematoxylin and eosin) staining which showed severe necrosis to the tumor tissues in mice administered with **PMNP** and those with laser treated **PMNP**. However, no noticeable damage was observed with other organs, which once again validates the potential applicability of **PMNP** as a targeted theranostic nanomaterial for localized therapeutic applications (Figure 57).

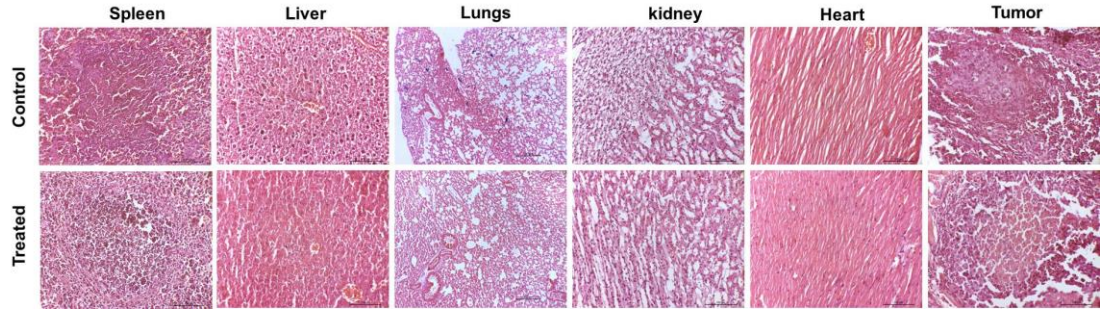

Figure 57. H&E staining analysis of various organs before and after treatment with **PMNP** and laser.

4.3. Design and fabrication of an ultrasensitive centrifugal force based lab-on-a-filter system for the size selective detection of circulating tumor cells

Although, cancer is considered as a localized disease in its pre-mature stages, in certain types of cells, it often becomes innate when patient become symptomatic and result in metastasis, which accounts for 90% of cancer deaths in the world. There are thriving evidences that cancer cells are showered from the primary tumor cells into the circulating blood stream that finally forms metastasis resulting in tumor growth in unexpected body parts. Thus, it becomes critical to identify and quantify the circulating tumor cells (CTCs) during the early stages of tumorigenesis. Recently, CTC has received tremendous attention as a hallmark analyte for non-invasive cancer diagnosis as a result of which more than 270 clinical trials have already been registered utilizing this biomarker. Monitoring of CTC levels may aid in predicting the response to ongoing therapy and developing personalized medicine.

Based on these considerations, CTC enumeration and detection has shown great clinical value, and its prognostic significance has been demonstrated in several types of cancers, including breast, prostate, colon, melanoma, lung cancer etc. Despite the clinical importance and progress of CTC-based cancer diagnostics, it still remains extremely challenging to develop systems to detect CTC in cancer patients as its presence is as low as 1-10 per mL of blood plasma. Moreover, currently available techniques such as pressure-driven microfluidic systems and immunoaffinity-based methods for enriching CTCs are extremely complex and time consuming which poses difficulty in its use in general hospital settings. In this section, we discuss about the fabrication and functioning of a centrifugal force based lab-on-a-filter system which is clog free, highly sensitive and selective towards the rapid isolation of viable CTCs from whole blood without sample pre-treatment.

4.3.1. Device fabrication and working principle of the lab-on-a-filter system

In order to realize a robust and user-friendly CTC isolation platform that can be readily adapted to clinical settings, we developed a custom-designed portable

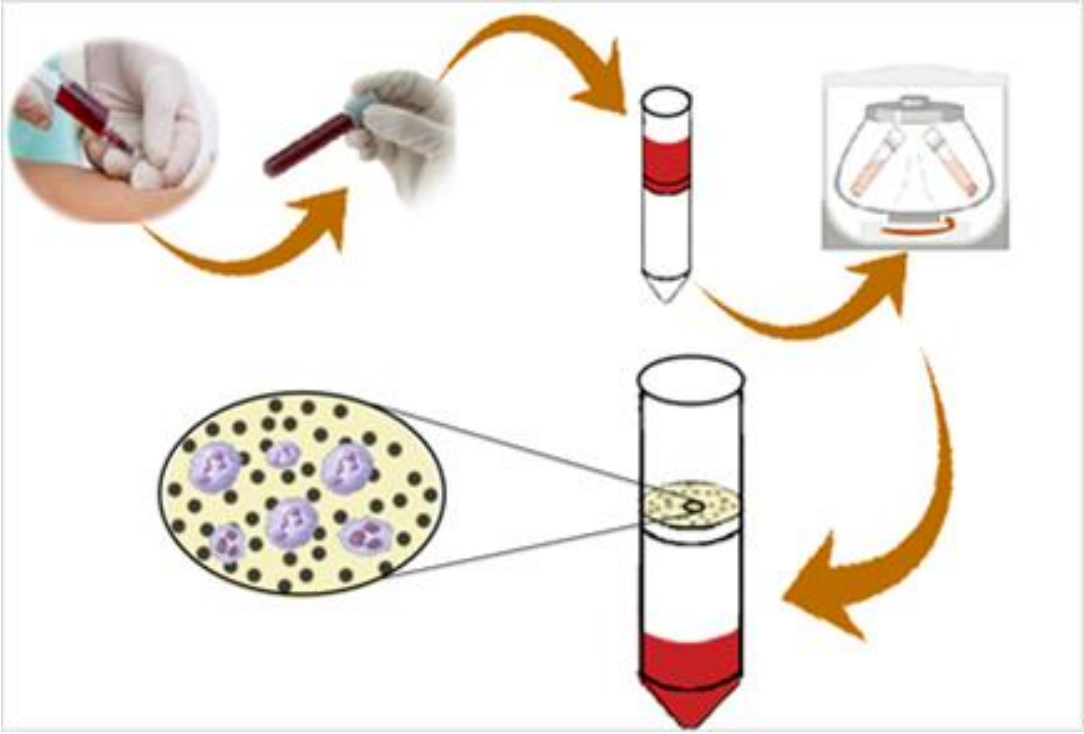

Figure 58. Graphical representation of various stages of CTC separation from the whole blood using lab-on-a-filter system.

centrifugal prototype based size selective lab-on-a-filter CTC detection system for the rapid isolation of CTCs with high purity (Figure 58). The centrifugal prototype comprises of three independent chambers for whole blood sample loading, CTC filtration, and waste residual blood storage (Figure 59). The lab-on-a-filter platform

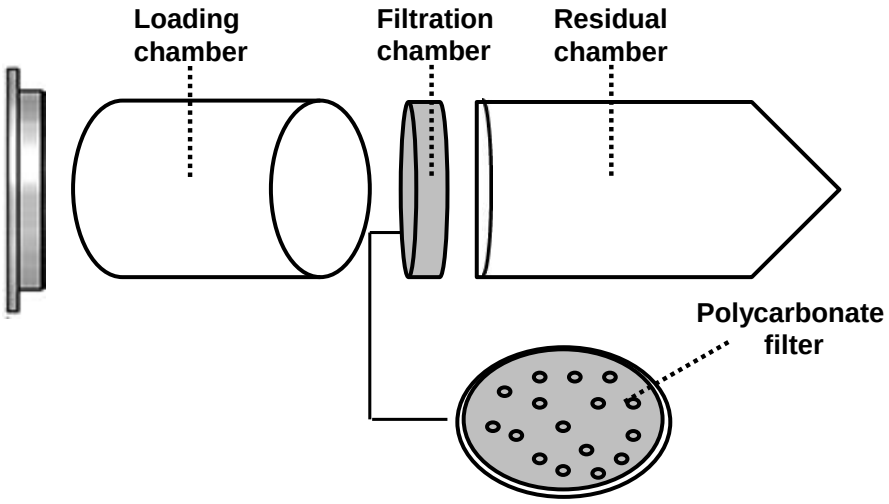

Figure 59. Diagramatic representation of the proposed design of lab-on-a-filter system.

utilizes centrifugal force to rapidly transfer unprocessed whole blood samples from one of the centrifugal prototype chambers to another. Compared with the commercially available CTC detection system, the lab-on-a-filter system offers more effective fluid control because it does not require external interconnectors. Instead, only a simple centrifuge is needed to actuate the fluid flow. Such advantages of the lab-on-a-filter system allow for a reduction in the manual handling steps between the filtration, staining and detection processes. To selectively isolate CTCs based on size differences between CTCs and the surrounding hematologic cells, we have integrated

Sl. No.	**Process**	**State**	**rpm**	**Volume**	**Time**
1	Incubation of whole blood sample with SERS nanotag	Incubation	------	5 mL	60 min
2	Insertion of antibody immobilized PC membrane into the centrifugal prototype	------	------	------	1 min
3	Sample filtration	Flow	2400	5 mL	1 min
4	PBS washing	Flow	2400	2 mL	2 min
5	Fixing	Incubation	------	0.25 mL	15 min
6	PBS washing	Flow	2400	1 mL	1 min
7	Dissolving the PC filter with cells	------	------	0.5 mL	10 min
8	SERS spectral analysis	Incubation	------	0.5 mL	20 min
9	Total time taken for the entire process		1 hr 50 min		

Table 1. Operation protocol for the detection of CTCs using lab-on-a-filter system.

a track-etched polycarbonate (PC) membrane filter on the system. Each chamber of centrifugal prototype was designed in a detachable fashion so that CTC filtration membrane can be easily mounted for the follow-up microscopic analysis and molecular characterization for the accurate detection and quantification of CTC from each sample.

In order to set up a microfluidic system, normally complex apparatus such as tubing, syringe pumps and connectors are compulsory components. In our lab-on-a-filter system, however, a centrifugal prototype and its motor are only required to process samples with quantities up to 5 mL. This provides great platform for establishing a rapid, sensitive and cost-effective CTC detection expertise, which is crucial for the rare-cell-based cancer diagnostics. In our study, the complete progression of CTC isolation and detection was steered on a filter, using a programmed operation procedure. The operation protocol is summarized in Table 1.

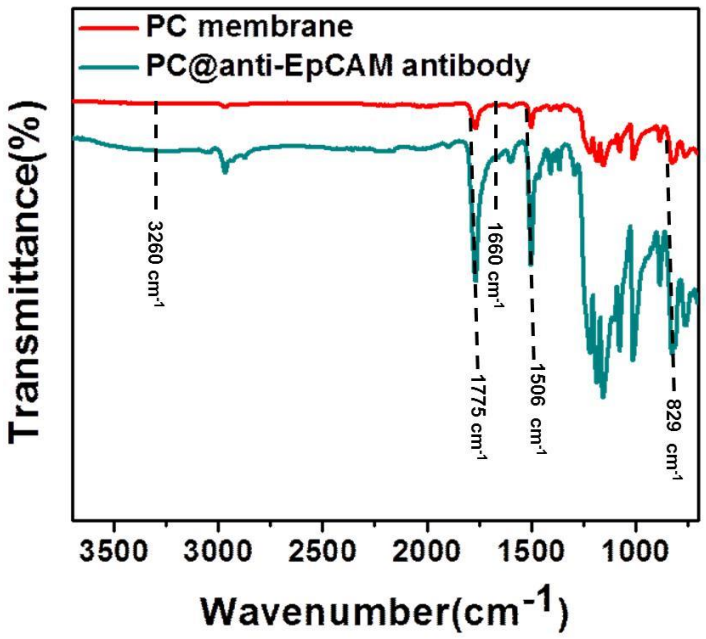

Figure 60. FTIR spectra of PC membrane and anti-EpCAM antibody conjugated PC membrane.

4.3.2. Immobilization of anti-EpCAM antibody over the PC filter

In order to increase the sensitivity and specificity of detection, we have immobilized anti-EpCAM antibody over the polycarbonate membrane which was then confirmed

through FTIR spectroscopy. Initially, the characteristic peaks of untreated PC membrane in the FTIR spectrum were found to appear at 1775, 1506 and 829 cm^{-1} corresponding to the –C=O vibrations of ester groups, aromatic vibrations and out of plane –CH vibrations respectively. Then, the presence of anti-EpCAM antibody on the PC membrane was confirmed through the appearance of peaks at 3260 and 1660 cm^{-1} which corresponds to the amide A and amide I vibrations respectively (Figure 60). Furthermore, we have also validated the antibody immobilization process through immunofluorescence experiments using FITC conjugated IgG for counterstaining the primary antibody (Figure 61). The green fluorescence of FITC was mainly observed from the track etched porous regions of the membrane which indicated the immobilization of antibodies in and around the pores of the PC filter. This will facilitate the retaining of CTCs even at high centrifugational speeds while excluding the WBCs from the whole blood samples.

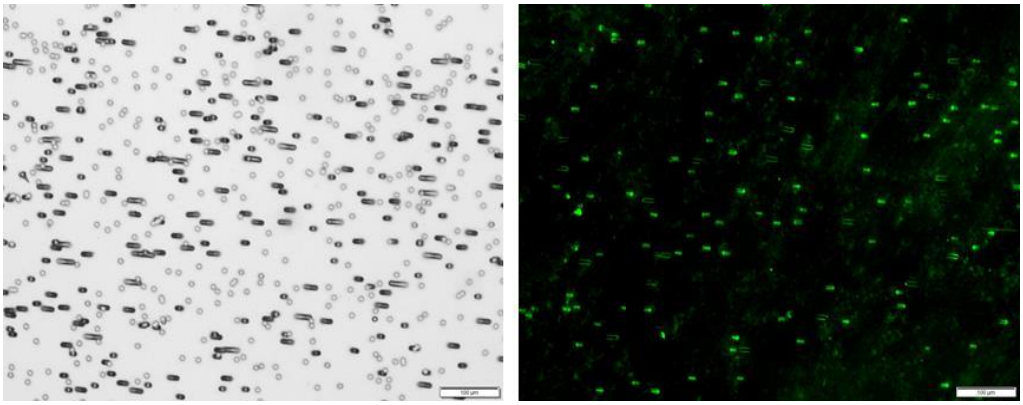

Figure 61. Immunofluorescence microscopic analysis of anti-EpCAM antibody immobilized poly carbonate membrane. Scale bar represents 100 µm.

4.3.3. Preparation and characterization of Au-rGO@anti-ErbB2 SERS nanotag

Preparation of the Au-rGO@anti-ErbB2 SERS nanotag is shown in figure 62. The detailed synthesis procedure of Au-rGO is described in section 3.1.2. In this study, Au-rGO is encoded as a two-in-one system that serves the purpose of SERS substrate as well as Raman signature molecule owing to its Raman enhancement property and characteristic D and G bands present at 1330 cm^{-1} and 1590 cm^{-1} respectively. In

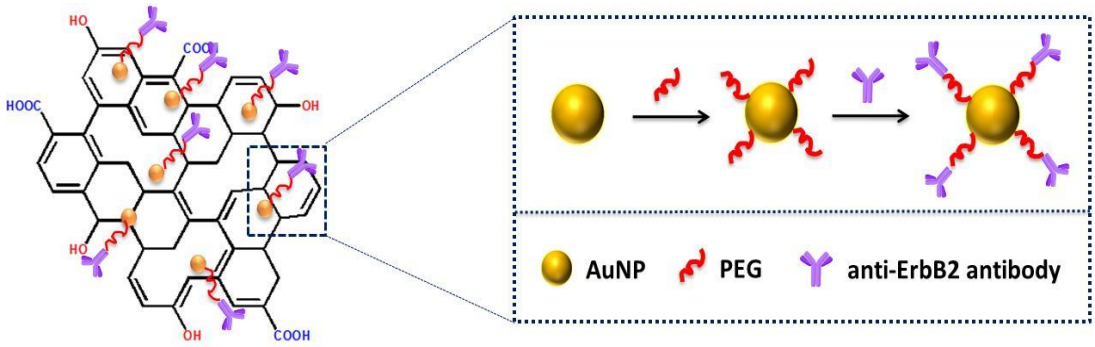

Figure 62. Schematic representation of construction of Au-rGO@anti-ErbB2 SERS nanotag.

order to avoid non-specific interaction with various blood cells, Au-rGO was coated with layers of PEG molecules (methoxy-PEG, SH-PEG-COOH), which will act as a protective layer and behave as a "lying hair" for further functionalization to increase specificity of the system towards CTCs. For that, PEG encapsulated Au-rGO was covalently conjugated with breast cancer specific antibody, anti-ErbB2 to form the Au-rGO@anti-ErbB2 SERS nanotag for the detection and quantification of CTCs among the millions and millions of healthy cells in the human blood stream (Figure 63).

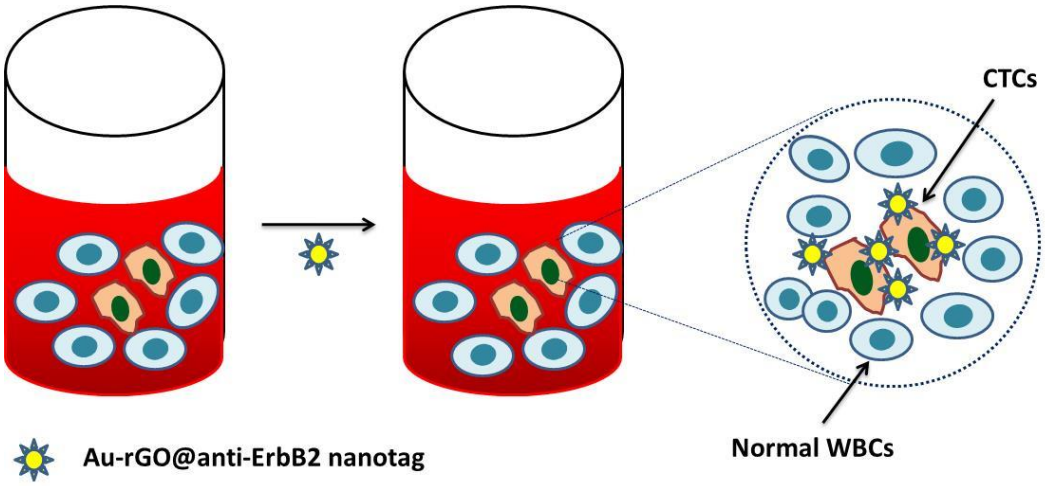

Figure 63. Working principle of Au-rGO@anti-ErbB2 SERS nanotag towards the detection of CTC from whole blood.

The absorption spectrum of Au-rGO was observed at 520 nm but shifted to 532 nm for Au-rGO@anti-ErbB2. The red shift observed in the absorption spectra can be attributed to the change in refractive index around the Au-rGO nanoparticles (Figure 64a). The TEM images of Au-rGO@anti-ErbB2 indicated the stability and well dispersibility of the synthesized nanoparticles (Figure 64b). The hydrodynamic diameter of the Au-rGO@anti-ErbB2 was estimated to be 330 nm when compred against Au-rGO having a diameter of 292 nm (Figure 64c and 64d). Both TEM and hydrodynamic diameter analysis indicated that the protection layer of PEG molecules was very thin, which actually helps to reduce the SERS weakening effect.

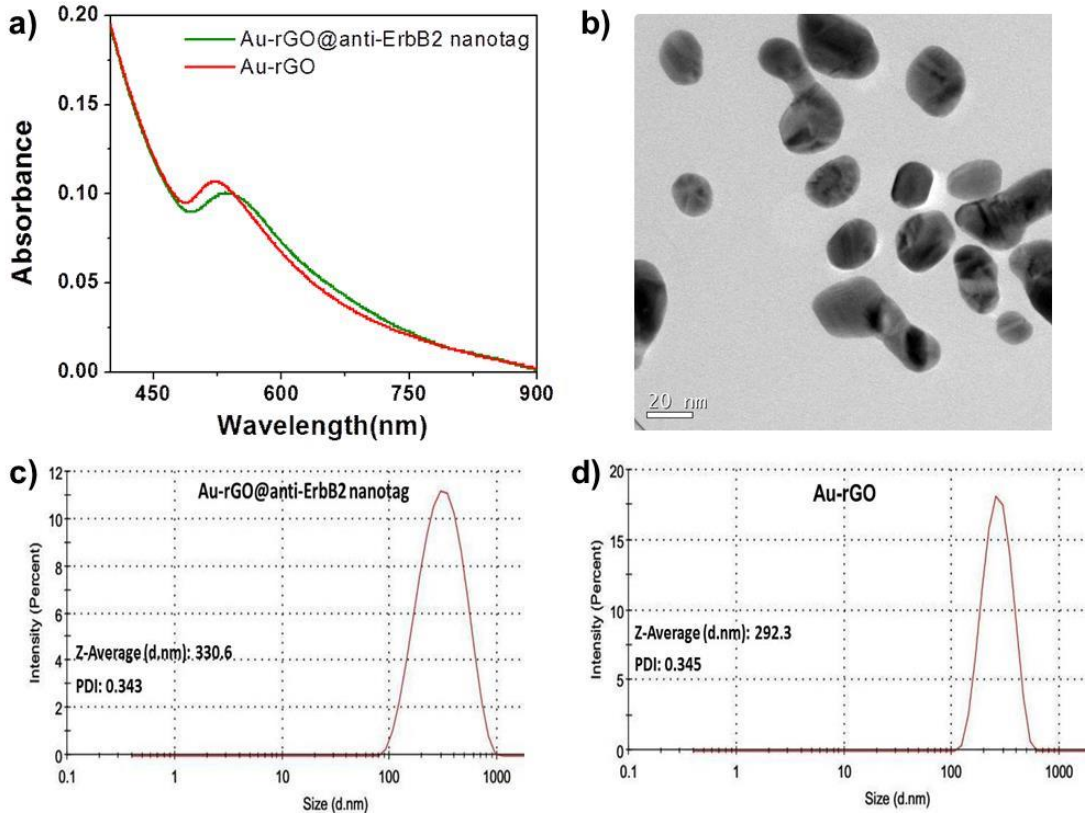

Figure 64. a) UV-Visible absorption spectrum and b) TEM image of Au-rGO@anti-ErbB2 SERS nanotag. c) and d) represent the hydrodynamic diameters of Au-rGO@anti-ErbB2 and Au-rGO respectively.

As a preliminary step, we have optimized the concentrations of Au-rGO, PEG and anti-ErbB2 antibody for the synthesis of highly stable SERS nanotag, Au-rGO@anti-ErbB2. The optimized concentration of different elements and their

corresponding SERS intensities are summarized in Table 2. It is found that the SERS intensity of Au-rGO increased with increase in concentration from 25 to 100 μg/mL (Figure 65a and Table 2). However, it is important to note that the signal intensity at 1330 cm^{-1} remained almost the same while increasing the concentration from 75 to 100 μg/mL which prompted us to fix the concentration of Au-rGO at 75 μg/mL for the subsequent experiments. Having fixed the concentration of Au-rGO, our next intention waas to study the effect of PEG coating in getting a stable nanotag suited for biological screening applications. The SERS intensity of PEGylated Au-rGO was found to be relatively low when the concentration of PEG molecules were 5 μg/mL but showed stronger signals in concentration ranging from 0.5 to 2 μg/mL (Figure 65b and Table 2). This effect indicates that the over package of the Au@rGO nanoparticles by protective polymers can influence its SERS signal intensity. Thus, fixing the optimal concentration of PEG molecules at 0.5 μg/mL in the subsequent

Construct	**Conc. of Au-rGO (μg/mL)**	**Conc. of PEG (μg/mL)**	**Conc. of anti-ErbB2 antibody (μg/mL)**	**SERS intensity at 1330 cm^{-1} (a.u)**
Au-rGO 1	25	-	-	23
Au-rGO 2	50	-	-	39
Au-rGO 3	75	-	-	58
Au-rGO 4	100	-	-	58
Au-rGO PEG 1	75	5	-	24
Au-rGO PEG 2	75	2	-	42
Au-rGO PEG 3	75	0.5	-	50
Au-rGO@anti-ErbB2 1	75	0.5	6	78
Au-rGO@anti-ErbB2 2	75	0.5	36	300

Table 2. Optimized conditions and respective SERS intensities towards the synthesis of nanotag.

experiments will provide an opportunity for the conjugation of more anti-ErbB2 antibodies to the Au-rGO system. The final nanotag, Au-rGO@anti-ErbB2 possessed much stronger SERS signals than the Au-rGO or PEGylated Au-rGO system because it was concentrated 6 fold by ultracentrifugation prior to SERS and CTC detection experiments (Figure 65c and Table 2).

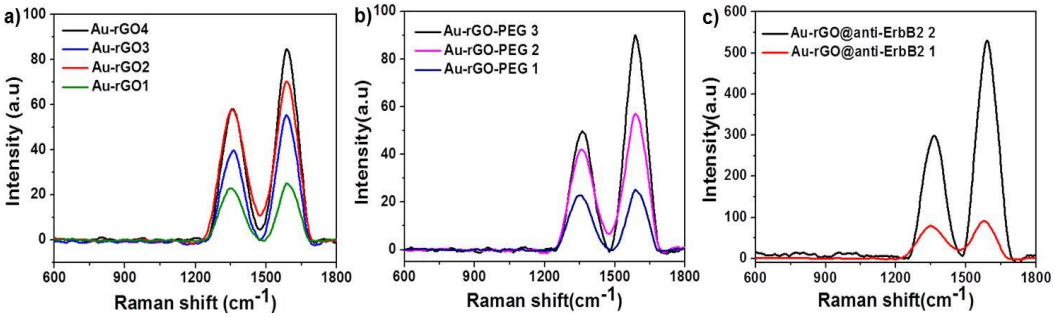

Figure 65. SERS spectral analysis performed with different concentrations of a) Au-rGO, b) PEG and c) Au-rGO@anti-ErbB2 antibodies.

After the successful synthesis of SERS nanotag, we moved on to optimize various parameters in order to realize an effective isolation protocol for CTCs. Briefly, whole blood spiked with cancer cells was incubated with Au-rGO@anti-ErbB2 for 60 minutes. The incubated blood was then transferred in to the loading chamber of the centrifugal prototype and spun at different centrifugal speeds for 60

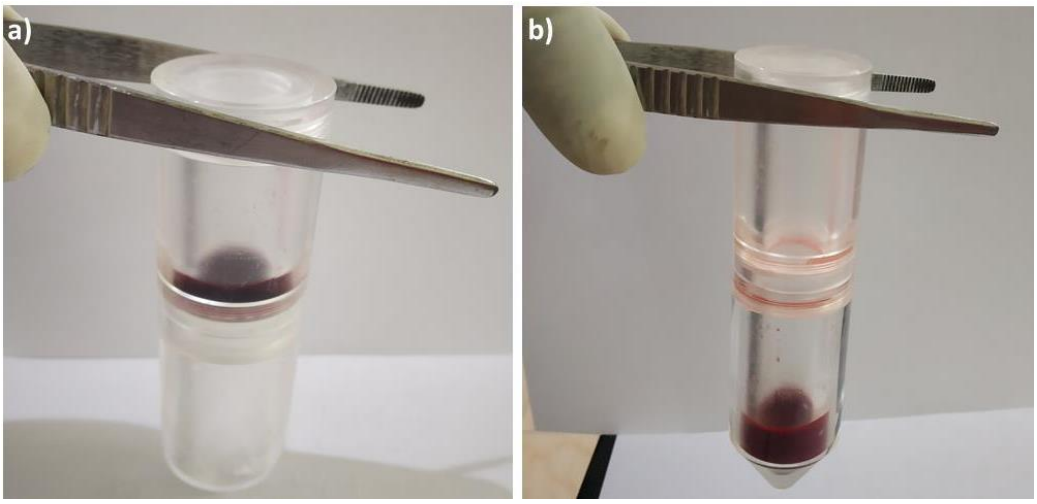

Figure 66. Photographs representing the working of lab-on-a-filter system before (a) and after (b) filtration.

seconds (Figure 66a). Then, the lab-on-a-filter system was subjected to two steps of washing using PBS. During this step, the unbound nanotag and other blood components will be removed from the filter system (Figure 66b). The filter was then removed from the filter chamber which was dissolved using chloroform and pelletized with the captured CTC. The pellet obtained from the filter was then illuminated by 633 nm laser and a SERS spectrum was recorded to evaluate the amount of Au-rGO@anti-ErbB2 SERS nanotag. The SERS signal intensity corresponds to the number of CTCs present in the whole blood along with the WBCs.

In order to prevent the cells from experiencing significant damage, the range of centrifugal force used in all the experimental conditions in this study was limited to 600, 1200, 1800 and 2400 rpm. The above mentioned centrifugal forces were chosen on the assumption that the captured cells will be present at the utmost outer edge of the filtration unit. The average capture efficiencies for the 2400, 1800, 1200 and 600 rpm were found to be 55 ± 5% (n = 6), 59 ± 3% (n = 6), 64 ± 3% (n = 6) and 83 ± 3% (n = 6) respectively (Figure 67a). Among various centrifugal conditions, the highest capture efficiency was obtained with 600 rpm speed, which exhibited a substantial difference from the rest of the spin conditions ($P < 0.0001$, t-test). However, the capturing efficiency obtained from spinning experiments from 1200 to

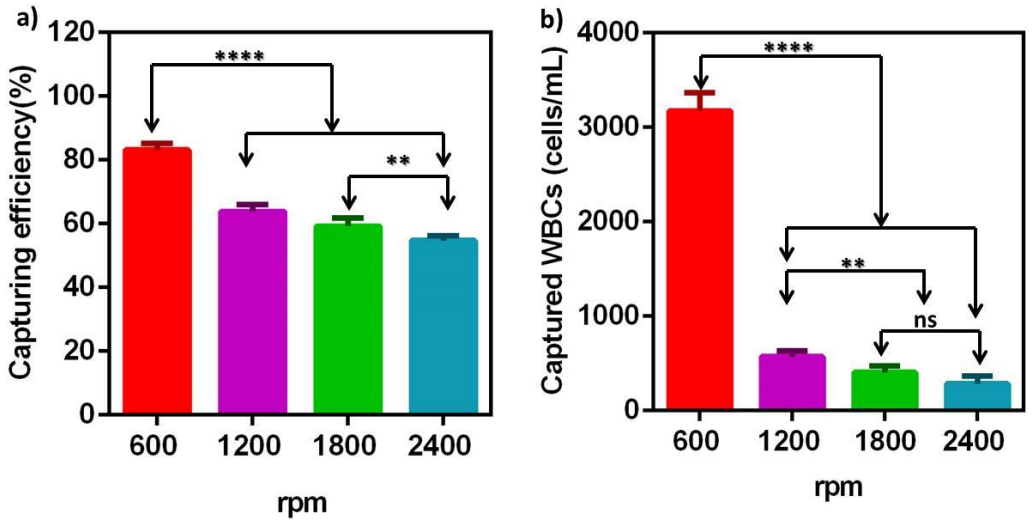

Figure 67. Quantitative evaluation of the effect of centifugal speed on the capturing efficiency of CTCs (a) and WBC counts (b).

2400 rpm didn't show any significant difference. The WBC counts obtained from 2400, 1800, 1200 and 600 rpm were 285 ± 53 cells (n = 3), 403 ± 61 cells (n = 6), 573 ± 51 cells (n = 6) and 3175 ± 286 cells (n = 6) respectively (Figure 67b). Even though spin speed at 600 rpm showed maximum capturing efficiency of cells, it lacks purity and transfer of blood through the filter system. Thus, for better blood purity and maximum capturing of the cells, the optimum rpm for the centrifugal filtration was fixed at 1800.

The most frequently encountered problem for majority of the CTC isolation platform is the membrane clogging. It can be solved either by density gradient centrifugation or RBC lysing. But, pretreatment of blood samples may result in significant loss of CTCs present in the blood serum. Thus, dilution is the only available blood pretreatment method to avoid membrane clogging. Using lab-on-a-filter system, we evaluated the effect of dilution factor on the capturing efficiency. For each trial, 1 mL of the whole blood (WB) was mixed with various amounts of PBS (0-3 mL) and spiked with approximately 100 SKBR3 cells. Then it was

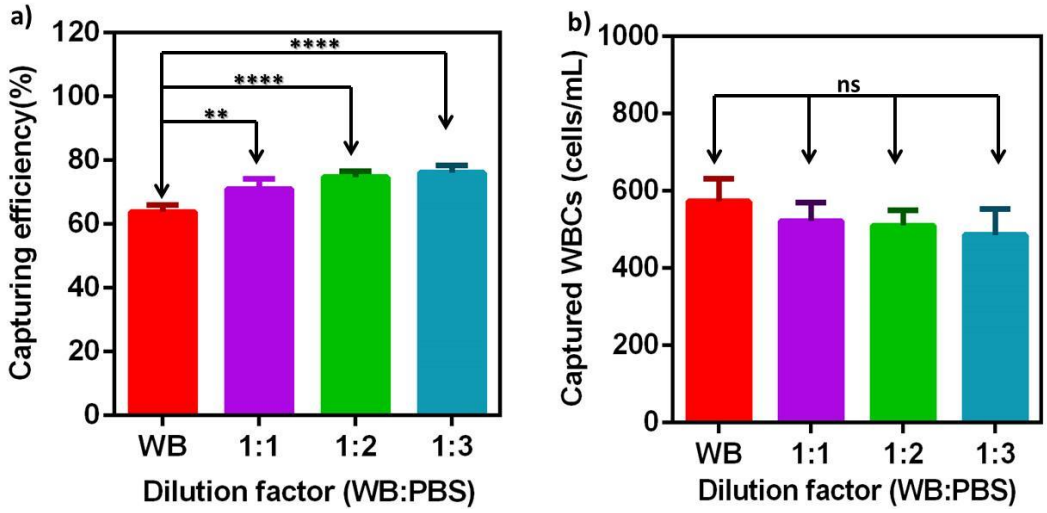

Figure 68. Quantitative estimation of the effect of dilution on the capture efficiency of CTCs (a) and WBC counts (b).

processed at 1800 rpm for 60 seconds. Average capture efficiencies for each condition were 64 ± 1%, 71 ± 2%, 75 ± 4%, and 76% ± 2%, respectively (n = 6) (Figure 68a) while the average WBC counts turned out to be 573 ± 40, 521 ± 71, 510 ± 144, and 487 ± 83 for the respective conditions (n = 6) (Figure 68b). These

results imply that dilution factor is not a critical component affecting either the capture efficiency or purity ($P < 0.05$, ANOVA).

4.3.4. Specificity and sensitivity of Au-rGO@anti-ErbB2 SERS nanotag for the detection of CTCs

SERS spectroscopy is well known for its selectivity and sensitivity as compared to other imaging modalities. It is capable of detecting even a single molecule or single cell with high multiplexing efficacies. The main challenge encountered during this work was to reduce the non-specific binding of Au-rGO@anti-ErbB2 SERS nanotag to other blood cells, which outstrips CTCs by several orders of magnitude. Initially, in order to increase the sensitivity of detection, control experiments were carried out to nullify the external factors which could lead to false negative results. For that, SERS spectra of whole blood and polycarbonate membrane were recorded which was compared with that of AurGO@anti-ErbB2 tag to identify the least interfered peak present in the nanotag to account for the accurate number of CTCs. After the detailed investigation, intensity variation of D band of Au-rGO@anti-ErbB2 located

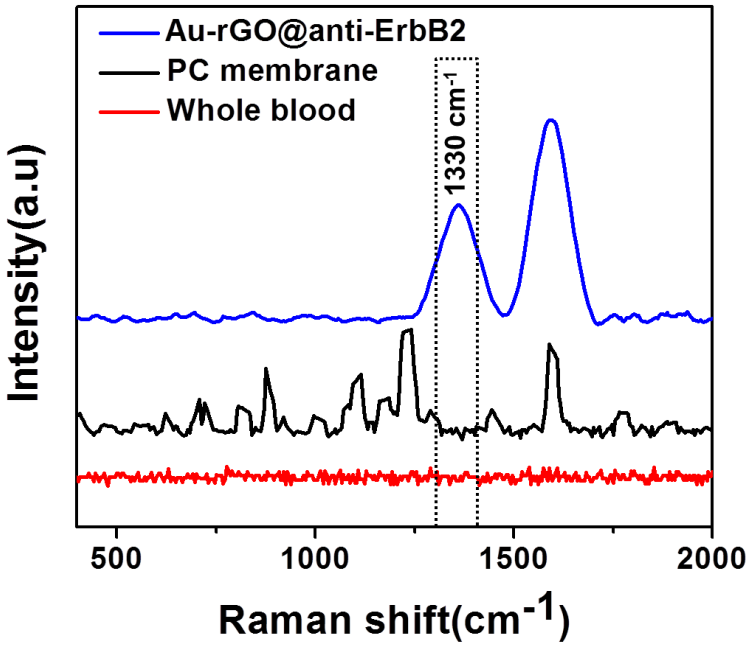

Figure 69. SERS spectral comparison between Au-rGO@anti-ErbB2 nanotag, PC membrane and whole blood.

at 1330 cm^{-1} was chosen as the correlative assessment peak of CTCs present in the given volume of whole blood (Figure 69).

In a proof-of-concept experiment, the target specificity of Au-rGO@anti-ErbB2 was evaluated using human breast cancer cell line, SKBR3 cells. In this study, SKBR3 cells (~10,000) were spiked into 1 mL of whole blood and incubated with

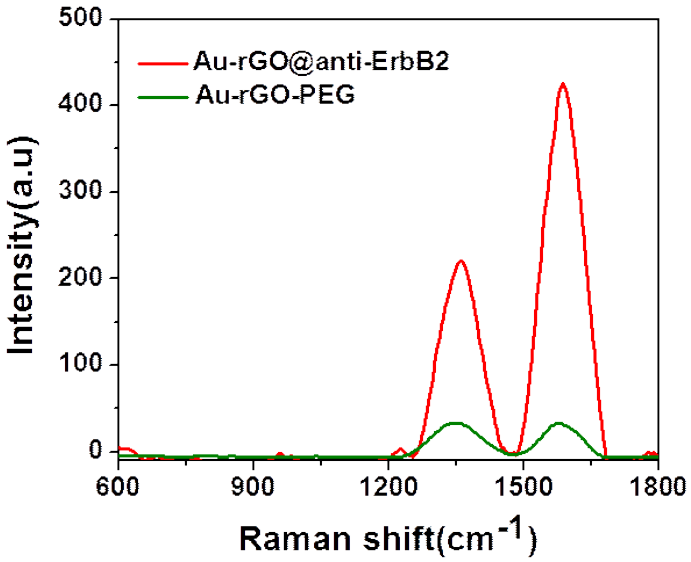

Figure 70. Specificity of Au-rGO-PEG and Au-rGO@anti-ErbB2 towards SKBR3 cells.

nanotag. Target specificity of Au-rGO@anti-ErbB2 was established by the strong SERS signals located at 1330 cm^{-1} of graphitic material present in the nanotag. However, only negligible signals were obtained from the samples incubated with PEGylated Au-rGO nanoparticles (Figure 70), illustrating the minimal non-specific binding.

To define the sensitivity of the experiment, different number of SKBR3 (5, 10, 25, 50, 100 and 500) cells were spiked into 1 mL of whole blood and each incubated with 100 µL of Au-rGO@anti-ErbB2 tag and followed the filtration process as mentioned in the above section (Figure 71a). The SERS spectra were measured from the pellets of filter and tagged CTCs using 633 nm laser excitation. A correlative plot of relative SERS signal intensity against the number of spiked cells is displayed in figure 71b. The relative or comparative fraction was quantified by estimating from the SERS signal intensity of peak at 1330 cm^{-1} of the

pellet. The limit of detection of our lab-on-a-filter system was estimated to be of 5 tumor cells/mL of whole blood as evident from the linear correlation graph.

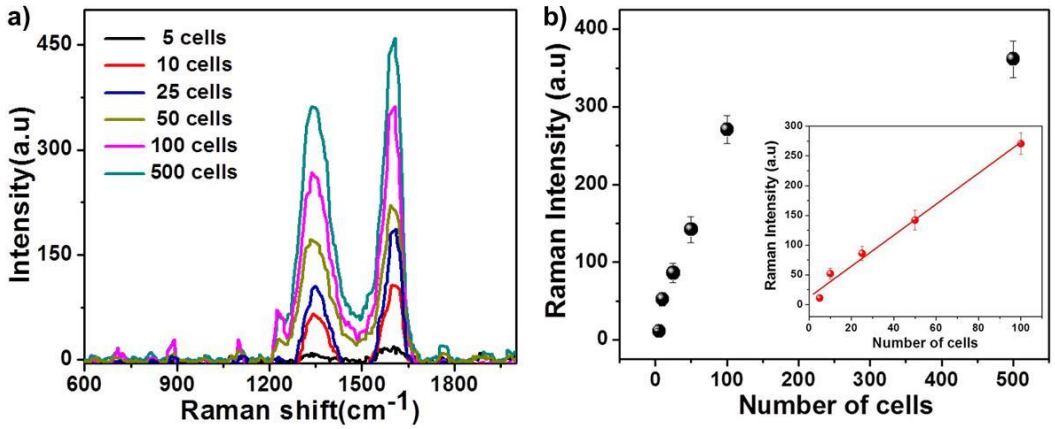

Figure 71. a) Detection specificity of lab-on-a-filter system for SKBR3 cells in whole blood and b) plot of Raman intensity against number of SKBR3 cells for LOD detection.

4.3.5. Fluorescence immunostaining for the detection of CTC

We have performed the fluorescence immunostaining studies to validate the SERS enabled CTC detection efficacies of our lab-on-a-filter system. In order to investigate

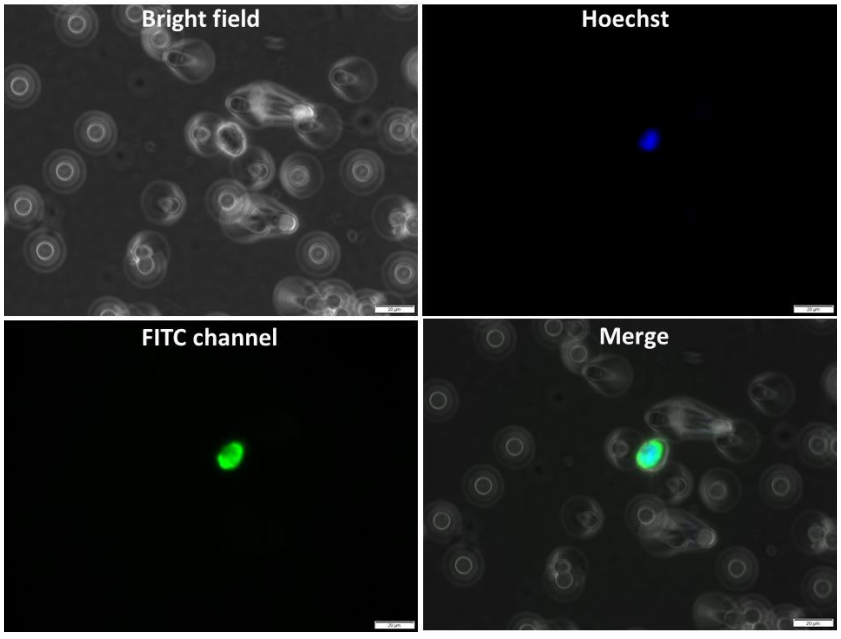

Figure 72. Fluorescence microscopic analysis of capture and isolation of SKBR3 cells using lab-on-a-filter system.

the capture efficiency of lab-on-a-filter system using whole blood samples, varying number of SKBR-3 cells (5–10 cells, 20–50 cells, 50-100 cells and 500-1000) were spiked into 1 ml of whole blood and filtered through the lab-on-a-filter system. (Figure 72). To differentiate captured CTCs and WBCs, fluorescence immunostaining was performed using anti-cytokeratin and anti-CD45 antibodies, where WBCs were identified as positive for hoechst and CD45, a common leucocyte antigen, while CTCs were identified as positive for hoechst and cytokeratin (CK),

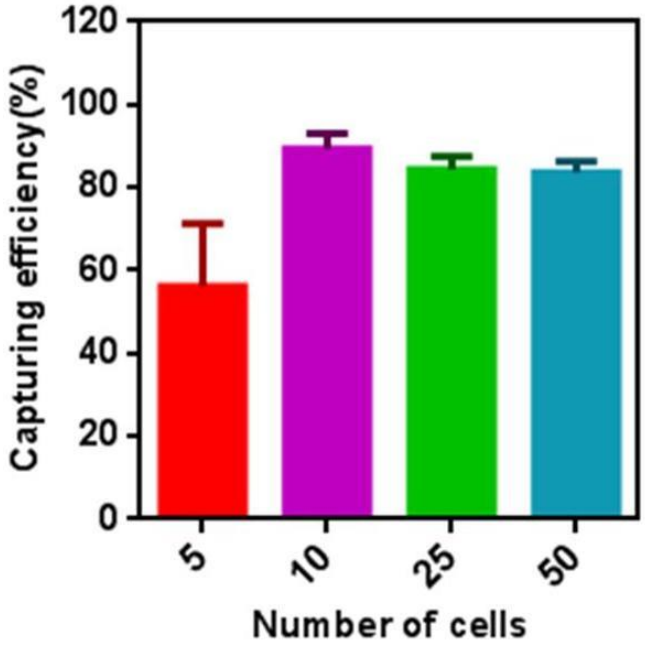

Figure 73. Capturing efficiency of lab-on-a-filter system using immunofluorescence staining.

but negative for CD45. The average recovery rates of 10, 25 and 50 spiked cells per 1 ml were 89.2% (n = 6), 84% (n = 6) and 83% (n=6), respectively (Figure 73). In the case of 5 spiked cells per 1 mL, the average recovery rate was 56% (n = 6). The higher standard deviation in this group may be explained by the inherent limitations in capture with cell numbers at low levels. These observations were found to be in well agreement with our SERS based detection strategy which facilitates a rapid and sensitive detection that may aid in the early stage screening of cancer.

Chapter 5

Summary and Conclusion

Chapter 5

Summary and Conclusion

The creation of novel functional nanomaterials for the detection and monitoring of a range of important target materials and biological events *in vivo* and *in vitro* is a great challenge in clinical diagnostics and chemical biology. Understanding the molecular interactions in living system in their native habitat is a great challenge, particularly in the area of cancer theranostics and clinical diagnostics. In the last few decades, owing to the high toxicity and side effects of anticancer drugs with large dosage, research fraternity has been focusing on the development of functional metamaterials with assemblies of diverse functional groups and nanoparticles, such as anticancer drugs, photosensitizers and photothermal agents onto the carriers, in order to achieve controlled drug release to perform targeted therapy without damaging the normal tissues. The development of multifunctional molecular diagnostic platforms for concordant visualization and treatment of diseases with high sensitivity and resolution become a crucial strategy in cancer management. Thus, engineering functional metamaterials with high therapeutic and imaging capabilities to elucidate diseases from morphological behaviors to physiological mechanisms is an unmet need in the current scenario. Among various metamaterials, plasmonic assemblies of graphene-gold hybrids are considered as fascinating “hot carriers”, where gold nanoparticles act as antennas to exploit its surface plasmon resonance and initiate the inherent near field coupling between graphitic materials to assist new platform with distinct favorable features to exploit its synergistic effect in theranostics. Thus, in our research work, we have developed various nanohybrids of graphene–gold nanocomposites for potential applications in biosensing, imaging and therapy.

In order to accomplish this angle, in the first part of the study, we have adopted a novel strategy for the construction of a nanoframework comprising of plasmonic gold-graphene hybrids tethered with folic acid ligated chitosan modified photosensitizer to afford target specific photothermal and photodynamic therapy. The hybrid vehicle also served as an excellent carrier for efficient loading and stimuli responsive release of the chemotherapeutic drug doxorubicin (DOX) to enhance the therapeutic efficacy, thereby forming a trimodal nanomedicine against cancer. In addition, it is very critical to recognize the state of these therapeutic agents both after *in vitro* and *in vivo* treatments. Thus, our nanoprobe is constructed in such a way that, these therapeutic regimes can be suitably assisted with simultaneous fluorescence and SERS imaging efficacies, a rare event to occur together in tumor homing environments. More importantly, our nanoconstruct exhibited synchronized therapeutic effects which resulted in the effective regression of tumor volume without propagating any toxic effects to the other organs of the animals. Taken together, by virtue of strong light-matter interactions, our nanoprobe showed enhanced photo-adsorption which facilitated the amplified light reactive therapeutic and imaging efficacies along with targeted and enhanced chemotherapy, both *in vitro* and *in vivo*, which may offer a promising outcome in clinical research.

In the second part of the study, we designed and developed a nanoarchitecture comprising of gold graphene hybrids functionalized with super paramagnetic iron oxide nanoparticles to realize a multifunctional theranostic tool for cancer management. The probe was fabricated by coupling Au-rGO with SPIONS through 4-aminothiophenol which served the role of a linker as well as a Raman reporter. The probe performed its chemodynamic therapeutic potential by smartly utilizing the tumor microenvironment features of low pH, high GSH and high H_2O_2 to produce highly cytotoxic hydroxyl radicals via a Fenton reaction. Moreover, we could precisely utilize the NIR absorbing properties of our nanoconstruct to induce a photothermal therapeutic effect, thereby affording a synchronized dual therapy on cancer cells. Furthermore, the hybrid probe served as an efficient platform for magnetic resonance imaging which produced a T2 contrast utilizing the super paramagnetic nature of the material. The inherent Raman signatures of the probe

allowed us to utilize its SERS imaging capabilities for visualizing its internalization and localization in the tumor cells. The promising attributes of the probe facilitated effective therapeutic efficacy on tumor bearing mice models which highlights the applicability of our nanosystem for *in vivo* cancer treatment. In view of the increasing demand for nanomaterials in cancer detection and treatment, the as-developed system is expected to serve as a promising tool for targeted imaging guided cancer therapeutics.

In the third part of the study, we designed and fabricated a user-friendly CTC isolation platform that can be easily adapted to the current clinical settings. In order to accomplish that, we developed a size selective lab-on-a-filter system built over a custom-designed portable centrifugal prototype for the rapid isolation of CTCs. The centrifugal prototype was designed with three different chambers for blood sample loading, CTC isolation, and residual blood storage. The lab-on-a-filter platform exploits centrifugal force to quickly transfer unprocessed blood samples from one chamber to another. Compared with the commercially available CTC detection system, the lab-on-a-filter system can offer more effective fluid control because it does not require external interconnectors. Instead, only a simple centrifuge is needed to actuate the fluid flow. Such advantages of the lab-on-a-filter system allowed for a reduction in the manual handling steps between the filtration, staining and detection processes. In order to isolate CTCs based on size differences between CTCs and blood cells, we integrated a 10 μM pore size track-etched polycarbonate (PC) membrane filter on the system. The PC membrane sitting portion in the isolation chamber was fabricated in such a way that, it can be transported to various imaging analyses after the filtration process. CTC detection sensitivity and selectivity experiments were initialized with cell spiking of different cancer cells in PBS as well as normal human blood to standardize and distinguish CTCs from the other blood parameters (like RBC, WBC, platelets etc.). In order to further improve the sensitivity of detection, a SERS nanotag built on Au-rGO@antiErbB2 was employed which played a key role in the isolation and quantification of CTCs among the millions and millions of healthy cells in the human blood stream. For performing cell spiking experiments in PBS as well as in whole blood samples, the suspension (1

mL, ~1 to 100 cells/mL) was initially injected into the upper loading chamber of the centrifugal prototype. Then, the prototype was placed in a rotor and allowed to spin at various rpm. During this process, cells gets transferred to the filter membrane placed in the middle chamber after which the residual liquid was allowed to flow to the third and final collection chamber. After the filtration, two steps of PBS wash were carried out to remove residual liquid, if any, present in the filter membrane. The estimated time required to separate 5 mL of sample was about 60 s, which is a considerably less time compared to earlier reported procedures. Since each chamber of centrifugal prototype was designed in a detachable fashion, it was easy to detach and mount the CTC filtration membrane for the follow-up microscopic analysis and molecular characterization for the accurate detection and quantification of CTC from each sample. Thus, as compared to most of the immunoaffinity-based CTC isolation platforms, our centrifugal force based lab-on-a-filter system proved to be a clog free, highly sensitive and selective platform towards the rapid isolation of viable CTCs from whole blood without sample pre-treatment.

Biological applications of graphene-nanoparticle hybrids are significantly influencing current biotechnology. The hybrids enable the development of biosensors with enhanced sensitivity, better selectivity, a wide range of detection, and ease of fabrication. Multi-component detection has also been achieved with a low detection limit and a high sensitivity. The biocompatible properties of the hybrids make them applicable for in situ detection of living cells. Rapid, accurate, multi-purpose and low-cost biosensors based on graphene-nanoparticle hybrids are expected to be in mass production in the near future. In future, the as-designed probes can be fine-tuned to find promising use in clinical studies based on their diagnostic and therapeutic performances. The targeted theranostic nanomaterials can serve as prospective candidates for further clinical analysis after comparison with FDA approved therapeutic agents. The centrifugal prototype developed for the detection of CTCs will serve as a useful tool for the rapid, sensitive and selective detection of CTCs which may aid in the early stage screening of cancer. After validating with patients samples, the device can be marketed as a commercial CTC detection platform by collaboration with Biotech companies.

While the future prospects of graphene−nanoparticle hybrids are very bright, our ability to synthesize graphene and its derivatives with controllable sizes, shapes, and defects at a lowcost and high-yield manner as well as our ability to control the size, composition, morphology, and crystallinity of the various incorporated nanoparticles remain critical bottlenecks to the advancement of graphene−nanoparticle hybrids. Moreover, while significant progress has been made to achieve precise control over the density and specific arrangement of nanoparticles that are assembled on graphene and its derivatives, there is still significant room for improvement. As such, there is a need to gain a deeper understanding of the underlying mechanism of graphene−nanoparticle formation to better control their synthesis, assembly, and adhesion. This is especially true for biosensing and imaging applications wherein the nanostructure and charge transfer behavior are particularly important. This will also allow for better control over stem cell differentiation, the distribution and targeting of hybrids in the body, as well as lower the limits of achievable sensitivity and selectivity for biosensing. Finally, significant investigation will be required to assess the toxicity and biodistribution of such hybrid material in vivo as well as the targeting of nanocomposites to improve the efficacy of treatments and reduce off-site toxicity. In addition to biodistribution and long-term safety, understanding the cellular interaction and the precise mechanism of action guiding changes in cellular behavior is equally important for regenerative medicine and tissue engineering.

References

References

Akhavan O, Ghaderi E, Akhavan A (2012) Size-dependent genotoxicity of graphene nanoplatelets in human stem cells. *Biomaterials* 33: 8017-8025.

Al-Ani AL, AlSaadi AM, Kadir FA, Hashim NM, Julkapli NM, Yehye WA (2017) Graphene–gold based nanocomposites applications in cancer diseases; Efficient detection and therapeutic tools. *European Journal of Medicinal Chemistry* 139: 349-366.

Alix-Panabières CKP (2013) Circulating tumor cells: liquid biopsy of cancer. *Clin. Chem.* 59: 110-118.

Aroca R (2006) *Surface-enhanced vibrational spectroscopy*. John Wiley & Sons, Chichester.

Artiles MS, Rout CS, Fisher TS (2011) Graphene-based hybrid materials and devices for biosensing. *Adv. Drug Delivery Rev.* 63: 1352–1360.

Awuah SG, You Y (2012) Boron dipyrromethene (BODIPY)-based photosensitizers for photodynamic therapy. *RSC Adv.* 2: 11169-11183.

Bajpai R, Roy S, Kumar P, Bajpai P, Kulshrestha N, Raee J, Koratkar N, Misra DS (2011) Graphene supported platinum nanoparticle counter-electrode for enhanced performance of dye-sensitized solar cells. *ACS Appl. Mater. Interfaces* 3: 3884–3889.

Balandin AA, Ghosh S, Bao W, Calizo I, Teweldebrhan D, Miao F, Lau CN (2008) Superior thermal conductivity of single-layer graphene. *Nano Lett.* 8: 902-907.

Bian X, Song ZL, Qian Y, Gao W, Cheng ZQ, Chen L, Liang H, Ding D, Nie XK, Chen Z (2014) Fabrication of graphene-isolated-Au-nanocrystal nanostructures for multimodal cell imaging and photothermal-enhanced chemotherapy. *Sci. Rep.* 4: 6093.

Bolotin KI, Sikes KJ, Jiang Z, Klima M, Fudenberg G, Hone J, Kim P, Stormer HL (2008) Ultrahigh electron mobility in suspended graphene. *Solid State Commun.* 146: 351-355.

Bonaccorso F, Sun Z, Hasan T, Ferrari AC (2010) Graphene photonics and optoelectronics. *Nat. Photonics* 4: 611-622.

Burda C, Chen X, Narayanan R, El-Sayed MA (2005) Chemistry and properties of nanocrystals of different shapes. *Chem. Rev.*105: 1025–1102.

Busquets MA, Estelrich J, Sánchez-Martín MJ (2015) Nanoparticles in magnetic resonance imaging: from simple to dual contrast agents. *Int. J. Nanomedicine* 10: 1727-1741.

Cai X, Sushkov AB, Jadidi MM, Nyakiti LO, Myers WRL, Gaskill DK, Murphy TE, Fuhrer MS, Drew HD (2015) Plasmon-enhanced terahertz photodetection in graphene. *Nano Lett.* 15: 4295-4302.

Champion A, Kambhampati P (1998) Surface-enhanced Raman scattering. *Chem. Soc. Rev.* 27: 241–250.

Chen Q, Liang C, Sun X, Chen J, Yang Z, Zhao H, Feng L, Liu Z (2017) H_2O_2-responsive liposomal nanoprobe for photoacoustic inflammation imaging and tumor theranostics via *in vivo* chromogenic assay. *Proc. Natl. Acad. Sci. USA* 114: 5343-5348.

Chen Y, Guo F, Qiu Y, Hu H., Kulaots I, Walsh E, Hurt RH (2013) Encapsulation of particle ensembles in graphene nanosacks as a new route to multifunctional materials. *ACS Nano* 7: 3744–3753.

Chen Y, Li Y, Sun D, Tian D, Zhang J, Zhu JJ (2011) Fabrication of gold nanoparticles on bilayer graphene for glucose electrochemical biosensing. *J. Mater. Chem.* 21: 7604–7611.

Chen Z, Liu L, Liang R, Luo Z, He H, Wu Z, Tian H, Zheng M, Ma Y, Cai L (2018) Nanozyme decorated metal–organic frameworks for enhanced photodynamic therapy. *ACS Nano* 12: 651-661.

Cheng L, Yang K, Chen Q, Liu Z (2012) Organic stealth nanoparticles for highly effective *in vivo* near-infrared photothermal therapy of cancer. *ACS Nano* 6: 5605–5613.

Choi WI, Kim JY, Kang C, Byeon CC, Kim YH, Tae G (2011) Tumor regression *in vivo* by photothermal therapy based on gold nanorod-loaded, functional nanocarriers. *ACS Nano* 5: 1995–2003.

Chopra N, Bachas LG, Knecht MR (2009) Fabrication and biofunctionalization of carbon-encapsulated Au nanoparticles. *Chem. Mater*. 21: 1176–1178.

Chou CH, Chen CD , Wang CR (2005) Highly efficient, wavelength-tunable, gold nanoparticle based optothermal nanoconvertors. *J Phy Chem B.* 109: 11135-11138.

Diaz LA Jr, Bardelli (2014) Liquid biopsies: genotyping circulating tumor DNA. *J. Clin. Oncol.* 32: 579-586.

Ding SY, You EM, Tian ZQ, Moskovits M (2017) Electromagnetic theories of surface-enhanced Raman spectroscopy *Chem. Soc. Rev.* 46: 4042–4076.

Dolmans DE, Fukumura D, Jain RK (2003) Photodynamic therapy for cancer. *Nat. Rev. Cancer* 3: 380-387.

Dreyer DR, Park S, Bielawski CW, Ruoff RS (2010) The chemistry of graphene oxide. *Chem. Soc. Rev.* 39: 228-240.

Echtermeyer TJ, Britnell L, Jasnos PK, Lombardo A, Gorbachev RV, Grigorenko AN, Kim ES, Hirsh V, Mok T, Socinski MA, Gervais R, Wu YL, Li LY, Watkins CL, Sellers MV, Lowe ES, Sun Y, Liao ML, Osterlind K, Reck M, Armour AA, Shepherd FA, Lippman SM, Douillard JY (2008) Gefitinib versus docetaxel in previously treated non-small-cell lung cancer (INTEREST): a randomized phase III trial. *Lancet* 372: 1809-1818.

El-Shall MS, Zedan AF, Moussa S, Terner J, Atkinson G (2013), Ultrasmall gold nanoparticles anchored to graphene and enhanced photothermal effects by laser irradiation of gold nanostructures in graphene oxide solutions *ACS Nano*,7: 627-636.

Fan WP, Shen B, Bu WB, Chen F, Zhao KL, Zhang SJ, Zhou LP, Peng WJ, Xiao QF, Xing HY, Liu JN, Ni DL, He QJ (2013) Rattle-structured multifunctional nanotheranostics for synergetic chemo-/radiotherapy and simultaneous magnetic/luminescent dual-mode imaging. *J. Am. Chem. Soc.* 135: 6494−6503.

Fang Y, Guo S, Zhu C, Zhai Y, Wang E (2010) Self-assembly of cationic polyelectrolyte-functionalized graphene nanosheets and gold nanoparticles: A two-dimensional heterostructure for hydrogen peroxide sensing. *Langmuir 26*: 11277–11282.

Fingar VH, Wieman TJ, Wiehle SA, Cerrito PB (1992) The role of microvascular damage in photodynamic therapy: The effect of treatment on vessel constriction, permeability, and leukocyte adhesion. *Cancer Res.* 52: 4914−4921.

Fu X, Bei F, Wang X, O'Brien S, Lombardi JR (2010) Excitation profile of surface-enhanced Raman scattering in graphene–metal nanoparticle based derivatives. *Nanoscale* 2: 1461–1466.

Geim AK, Ferrari AC, Novoselov KS (2011) Strong plasmonic enhancement of photovoltage in graphene. *Nat. Commun.* 2: 458-464.

Geim AK, Novoselov KS (2007) The rise of graphene. *Nat. Mater*. 6: 183-191.

Gomez-Navarro C, Weitz RT, Bittner AM, Scolari M, Mews A, Burghard M, Kern K (2007) Electronic transport properties of individual chemically reduced graphene oxide sheets *Nano Lett.* 7: 3499-3503.

Goncalves G, Marques PAAP, Granadeiro CM, Nogueira HIS, Singh MK, Gr´acio J (2009) Surface modification of graphene nanosheets with gold nanoparticles: The role of oxygen moieties at graphene surface on gold nucleation and growth. *Chem. Mater.* 21: 4796–4802.

Goodman CM, McCusker CD, Ylmaz T, Rotello VM (2004) Toxicity of gold nanoparticles functionalized with cationic and anionic side chains. *Bioconjugate Chem*. 15: 897–900.

Greco F, Vicent MJ (2009) Combination therapy: opportunities and challenges for polymer-drug conjugates as anticancer nanomedicines. *Adv. Drug Delivery Rev.* 61: 1203-1213.

Guo S, Dong S, Wang E (2009) Three-Dimensional Pt-on-Pd bimetallic nanodendrites supported on graphene nanosheet: Facile synthesis and use as an advanced nanoelectrocatalyst for methanol oxidation. *ACS Nano* 4: 547–555.

Gupta V, Sharma N, Singh U, Arif M (2017) High oxidation levels in graphene oxide, *Optik* 143: 115-124.

Haoran W, Seyyed MHA, Peter JV (2015) Plasmonic colorimetric and SERS sensors for environmental analysis. *Environ. Sci. Nano* 2: 120-135.

Hong B, Jing W, Chunying C (2013) Gold nanorods based platforms for light-mediated theranostics. *Theranostics* 3: 377−394.

Hu C, Rong J, Cui J, Yang Y, Yang L, Wang Y, Liu Y (2013) Fabrication of a graphene oxide–gold nanorod hybrid material by electrostatic self-assembly for surface-enhanced Raman scattering. *Carbon 51*: 255–264.

Ishikawa-Ankerhold HC, Ankerhold R, Drummen GPC (2012) Advanced Fluorescence Microscopy Techniques—FRAP, FLIP, FLAP, FRET and FLIM. *Molecules* 17: 4047–4132.

Jiang J, Fan W, Du X (2014) Nitrite electrochemical biosensing based on coupled graphene and gold nanoparticles. *Biosens. Bioelectron.51*: 343–348.

Kell DB (2010) Towards a unifying, systems biology understanding of large-scale cellular death and destruction caused by poorly liganded iron: Parkinson's, Huntington's, Alzheimer's, prions, bactericides, chemical toxicology and others as examples. *Archives of Toxicology* 84: 825–889.

Kim M, Sohn K, Na HB, Hyeon T (2002) Synthesis of nanorattles composed of gold nanoparticles encapsulated in mesoporous carbon and polymer shells. *Nano Lett.* 2: 1383–1387.

Kim YG, Akbar ZA, Kim DY, Jo SM, Jang SY (2013) Aqueous dispersible graphene/Pt nanohybrids by green chemistry: Application as cathodes for dye-sensitized solar cells. *ACS Appl. Mater. Interfaces* 5: 2053–2061.

Kneipp K, Wang Y, Kneipp H, Perelman LT, Itzkan I, Dasari RR, Feld MS (1997) Single molecule detection using surface-enhanced Raman scattering (SERS). *Phys. Rev. Lett.* 18: 5701–5710.

Laing S, Gracie K, Faulds K (2016) Multiplex *in vitro* detection using SERS. *Chem. Soc. Rev.* 45: 1901–1918.

Lam T, Pouliot P, Avti PK (2013) Superparamagnetic iron oxide based nanoprobes for imaging and theranostics. *Adv Colloid Interface Sci.* 200: 95–113.

Lee C, Wei XD, Kysar JW, Hone J (2008) Measurement of the elastic properties and intrinsic strength of monolayer graphene. *Science* 321: 385-388.

Li C, Winnard PT, Takagi T, Artemov D, Bhujwalla ZM (2006) Multimodal image-guided enzyme/prodrug cancer therapy, *J. Am. Chem. Soc.* 128: 15072-15073.

Li S, Chang K, Sun K, Tang Y, Cui N, Wang Y, Qin W, Xu H, Wu C (2016) Amplified singlet oxygen generation in semiconductor polymer dots for photodynamic cancer therapy. *ACS Appl. Mater. Interfaces* 8: 3624-3634.

Lin Y, Zhang K, Chen W, Liu Y, Geng Z, Zeng J, Pan N, Yan L, Wang X, Hou JG (2010) Dramatically enhanced photoresponse of reduced graphene oxide with linker-free anchored CdSe nanoparticles. *ACS Nano* 4: 3033–3038.

Ling X, Xie L, Fang Y, Xu H, Zhang H, Kong J, Dresselhaus MS, Zhang J, Liu Z (2009) Can graphene be used as a substrate for Raman enhancement? *Nano Lett.* 10: 553–561.

Liu J, Fu S, Yuan B, Li Y, Deng Z (2010) Toward a universal “adhesive nanosheet” for the assembly of multiple nanoparticles based on a protein-induced reduction/decoration of graphene oxide. *J. Am. Chem. Soc.* 132: 7279–7281.

Liu J, Liu Y, Bu W, Bu J, Sun Y, Du J, Shi J (2014) Ultrasensitive nanosensors based on upconversion nanoparticles for selective hypoxia imaging *in vivo* upon near-infrared excitation. *J. Am. Chem. Soc.* 136: 9701-9709.

Liu Q, Wei L, Wang J, Peng F, Luo D, Cui R, Niu Y, Qin X, Liu Y, Sun H, Yang J, Li Y (2012) Cell imaging by graphene oxide based on surface enhanced Raman scattering. *Nanoscale* 4: 7084–7089.

Liu Y, Qin R, Sebastian AJZ, Eefjan B, Michal H (2015) Antibacterial photodynamic therapy: overview of a promising approach to fight antibiotic-resistant bacterial infections, *Journal of Clinical and Translational Research*, 1: 140-167.

Liu Z, Liang XJ (2012) Nano-carbons as theranostics. *Theranostics* 2: 235-237.

Ma X, Qu Q, Zhao Y, Luo Z, Zhao Y, Ng KW, Zhao Y (2013) Graphene oxide wrapped gold nanoparticles for intracellular Raman imaging and drug delivery. *J. Mater. Chem. B* 1: 6495–6500.

Mandler D, Wang Z, Zhang J, Yin Z, Wu S, Zhang H (2012) Fabrication of nanoelectrode ensembles by electrodepositon of Au nanoparticles on single-layer graphene oxide sheets. *Nanoscale* 4: 2728–2733.

Marquardt D, Vollmer C, Thomann R, Steurer P, Mulhaupt R, Redel JEC (2011) The use of microwave irradiation for the easy synthesis of graphene-supported transition metal nanoparticles in ionic liquids. *Carbon* 49: 1326–1332.

Moulder JE, Rockwell S (1987) Tumor hypoxia: its impact on cancer therapy. *Cancer Metastasis Rev.* 5: 313-341.

Murphy S, Huang L, Kamat PV (2013) Reduced graphene oxide–silver nanoparticle composite as an active SERS material. *J. Phys.Chem. C* 117: 4740-4747.

Muszynski R, Seger B, Kamat PV (2008) Decorating graphene sheets with gold nanoparticles. *J. Phys. Chem. C* 112: 5263–5266.

Nair LV, Nazeer SS, Jayasree RS, Ajayaghosh A (2015) Fluorescence imaging assisted photodynamic therapy using photosensitizer-linked gold quantum clusters. *ACS Nano* 9: 5825-5832.

Nguyen KT, Zhao Y (2014) Integrated graphene/nanoparticle hybrids for biological and electronic applications. *Nanoscale* 6: 6245-6266.

Ni DL, Zhang JW, Bu WB, Xing HY, Han F, Xiao QF, Yao ZW, Chen F, He QJ, Liu JN, Zhang SJ, Fan WP, Zhou LP, Peng WJ, Shi JL (2014) Dual-targeting upconversion nanoprobes across the blood−brain barrier for magnetic resonance/ fluorescence imaging of intracranial glioblastoma. *ACS Nano* 8: 1231−1242.

Novoselov KS, Geim AK, Morozov SV, Jiang D, Zhang Y, Dubonos SV, Grigorieva IV, Firsov AA (2004) Electric field effect in atomically thin carbon films. *Science* 306: 666–669.

Pan X, Li H, Nguyen KT, Gruner G, Zhao Y (2012) Integrated graphene/nanoparticle hybrids for biological and electronic applications. *J. Phys.Chem. C* 116: 4175–4181.

Peer D, Karp JM, Hong S, Farokhzad OC, Margalit R., Langer R (2007) Nanocarriers as an emerging platform for cancer therapy. *Nat. Nanotechnol.* 2: 751-760.

Peng HP, Hu Y, Liu P, Deng YN, Wang P, Chen W, Liu AL, Chen YZ, Lin XH (2015) Label-free electrochemical DNA biosensor for rapid detection of multidrug resistance gene based on Au nanoparticles/toluidine blue–graphene oxide nanocomposites. *Sens. Actuators B Chem. 207*: 269–276.

Rissin DM, Kan CW, Campbell TG, Howes SC, Fournier DR, Song L, Piech T, Patel PP, Chang L, Rivnak AJ, Ferrell EP, Randall JD, Provuncher GK, Walt DR, Duffy DC (2010) Single-molecule enzyme-linked immunosorbent assay detects serum proteins at subfemtomolar concentrations. *Nat. Biotechnol.* 28: 595-599.

Rizia B, Surbhi L, Amit J, Naomi JH (2011) Theranostic nanoshells: from probe design to imaging and treatment of cancer. *Acc Chem Res.* 44: 936–946.

Sanchez VC, Jachak A, Hurt RH, Kane AB (2012) Biological interactions of graphene-family nanomaterials: an interdisciplinary review. *Chem.Res.Toxicol.* 25: 15–34.

Schroeder A, Heller DA, Winslow MM, Dahlman JE, Pratt GW, Langer R, Jacks T, Anderson DG (2012) Treating metastatic cancer with nanotechnology. *Nat. Rev. Cancer,* 12: 39−50.

Shan C, Yang H, Han D, Zhang Q, Ivaska A, Niu L (2010) Graphene/AuNPs/chitosan nanocomposites film for glucose biosensing. *Biosens. Bioelectron.* 25: 1070–1074.

Stephen ZR, Kievit FM, Zhang M (2011) Magnetite nanoparticles for medical MR imaging. *Mater. Today* 14: 330–338.

Stiles PL, Dieringer JA, Shah NC, van Duyne RP (2008) Surface-enhanced Raman spectroscopy. *Annu. Rev. Anal. Chem.* 1: 601–626.

Stoller MD, Park SJ, Zhu YW, An JH, Ruoff RS (2008) Graphene-based ultracapacitors. *Nano Lett.* 8: 3498-3502.

Sun X, Jia M, Guan L, Ji J, Zhang Y, Tang L, Li Z (2015) Multilayer graphene–gold nanocomposite modified stem-loop DNA biosensor for peanut allergen-Ara h1 detection. *Food Chem.* 172: 335–342.

Swierczewska M, Liu G, Lee S, Chen X (2012) High-sensitivity nanosensors for biomarker detection. *Chem. Soc. Rev.* 41: 2641-2655.

Szunerits S, Boukherroub R (2014) Electrochemistry of graphene: The current state of the art. 12: 211–242.

Tsien RY (2003) Imagining imaging's future. *Nat. Rev. Mol. Cell Biol.* 9:16–21.

Turcheniuk K, Boukherroub R, Szunerits S (2015) Gold–graphene nanocomposites for sensing and biomedical applications. *J. Mater. Chem. B* 3: 4301–4324.

Ushio-Fukai M, Nakamura Y (2008) Reactive oxygen species and angiogenesis: NADPH oxidase as target for cancer therapy. *Cancer Lett.* 266: 37-52.

Varela-Rizo H, I. Mart´ ın-Gull, Terrones M (2012) Vitamin C is an ideal substitute for hydrazine in the reduction of graphene oxide suspensions. *ACS Nano* 6: 4565–4572.

Wang W, He D, Duan J, Wang S, Peng H, Wu H, Fu M, Wang Y, Zhang X (2013) Simple synthesis method of reduced graphene oxide/gold nanoparticle and its application in surface-enhanced Raman scattering. *Chem. Phys. Lett.* 582: 119–122.

Wang X, Qian X, Beitler JJ, Chen ZG, Khuri FR, Lewis MM, Shin HJ, Nie S, Shin DM (2011) Detection of circulating tumor cells in human peripheral blood using surface-enhanced Raman scattering nanoparticles. *Cancer Res.* 71: 1526–1532.

Wang Y, Polavarapu L, Liz-Marzán LM (2014) Reduced graphene oxide-supported gold nanostars for improved SERS sensing and drug delivery. *ACS Appl. Mater. Interfaces* 6: 21798–21805.

Wilson R (2008) The use of gold nanoparticles in diagnostics and detection. *Chem. Soc. Rev.* 37: 2028–2045.

Xu C, Yang D, Mei L, Li Q, Zhu H, Wang T (2013) Targeting chemophotothermal therapy of hepatoma by gold nanorods/graphene oxide core/shell nanocomposites. *ACS Appl. Mater. Interfaces* 5: 12911–12920.

Yu J, Ju YM, Zhao LY, Chu X, Yang WL, Tian YL, Sheng FG, Lin J, Liu F, Dong YH, Hou YL (2016) Multistimuli regulated photochemothermal cancer therapy remotely controlled via Fe_5C_2 nanoparticles. *ACS Nano* 10: 159−169.

Yuan Y, Zhang Y, Liu B, Wu H, Kang Y, Li M, He N, Zhang J (2015) Optical and electron microscopy study of laser-based intracellular molecule delivery using peptide-conjugated photodispersible gold nanoparticle agglomerates. *Nanobiotechnol.* 13: 1–15.

Zhang C, Bu W, Ni D, Zhang S, Li Q, Yao Z, Zhang J, Yao H, Wang Z, Shi J (2016) Synthesis of iron nanometallic glasses and their application in cancer therapy by a localized Fenton reaction. *Angew. Chem. Int. Ed.* 55: 2101-2106.

Zhang D, Gan L, Cao Y, Wang Q, Qi L, Guo X (2012) Understanding charge transfer at PbS-decorated graphene surfaces toward a tunable photosensor. *Adv. Mater.* 24: 2715–2720.

Zhang J, Jianga C, João PFL, Ricardo BA, Hua Z, Luis AM (2018) An updated overview on the development of new photosensitizers for anticancer photodynamic therapy. *Acta Pharmaceutica Sinica B* 8: 137-146.

Zhang L, Riethdorf S, Wu G, Wang T, Yang K, Peng G, Liu J, Pantel K (2012) Meta-analysis of the prognostic value of circulating tumor cells in breast cancer. *Clin. Cancer Res.*18: 5701–5710.

Zhang L, Xia J, Zhao Q, Liu L, Zhang Z (2010) Functional graphene oxide as a nanocarrier for controlled loading and targeted delivery of mixed anticancer drugs. *Small* 6: 537-544.

Zhao H, Wang Y, Wang Y, Cao T, Zhao G (2012) Electro-Fenton oxidation of pesticides with a novel Fe_3O_4@ Fe_2O_3/ activated carbon aerogel cathode: high activity, wide pH range and catalytic mechanism. *Appl. Catal. B* 125: 120−127.

Zheng Z, Cheng Y, Yan X, Wang R, Zhang P (2014) Enhanced electrochemical properties of graphene-wrapped $ZnMn_2O_4$ nanorods for lithium-ion batteries. *J.Mater.Chem. A* 2: 149–154.

Zhou H, Qiu C, Liu Z, Yang H, Hu L, Liu J, Gu C, Sun L (2010) Thickness-dependent morphologies of gold on *N*-layer graphenes. *J. Am. Chem. Soc*. 132: 944–946.

Annexure

Research publications

1. Victor SP, **Jibin K**, Gayathri devi MG , Remya K,Vijayan VM, Muthu J, Design and characterization of biodegradable macroporous hybrid inorganic-organic polymer for orthopedic applications. *Materials Science and Engineering: C*, 77: 513-520.

2. **Jibin K**, Jayaram SP, Saranya G, Sachin PS, Maiti KK, Jayasree RS Optically controlled hybrid metamaterial of plasmonic spiky gold inbuilt graphene sheets for bimodal imaging guided multimodal therapy (Communicated).

3. **Jibin K**, Jayasree R S *et al.*, Development of tumor microenvironment responsive graphene-gold nanohybrid as a plasmonic magnetic nanoprobe (PMNP) for bimodal imaging guided chemodynamic/photothermal therapy (Communicated).

4. Ariya S, Nazeer SS, Nimi N, Hema S, Parvathy RS, **Jibin K**, Jayasree RS Asialoglycoprotein receptor mediated targeting of a dual function nanoprobe for *in vivo* magnetic resonance imaging and therapy of liver fibrosis (Communicated).

Presentation in conferences

1. **Jibin K** and Jayasree RS "An All-in-One Nanoplatform Built on Gold-Graphene Hybrids for Multifunctional Cancer Theranostics", 6th Asian Biomaterial Congress 2017 (25-27th October) held in Trivandrum.

2. **Jibin K** and Jayasree RS "Graphene-Gold Hybrids for Cancer Theranostics", NANOBIOTEK 2018 (24-27th October) held in Delhi.

3. **Jibin K** and Jayasree RS “A Trio Modal Nanotechnological Approach for Cancer Management: Graphene Based Plasmonic Polymer Assemblies for Multimodal Imaging and Therapy” Kerala Science Congress 2019 (2^{nd}-3^{rd} February) held in Kollam.